



**Damage Identification in FRP-Retrofitted Concrete
Structures Using Linear and Nonlinear Guided Waves**

By

Hasan Mohseni

Thesis submitted in fulfilment of the requirements for the degree of
Doctor of Philosophy

The University of Adelaide
School of Civil, Environmental and Mining Engineering
Faculty of Engineering, Computer and Mathematical Sciences

June 2018

Abstract

Structural health monitoring (SHM) involves the implementation of damage identification methods in engineering structures to ensure structural safety and integrity. The paramount importance of SHM has been recognised in the literature. Among different damage identification methods, guided wave approach has emerged as a revolutionary technique. Guided wave-based damage identification has been the subject of intensive research in the past two decades. Meanwhile, applications of fibre reinforced polymer (FRP) composites for strengthening and retrofitting concrete structures have been growing dramatically. FRP composites offer high specific stiffness and high specific strength, good resistance to corrosion and tailorable mechanical properties. On the other hand, there are grave concerns about long-term performance and durability of FRP applications in concrete structures. Therefore, reliable damage identification techniques need to be implemented to inspect and monitor FRP-retrofitted concrete structures.

This thesis aims to explore applications of Rayleigh wave for SHM in FRP-retrofitted concrete structures. A three-dimensional (3D) finite element (FE) model has been developed to simulate Rayleigh wave propagation and scattering. Numerical simulation results of Rayleigh wave propagation in the intact model (without debonding at FRP/concrete interface) are verified with analytical solutions. Propagation of Rayleigh wave in the FRP-retrofitted concrete structures and scattering of Rayleigh waves at debonding between FRP and concrete are validated with experimental measurements. Very good agreement is observed between the FE results and experimental measurements. The experimentally and analytically validated FE model is then used in numerical case studies to investigate the scattering characteristic. The

scattering directivity pattern (SDP) of Rayleigh wave is studied for different debonding size to wavelength ratios and in both backward and forward scattering directions. The suitability of using bonded mass to simulate debonding in the FRP-retrofitted concrete structures is also investigated. Besides, a damage localisation method is introduced based on the time-of-flight (ToF) of the scattered Rayleigh wave. Numerical case studies, involving different locations and sizes of debonding, are presented to validate the proposed debonding localisation method.

Nonlinear ultrasonics is a novel and attractive concept with the potential of baseline-free damage detection. In this thesis, nonlinear Rayleigh wave induced at debondings in FRP-retrofitted concrete structures, is studied in detail. Numerical results of nonlinear Rayleigh wave are validated with experimental measurements. The study considers both second and third harmonics of Rayleigh wave. A very good agreement is observed between numerical and experimental results of nonlinear Rayleigh wave. Directivity patterns of second and third harmonics for different debonding size to the wavelength ratios, and in both backward and forward scattering directions, are presented. Moreover, a damage image reconstruction algorithm is developed based on the second harmonic of Rayleigh wave. This method provides a graphical representation for debonding detection and localisation in FRP-retrofitted concrete structures. Experimental case studies are used to demonstrate the performance of the proposed technique. It is shown that the proposed imaging method is capable of detecting the debonding in the FRP-retrofitted concrete structures.

Overall, this PhD study proves that Rayleigh wave is a powerful and reliable means of damage detection and localisation in FRP-retrofitted concrete structures.

Acknowledgements

I am deeply honoured and privileged to have been able to undertake this PhD research. I feel the most sincere gratitude towards my main supervisor; **Associate Professor Ching-Tai Ng**; whose tremendous support and invaluable guidance led me throughout this postgraduate journey. His extensive technical expertise along with genuine enthusiasm helped me complete this study.

Besides, I need to extend my heartfelt appreciation to my co-supervisor; **Dr. Togay Ozbakkaloglu**; who provided me with precious advice and technical support.

I would also like to thank gratefully the following people:

My fellow postgraduate students and academics at the school of civil, environmental and mining engineering;

Technical and office staff at the faculty of engineering, computer and mathematical sciences;

And;

My Parents; who offered me enthusiastic and wholehearted support.

Hasan Mohseni

June 2018

Declaration by Author

I, Hasan Mohseni, certify that this work contains no material which has been accepted for the award of any other degree or diploma in my name, in any university or other tertiary institution and, to the best of my knowledge and belief, contains no material previously published or written by another person, except where due reference has been made in the text. In addition, I certify that no part of this work will, in the future, be used in a submission in my name, for any other degree or diploma in any university or other tertiary institution without the prior approval of The University of Adelaide and where applicable, any partner institution responsible for the joint-award of this degree. I give consent to this copy of my thesis, when deposited in the University Library, being made available for loan and photocopying, subject to the provisions of the Copyright Act 1968. I also give permission for the digital version of my thesis to be made available on the web, via the University's digital research repository, the Library Search and also through web search engines, unless permission has been granted by the University to restrict access for a period of time. I acknowledge the support I have received for my research through the provision of an Australian Government Research Training Program Scholarship.

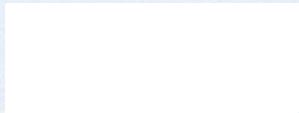
PhD Researcher: Hasan Mohseni**Signature:** 

Table of contents

1	Introduction	1
1.1	Structural Health Monitoring	1
1.2	Guided waves	2
1.3	Fibre reinforced polymer composites	4
1.4	Objective and aims of the research	5
1.5	Thesis outline	5
1.6	List of publications	8
2	Literature review	9
2.1	Damage identification using guided waves	9
2.1.1	Fundamentals of guided waves	9
2.1.2	Generating and sensing of guided waves	12
2.1.3	Digital signal processing	14
2.1.3.1	Hilbert transform	14
2.1.3.2	Fourier transform	15
2.1.3.3	Short-time Fourier transform	15
2.1.3.4	Wavelet transform	16
2.1.4	Guided waves in composites	17
2.1.5	Waves interaction with delamination in composites	21
2.2	Structural health monitoring of FRP-retrofitted concrete structures	24
2.2.1	Applications of FRP in concrete structures	24

2.2.2	Importance of SHM in FRP-retrofitted concrete structures	25
2.2.3	Visual testing	27
2.2.4	Impact testing	28
2.2.5	Microwave method	29
2.2.6	Infrared thermography	30
2.2.7	Acoustic emission	31
2.2.8	Guided waves in FRP-retrofitted concrete structures	32
2.2.9	Rayleigh waves in concrete structures	33
2.2.10	Nonlinear Rayleigh waves	34
2.3	Conclusions and research gaps	35
3	Research Methodology	36
3.1	Explicit numerical simulations	36
3.2	Analytical solution	38
3.3	Preparation of FRP-retrofitted concrete experimental specimens	39
4	Scattering of linear Rayleigh wave	43
4.1	Finite element model description	43
4.2	Absorbing regions to improve the computational efficiency in scattering analysis	46
4.3	Attenuation of Rayleigh wave signals	49
4.4	Analytical validation of numerical model	50
4.5	Experimental validation	52
4.5.1	Equipment setup	52
4.5.2	Validation of Rayleigh wave propagation	53

4.5.3	Rayleigh wave scattering at bonded mass	58
4.6	Scattering of Rayleigh wave at debonding at FRP/concrete interface	60
4.6.1	Effect of rebars	61
4.6.2	Effect of debonding size and shape	62
5	Scattering of nonlinear Rayleigh wave	68
5.1	Numerical model	68
5.2	Validation of numerical model	69
5.2.1	Analytical verification	69
5.2.2	Equipment setup	70
5.2.3	Higher harmonics generation due to contact nonlinearity at debonding	71
5.2.4	Accuracy of the element type in simulating higher harmonics	74
5.3	Directivity patterns of higher harmonics generated at debondings	75
6	Debonding localisation in FRP-retrofitted concrete based on scattering of linear Rayleigh wave	82
6.1	Basics of debonding localisation method	82
6.2	Numerical model description	85
6.3	Numerical case studies	87
7	Locating debonding in FRP-retrofitted concrete using nonlinear Rayleigh wave	95
7.1	Debonding detection method using nonlinear Rayleigh wave	95
7.2	Experimental studies	100
7.2.1	Experiment equipment setup	100
7.2.2	Results and discussion	102
8	Conclusions and suggestions for future research	108

8.1 Conclusions	108
8.2 Suggestions for further research	112
9 References	113

List of figures

Figure 1-1. Examples of damage in composites a. surface cut; b. filament breakage; c. impact dent; d. blister; e. surface swelling-blistering; and f. voids in resin filler [3]	2
Figure 1-2. a. Rayleigh wave; b. Love wave; and c. Lamb wave [6]	3
Figure 1-3. a. Bulk waves; and b. guided waves [13]	4
Figure 2-1. Phase velocity of Lamb wave modes in a steel plate as a function of product of frequency and thickness	11
Figure 2-2. Different sizes of PZT elements [28]	13
Figure 2-3. Typical inspection tools for visual testing and hammer tapping [77]	29
Figure 2-4. Microwave apparatus for inspection of concrete members retrofitted with FRP composites [77].	30
Figure 2-5. a. Heating a concrete column wrapped with FRP composites; and b. IRT image showing areas of debonding [82]	31
Figure 2-6. Schematic diagram of acoustic emission method. Courtesy of www.nde-ed.org .	32
Figure 3-1. a. Schematic of FRP-retrofitted concrete with rebars ; b. formwork preparation; c. concrete pour; d. preparation of carbon fabric and epoxy resin; e. saturating carbon fabric with epoxy resin; and f. applying carbon fibre on concrete specimen	41
Figure 4-1. Schematic diagram of the FRP-retrofitted concrete FE model	45

Figure 4-2. Typical contour snapshots of out-of-plane displacement for numerical FRP-retrofitted concrete model with a circular debonding at FRP/concrete interface a. before Rayleigh wave reach debonding; and b. after interaction of Rayleigh wave with debonding.	46
Figure 4-3. Schematic diagram of absorbing regions for wave scattering studies	48
Figure 4-4. Typical contour snapshots of out-of-plane displacement for Rayleigh wave in FRP-retrofitted concrete model without and with absorbing layers a. when the incident wave interacts with the boundary; b. soon after the wave reflection; c. when the incident wave is being absorbed by the absorbing region; and d. soon after the wave absorption.	49
Figure 4-5. Numerical and analytical values of group and phase velocity	51
Figure 4-6. Analytical and numerical mode shapes for FRP-retrofitted concrete model	52
Figure 4-7. Schematic diagram of the experimental setup using 3D laser	53
Figure 4-8. FE calculated and experimentally measured Rayleigh wave signals for concrete specimen 1 (without rebar)	54
Figure 4-9. FE calculated and experimentally measured Rayleigh wave signals for concrete specimen 2 (with rebar)	55
Figure 4-10. Polar directivity of the normalised amplitude of Rayleigh incident wave measured on a circular path with $r = 50\text{mm}$, $0^\circ \leq \theta \leq 360^\circ$ and the actuator located at the centre.	56
Figure 4-11. Experimental measurements using 3D laser Doppler vibrometer	57
Figure 4-12. Attenuation of Rayleigh waves in FRP-retrofitted concrete.	57

Figure 4-13. Normalised polar directivity pattern for the measured signal, with and without cubic 40mm bonded mass.	59
Figure 4-14. SDP for a cubic 40mm bonded mass.	60
Figure 4-15. Effect of rebars on Rayleigh wave propagation.	61
Figure 4-16. SDP for 40mm×40mm rectangular debonding and 40mm diameter circular debonding.	63
Figure 4-17. Normalised amplitude for the forward scattering of rectangular debonding as a function of debonding size to wavelength ratio.	64
Figure 4-18. Normalised amplitude for the forward scattering of circular debonding as a function of debonding diameter to wavelength ratio.	65
Figure 4-19. Normalised amplitude for the backward scattering of rectangular debonding as a function of debonding size to wavelength ratio.	66
Figure 4-20. Normalised amplitude for the backward scattering of circular debonding as a function of debonding diameter to wavelength ratio.	67
Figure 5-1. Numerical and analytical results of the Rayleigh wave phase velocity	70
Figure 5-2. Schematic diagram of experimental setup	71
Figure 5-3. Experimental validation of FE simulated linear Rayleigh wave results	72
Figure 5-4. Experimental validation of FE simulated higher harmonics	74
Figure 5-5. Comparison between the FE simulations using reduced integration elements and full integration elements	75
Figure 5-6. Energy density spectrum in time-frequency domain for a. debonding size of 38×38 mm and $\theta=30^\circ$; and b. debonding size of 22×22 mm and $\theta=330^\circ$	76

Figure 5-7. Directivity pattern for second harmonic amplitude to fundamental harmonic amplitude ratio (A_2/A_1) in the model with debonding size 38mm × 38mm	77
Figure 5-8. Directivity pattern for third harmonic amplitude to fundamental harmonic amplitude ratio (A_3/A_1) in the model with debonding size 22mm × 22mm	77
Figure 5-9. Second harmonic amplitude to fundamental harmonic amplitude ratio (A_2/A_1) in the forward scattering direction as a function of debonding size to wavelength ratio	78
Figure 5-10. Third harmonic amplitude to fundamental harmonic amplitude ratio (A_3/A_1) in the forward scattering direction as a function of debonding size to wavelength ratio	79
Figure 5-11. Second harmonic amplitude to fundamental harmonic amplitude ratio (A_2/A_1) in the backward scattering direction as a function of debonding size to wavelength ratio	80
Figure 5-12. Third harmonic amplitude to fundamental harmonic amplitude ratio (A_3/A_1) in backward scattering direction as a function of debonding size to wavelength ratio	80
Figure 6-1. Schematic diagram of 1D damage localization in FRP-retrofitted concrete using ToF	83
Figure 6-2. Schematic diagram of damage localization in FRP-retrofitted concrete element using a pair of actuator/sensor	84
Figure 6-3. FE model of FRP-retrofitted concrete	88

Figure 6-4. PZT and debonding locations in Cases 1-3 of the numerical studies	88
Figure 6-5. Wave signals generated by PZT-1 and captured by PZT-3 in the model without rebars a. signal from model without debonding; b. signal from model with debonding; and c. scattered signal obtained from baseline subtraction	89
Figure 6-6. Wave signals generated by PZT-1 and captured by PZT-3 in the model with rebars a. signal from model without debonding; b. signal from model with debonding; and c. scattered signal obtained from baseline subtraction	91
Figure 6-7. Wave signals generated by PZT-4 and captured by PZT-3 for debonding Case 4	92
Figure 6-8. Elliptic solutions for 6mm diameter circular debonding in a. Case 1; b. Case 2; and c. Case 3	93
Figure 6-9. Elliptic solutions for 8mm diameter circular debonding in Case 4	93
Figure 7-1. a. Rayleigh wave propagation and scattering at debonding between CFRP and concrete interface; and b. discretization of inspection area by image pixels	96
Figure 7-2. Schematic diagram of the proposed damage debonding method and signal processing	100
Figure 7-3. Schematic diagram of the CRFP-retrofitted concrete block and the layout of the surface-mounted transducer array (top view) a. concrete specimen 3 with 60mm×60mm debonding; and b. concrete specimen 4 with 40mm×300mm debonding	101
Figure 7-4. Experiment setup for one of the scanning processes in the sequential scan	101

Figure 7-5. Measured data of signal path <i>T1-T4</i> with debonding size 60mm × 60mm	102
Figure 7-6. Energy density spectrum in time-frequency domain for the data of signal path <i>T1-T4</i> with debonding size 60mm × 60mm	103
Figure 7-7. Normalised spectral amplitude of signal path <i>T1-T4</i> at fundamental frequency and second harmonic frequency for debonding size 60mm × 60mm	103
Figure 7-8. Angular dependence of group velocity in m/s for the CFRP-retrofitted concrete	105
Figure 7-9. Typical image of actuator/sensor signal paths <i>T1-T4</i> for debonding size 60mm × 60mm	105
Figure 7-10. a. Debonding location image; and b. corresponding binary image for debonding size 60mm × 60mm (Circles: PZT transducers, dashed line: actual debonding location and size, cross: centroid of the binary image)	106
Figure 7-11. a. Debonding location image; and b. corresponding binary image for debonding size 40mm × 300mm (Circles: PZT transducers, dashed line: actual debonding location and size)	107

List of tables

Table 2-1. Comparison of typical properties of three types of FRP with steel [68]	25
Table 2-2. Stages of application of FRP on concrete structures and different causes of defect [20]	26
Table 4-1. Elastic properties of each FRP lamina	44
Table 6-1. Elastic properties of carbon fibre and epoxy resin	86
Table 6-2. Mechanical properties of each FRP ply	87
Table 6-3. Coordinates of the PZT centres in numerical case studies	90
Table 6-4. Coordinates of the debonding centres and diameters in numerical case studies	90

1 Introduction

1.1 Structural Health Monitoring

Engineering structures are indispensable assets of the society and provide people with crucial services. Therefore, integrity, serviceability and safety of the engineering structures are of paramount importance. The literature on Structural Health Monitoring (SHM) has been developed extensively over the past two decades [1, 2]. SHM is defined as the implementation of an integrated sensing/actuating system in engineering structures in order to monitor structural conditions and identify damage through data acquisition and processing. Damage can be defined as any local variation in the physical state or mechanical properties of a structural component, which can adversely affect the structural behaviour [3]. Depending on the material, fabrication and geometry of the structure, different types of damage can occur; e.g. cracks and fractures, buckling, corrosion, joint loosening, matrix cracking, fibre pull-out or breakage, delamination and debonding [4]. Some common types of damage in composites are shown in Figures 1-1a to 1-1f. The procedure of damage identification can be divided into four levels [5]:

- Detecting the existence of damage
- Determining damage location
- Identifying damage type
- Quantifying extent or severity of the damage

It should be noted that it is more difficult and challenging to achieve higher level of damage identification. The development and use of accurate, reliable and economical damage detection

techniques can enhance structural safety, integrity and serviceability. In this regard, a wide variety of damage identification methods have been developed in the literature.

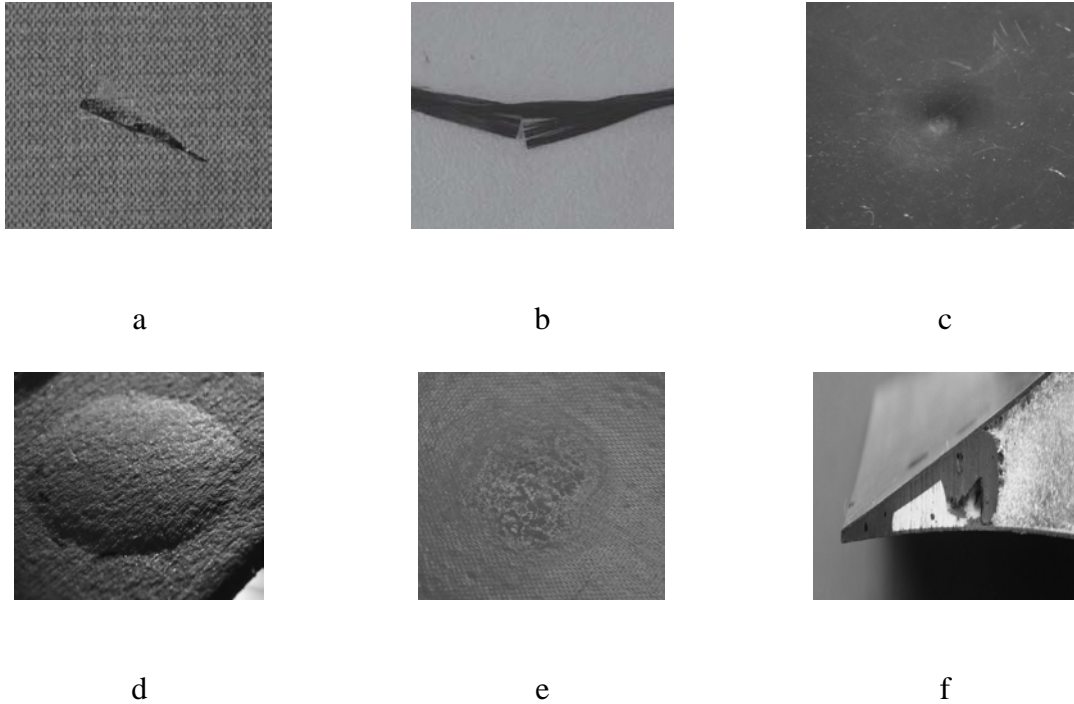


Figure 1-1. Examples of damage in composites a. surface cut; b. filament breakage; c. impact dent; d. blister; e. surface swelling-blistering; and f. voids in resin filler [3]

1.2 Guided waves

Guided waves propagate in solid media and their propagation is characterised by the boundaries of the waveguide. Different types of guided waves can occur in different types of structures, depending on geometry and boundary conditions of structural element(s). Some types of guided waves are shown in Figure 1-2 and they are listed as below.

- Rayleigh waves, also defined as surface waves, propagate along the surface of a semi-infinite solid medium.

- Love waves also propagate in a semi-infinite solid medium in which direction of particle vibration is horizontal and perpendicular to the propagation direction.
- Lamb waves propagate in a plate or plate-like thin medium.

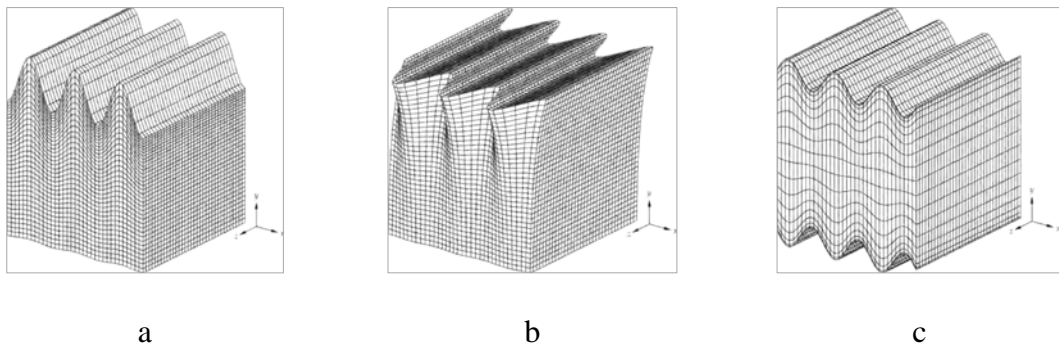


Figure 1-2. a. Rayleigh wave; b. Love wave; and c. Lamb wave [6]

Guided wave damage identification methods have significantly captured interests of researchers in the past two decades [7-9]. The advantages of guided waves over conventional bulk wave inspection methods can be enumerated as follows [10-13]:

- Guided waves can propagate over relatively long distances while conventional bulk waves can inspect only a limited area of structure from a single probe location. This is schematically shown in Figures 1-3a and 1-3b.
- Guided waves are economical because their application is fast, energy-efficient and cost-effective.
- Guided waves have active nature, which enables clients to apply them wherever and whenever necessary.
- Guided waves have ability to inspect inaccessible, encapsulated and embedded structural elements.
- Guided waves have great sensitivity to different types of damage.

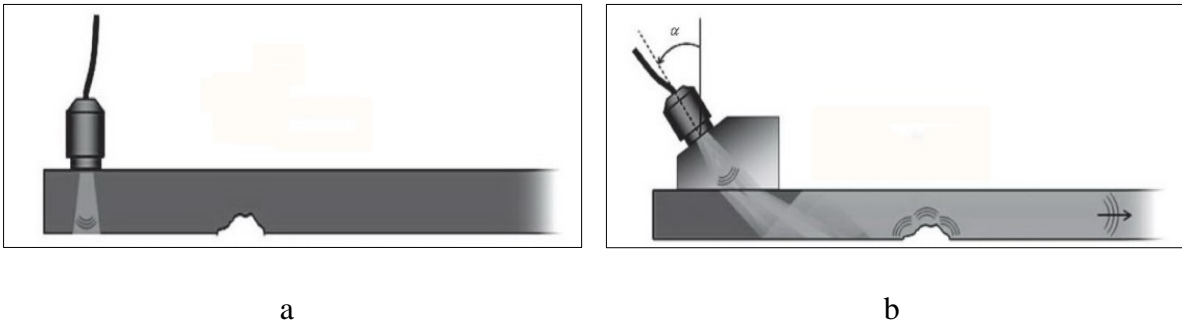


Figure 1-3. a. Bulk waves; and b. guided waves [13]

1.3 Fibre reinforced polymer composites

Fibre reinforced polymer (FRP) composites have been extensively used for retrofitting, strengthening and repairing concrete structures [14]. The use of FRPs is economical and they have high specific strength and high specific stiffness [15]. They, besides, show better resistance to corrosion than other conventional construction materials such as steel. There are, on the other hand, grave concerns about long-term performance of FRPs on concrete structures [16-18]. That is in part because FRP is still a relatively new concept compared to other conventional structural materials, such as steel and concrete. In addition, for FRP bonded to concrete, experimental data on durability is sparse and not well-documented [19].

Different types of defects can occur during preparation, installation and service life of concrete structures retrofitted by FRP composites [20]. Several non-destructive evaluation (NDE) techniques, such as impact testing, infrared thermography and acoustic emission are currently implemented in FRP-retrofitted concrete structures [21]. Due to the active nature of guided waves and their above-mentioned advantages, guided wave-based method seems promising for damage identification in FRP-retrofitted concrete structures; particularly; debonding detection at FRP/concrete interface. To date, different approaches have been

adopted by researchers towards guided wave-based damage detection in homogenous and composite materials, which will be discussed in the literature review.

1.4 Objective and aims of the research

The main objective of this research is to gain physical insights and develop guided wave-based damage identification techniques for FRP-retrofitted concrete structures. Guided waves propagate in FRP-retrofitted concrete structures as Rayleigh wave. Therefore, to achieve the main objective, the following aims have been pursued:

- To gain physical insights into Rayleigh wave propagation in FRP-retrofitted concrete structures and scattering at debonding at FRP/concrete interface.
- To enhance understanding about higher harmonics generation of Rayleigh wave due to interaction with debonding between FRP and concrete.
- To develop a debonding localisation method in FRP-retrofitted concrete structures using linear Rayleigh wave.
- To develop a debonding detection technique in FRP-retrofitted concrete structures using higher harmonics of Rayleigh wave.

1.5 Thesis outline

Chapter 1 (current chapter) provides an introduction, and objective and aims of this research. A general explanation of SHM and the use of guided wave for damage identification is provided. Applications of FRP composites to retrofit concrete structures and defects in FRP-retrofitted concrete structures are then discussed. A list of publications, including journal and conference papers, is also mentioned at the end of this chapter.

Chapter 2 presents a comprehensive literature review in two sections. The first section reviews applications of guided waves for damage identification, particularly in composite structures. Various aspects of guided wave-based damage identification are discussed. The second section reviews applications of FRP composites in concrete structures, defects in FRP-retrofitted concrete structures, and current inspection methods for FRP-retrofitted concrete structures. Based on the literature review, the research gaps are then identified.

Chapter 3 discusses the proposed research methodology and the basics of numerical methods for simulation of Rayleigh wave propagation and scattering. Besides, the analytical solution for verification of Rayleigh wave propagation is described. The preparation steps of FRP-retrofitted concrete specimens are also presented in this chapter.

Chapter 4 presents a study of Rayleigh wave propagation in FRP-retrofitted concrete structures and scattering of linear Rayleigh wave at debonding between FRP and concrete. Numerical simulations of Rayleigh wave propagation and scattering are presented and validated with analytical solutions and experimental measurements. Absorbing layers are developed to enhance computational efficiency of numerical simulations. Furthermore, this chapter discusses the suitability of bonded masses to simulate debonding at FRP/concrete interface. To investigate effects of debonding size and shape on Rayleigh wave scattering, a parametric study is also presented.

Chapter 5 provides insights into generation of higher harmonics of Rayleigh wave due to contact nonlinearity at debondings in FRP-retrofitted concrete structures. Numerical simulations of linear and nonlinear components of Rayleigh waves are validated with experimental measurements. Generation of both second and third harmonics of Rayleigh wave

are investigated and validated with experiments. A parametric study is also carried out to investigate the directivity patterns of second and third harmonics of Rayleigh waves for different sizes of debonding at FRP/concrete interface.

Chapter 6 presents a debonding detection method in FRP-retrofitted concrete structures based on the scattering of linear Rayleigh wave. The proposed method employs time-of-flight of the scattered Rayleigh waves at debonding at FRP/concrete interface. Numerical case studies are presented to validate the proposed debonding detection technique. Different locations and sizes of debonding are considered in numerical investigations.

Chapter 7 introduces a debonding identification technique in FRP-retrofitted concrete structures based on nonlinear Rayleigh wave. An imaging approach is adopted to locate debonding using higher harmonics generation at debonding between FRP and concrete. The imaging method is successfully applied to locate the debonding in experimental case studies. The proposed technique can facilitate a reference-free damage detection in FRP-retrofitted concrete structures.

Chapter 8 presents the conclusions drawn from this PhD study. Potential subjects for further research are also suggested in this chapter.

1.6 List of publications

Journal papers:

- Mohseni H and Ng CT. Rayleigh wave for detecting debonding in FRP-retrofitted concrete structures using piezoelectric transducers. *Computers and Concrete* 2017; 20: 583-593.
- Mohseni H and Ng CT. Rayleigh wave propagation and scattering characteristics at debondings in fibre-reinforced polymer-retrofitted concrete structures. *Structural Health Monitoring* 2018; (10.1177/1475921718754371)
- Mohseni H and Ng CT. Higher harmonic generation of Rayleigh wave at debondings in FRP-retrofitted concrete structures. *Smart Materials and Structures* 2018. (Under review)
- Ng CT, Mohseni H and Lam HF. Debonding detection in CFRP-retrofitted reinforced concrete structures using nonlinear Rayleigh wave. *Mechanical Systems and Signal Processing* 2018. (Under review)

Conference paper:

- Mohseni H and Ng CT. Guided wave for debonding detection in FRP-retrofitted concrete structures. *Second international conference on performance-based and lifecycle structural engineering*. Brisbane, Australia 2015.

2 Literature review

2.1 Damage identification using guided waves

Guided waves have been of great interest among researchers, especially in the past two decades [22, 23]. Different aspects of guided wave damage identification including wave actuation and collection, signal processing and interpretation, have been studied. The literature on guided wave is still being developed rapidly with a focus on damage identification in a wide variety of homogenous and composite materials with different types of damage. However, guided wave-based damage identification in composite structures is very complex because of non-homogeneous and layered architecture of composites, which results in several reflections and refractions of guided wave signals [24, 25].

2.1.1 Fundamentals of guided waves

Horace Lamb [26], was first to explain waves in plates and therefore plate wave has been named after him. Before that, Rayleigh [27] had discovered waves along the surface of a semi-infinite elastic solid. Lamb Waves are guided waves propagating in a plate or thin plate-like medium. There are two fundamental modes of Lamb waves, symmetric (S_0) and asymmetric (A_0) Lamb waves. A_0 waves have smaller wavelength and are therefore more sensitive to damage; however, S_0 waves have smaller magnitude and can travel longer distance over the surface of structure compared to A_0 waves. Based on parameters and conditions of the guided wave problem, the appropriated wave mode should be selected. Propagation of S_0 and A_0 Lamb wave in a plate can be expressed by Equations 1 and 2 respectively [28]:

$$\frac{\tan(qh)}{\tan(ph)} = -\frac{4k^2pq}{(k^2 - q^2)^2} \quad (1)$$

$$\frac{\tan(qh)}{\tan(ph)} = -\frac{(k^2 - q^2)^2}{4k^2pq} \quad (2)$$

The parameters p and q are given by Equations 3 and 4 where C_L and C_T denote longitudinal and transverse velocities respectively. Also, h , ω , k , ν , ρ and E represent half thickness, angular frequency, wavenumber, Poisson's ratio, density and the Young's modulus respectively.

$$p^2 = \left(\frac{\omega}{C_L}\right)^2 - k^2 \quad (3)$$

$$q^2 = \left(\frac{\omega}{C_T}\right)^2 - k^2 \quad (4)$$

$$C_L = \sqrt{\frac{E(1 - \nu)}{\rho(1 + \nu)(1 - 2\nu)}} \quad (5)$$

$$C_T = \sqrt{\frac{E}{2\rho(1 + \nu)}} \quad (6)$$

Group velocity (C_g) and phase velocity (C_p) are two important concepts, by which the propagation of guided waves can be described. Group velocity is the velocity of propagation of a group of waves with similar frequency. Group velocity can be obtained in experiment based on difference of arrival times of signals. Phase velocity is the propagation speed of the wave phase at a specific frequency. The relationship between wavenumber, angular frequency, phase velocity and group velocity can be expressed as follows:

$$C_p = \frac{\omega}{k} \quad (7)$$

$$C_g = \frac{d\omega}{dk} \quad (8)$$

$$C_g = \frac{d(kC_p)}{dk} = C_p + k \frac{dC_p}{dk} \quad (9)$$

$$C_p = C_p(k) \quad (10)$$

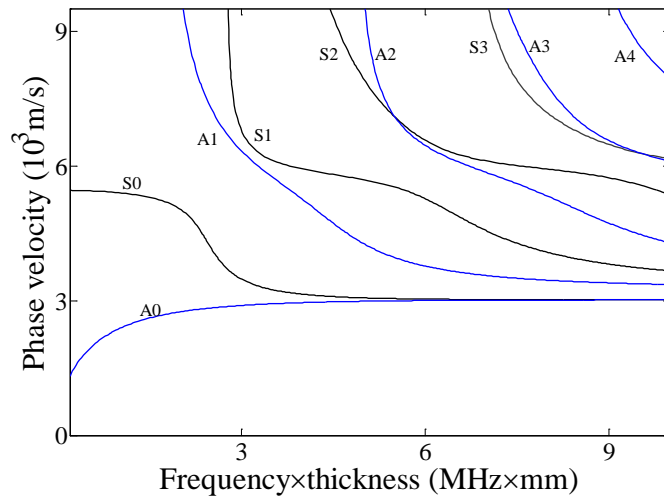


Figure 2-1. Phase velocity of Lamb wave modes in a steel plate as a function of product of frequency and thickness

Dependency of phase velocity on spatial frequency means that a wave is dispersive. If phase velocity is constant, then $C_p=C_g$ and there will be no dispersion. The relationship between group velocity, phase velocity, frequency (f) and plate thickness (d) can be described as below [6]:

$$C_g = \frac{(C_p)^2}{C_p - (fd) \frac{dC_p}{d(fd)}} \quad (11)$$

The graphic display of solutions of the guided wave equations is called “dispersion curve” and is of major importance in guided wave-based damage detection analysis. Figure 2-1 shows a phase velocity dispersion curve of symmetric and asymmetric Lamb waves in a steel plate as a function of product of plate thickness and frequency.

2.1.2 Generating and sensing of guided waves

Guided waves can be generated by the use of an actuator or a number of actuators. An actuator is a device which converts electrical signal into mechanical motion. Thus, actuator is called an active device. Capturing of waves is done by a sensor or a network of sensors. A sensor is an instrument which turns a mechanical motion into electrical signal and therefore is called a passive device. Transducer is a device which function as both actuator and sensor. It can convert electrical signal to mechanical motion and vice versa and therefore excitation and sensing of waves can be done by a transducer.

Piezoelectric ceramic (PZT) elements have been widely used in guided wave-based SHM. The direct piezoelectric effect is defined as the generation of electric signal due to mechanical deformation. The opposite effect, which is also called inverse piezoelectric effect, is the application of an electric charge to induce mechanical strain [29]. PZT transducers are able to both generate and capture waves and can be either surface-mounted or integrated into host structure. Main advantages of PZT transducers are listed as follows [28]:

- With the use of PZT elements, guided waves can be excited with controlled waveform, frequency and amplitude.
- The use of PZT transducers is economical because they are inexpensive. Besides, the number of signal generators/sensors in SHM scheme will be substantially reduced as PZTs can both generate and receive signals.
- PZT transducers are lightweight and can be coupled with host structures with minimum intrusion. Figure 2-2 shows examples of different sizes of PZT elements.
- PZT transducers have good mechanical strength.

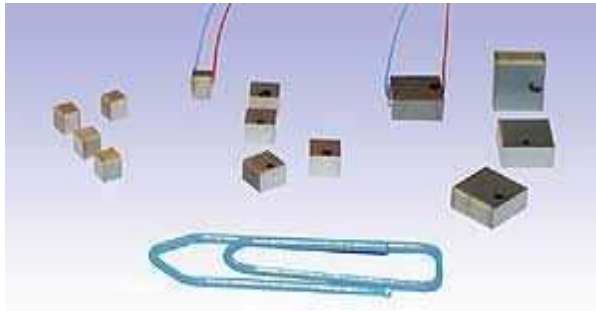


Figure 2-2. Different sizes of PZT elements [28]

Sensors constitute a crucial part of any NDE method and damage identification system. Generally, NDE techniques are based on measuring defect-induced variations in structural properties. Those variations are reflected in the dynamic features such as captured guided wave signals. Therefore, sensor's capability of accurately obtaining and faithfully transmitting all changes in the structure is of paramount importance. In addition, a sensor needs to be flexibly embeddable in or mounted on the host structure with minimum intrusion. Ease of operation is also another necessity for a sensor or a network of sensors [28]. Considering aforementioned advantages of PZT transducers, they are a very good choice for sensing guided wave signals.

2.1.3 Digital signal processing

Signal processing is a very important step in guided wave-base damage detection [30]. The purpose of signal processing is to extract the feature of wave signal, which can help with damage identification. However, the feature extraction is always accompanied by some challenges. For instance, guided wave signals are likely contaminated by a number of factors, such as ambient noise and varying temperature. Moreover, several wave modes can exist in a signal simultaneously. Hence, a proper signal processing scheme should be implemented to accurately extract wave feature containing the damage information.

2.1.3.1 Hilbert transform

Basically, a wave signal is presented as a series of amplitudes in the time domain and therefore time domain methods can be used to extract basic features of the signal. When guided wave signals interact with damage, scattering occurs. Scattering phenomenon can be investigated based on instantaneous wave characteristics. Besides, propagation characteristics of guided waves can be obtained from signals in time domain. The Hilbert transform is an important tool converting a guided wave signal $f(t)$ to an analytical signal $F_A(t)$, where $H(t)$ is the Hilbert transform of $f(t)$:

$$F_A(t) = f(t) + iH(t) = e(t).e^{i\varphi(t)} \quad (15)$$

$$H(t) = \frac{1}{\pi} \int_{-\infty}^{+\infty} \frac{f(t')}{t-t'} dt' \quad (16)$$

$$e(t) = \sqrt{f^2(t) + H^2(t)} \quad (17)$$

$$\varphi(t) = \arctan \frac{H(t)}{f(t)} \quad (18)$$

where $\varphi(t)$ is the instantaneous phase. As seen in the Equation (15), the analytical signal is comprised of a real and an imaginary part. The real part is the original wave signal and the imaginary one is the corresponding Hilbert transform. The energy envelope of guided wave signals in time domain is often obtained by Hilbert transform.

2.1.3.2 Fourier transform

The captured guided wave signals usually contain ambient noise as well as boundary reflections. Therefore, it is difficult to extract the scattered signal from the time domain signals. Fourier series provide a means for representing the periodic signals in frequency domain. By applying Fourier transform on a wave signal, the signal is decomposed into its harmonic components. The basic relationship of Fourier transform can be described as:

$$F(\omega) = \int_{-\infty}^{+\infty} f(t) \cdot e^{-2\pi i \omega t} dt \quad (19)$$

where $f(t)$ is the wave signal in time domain and ω is the angular frequency. Among Fourier methods, fast Fourier transform (FFT) has been widely used in damage detection studies [31, 32].

2.1.3.3 Short-time Fourier transform

Although FFT technique is commonly used for processing the guided wave signals, it only provides frequency domain information without any time information [33]. A joint time-frequency domain method combines the analysis in time and frequency domain in order to

extract as much as information from the wave signal. A very common joint time-frequency method is the short-time Fourier transform (STFT). In this method, a time window function, usually a Hanning or Gaussian window function, is employed. The window function, denoted by W , is applied on the wave signal $f(\tau)$ around the specific time, t , while ignoring the rest of signal. This operation is then repeated for all intervals along the time axis. The energy density spectrum, which is basically the Fourier transform of the windowed signal, can be expressed as [28]:

$$S(t, \omega) = \int_{-\infty}^{+\infty} f(\tau) \cdot W(\tau - t) e^{-2\pi i \omega \tau} d\tau \quad (20)$$

2.1.3.4 Wavelet transform

Wavelet transform (WT) is another joint time-frequency method. When wavelet transform is applied to a signal, the time-amplitude domain $(t, f(t))$ is transferred into a time-scale domain (a, b) . Here, scale denoted by b , is inversely proportional to frequency. There are two types of wavelet transform, continuous wavelet transform and discrete wavelet transform, and they are denoted by CWT and DWT, respectively [28]:

$$CWT(a, b) = \frac{1}{\sqrt{a}} \int_{-\infty}^{+\infty} f(t) \cdot \psi^*\left(\frac{t-b}{a}\right) dt \quad (21)$$

$$DWT(m, n) = a_0^{-\frac{m}{2}} \int f(t) \cdot \psi(a_0^{-m}t - nb_0) dt \quad (22)$$

$$a = a_0^m, b = na_0^m b_0, m, n \in Z \quad (23)$$

where $f(t)$ is the wave signal and $\Psi(t)$ is orthogonal wavelet function. Besides, a_0 and b_0 define the sampling intervals along the time and scale axes, respectively. Using DWT analysis, we

can decompose signals into discrete components while CWT provides energy spectrum of the wave signal in the time-scale domain. Thus, the computational cost of a CWT analysis is far higher than that of a DWT operation.

2.1.4 Guided waves in composites

Rose [34] provided an insight into the potentials of ultrasonic guided waves for NDE and SHM. Advantages of new method of guided wave over the conventional bulk wave method, along with the possible application fields of guided waves have been outlined. Finite element (FE) method is a widely used and recognized method for numerical simulation. A numerical simulation is usually associated with experimental measurements. The reason for performing experiments is to validate FE results; however, some of the studies in the literature were limited to numerical study only.

Diamanti *et al.* [35] presented a study on detection of low-velocity impact damage in composite plates with Lamb waves using FE method and experimental validation. Generation of A_0 Lamb wave with the use of a linear array of small piezoelectric patches was studied. The optimum number and spacing of piezoelectric patches then was determined and impact damage in multidirectional carbon FRP was detected in experiment. This work was followed by Diamanti *et al.* [36] presenting a study on PZT transducer arrangement for inspection of large composite structures again with the use of finite element method and experimental validation. It involved generation of A_0 Lamb wave in carbon FRP quasi-isotropic laminates using a linear array of thin piezoelectric transmitters operating in-phase. The aim was to develop a system of smart devices that would be permanently attached on the surface of the composite structure and monitor the interaction of Lamb waves at defects with a focus of

inspection of large areas with a limited number of sensors. Defects of critical size and also location of damage was determined. Furthermore, the technique was applied to the inspection of stiffened panels.

Despite all advantages of FE method, the high computational cost is a concern especially when the geometric size of model is large; also, in FE simulation, the unwanted reflection from boundaries is an important issue. To overcome this problem, Drozd *et al.* [37] proposed a concept of using absorbing regions. Absorbing regions are finite regions attached at the extremities of the model in order to approximate the case of an unbounded problem by absorbing waves entering them. Two methods of application of absorbing boundary layers for guided waves are “Perfectly matched layer (PML)” and “Absorbing layers by increasing damping (ALID)”. Rajagopal *et al.* [38] presented analytical modelling of PML and ALID for both bulk wave and guided wave problems. A stiffness reduction method for efficient absorption of waves in absorbing layers was studied by Pettit *et al.* [39]. It was aimed at reducing stiffness values inside absorbing layers so that the time increment could remain constant in spite of increasing damping values. Hosseini and Gabbert [40] studied on using dashpot elements as non-reflecting boundary condition for Lamb wave propagation problems in honeycomb and CFRP plates. The work involved FE simulation using ANSYS along with experimental validation. Moreau and Castaings [41] worked towards reducing the size of FE model with the use of an orthogonality relation. It was a technique for post-processing FE output data corresponding to 3D guided waves scattering problems. The method was based on a 3D orthogonality relation used to calculate the amplitudes of individual Lamb or SH-like modes forming a scattered field predicted by the FE model.

One of the complexities in guided wave problem is wave mode conversion due to defects. Cegla *et al.* [42] studied on mode conversion and scattering of plate waves at non-symmetric circular blind holes in isotropic plates using analytical prediction and experimental measurements. The analytical model was based on Poisson and Mindlin plate wave theories for S_0 and A_0 modes, respectively. Wave function expansion technique and coupling conditions at defect boundary were used to evaluate the scattered far fields for the three fundamental guided wave modes. The results were compared to other analytical models and also experimentally validated. Two active pitch-catch sensing methods for detection of debondings and cracks in metallic structures was studied by Ihn and Chang [43], which could be implemented into aircraft frame structures. First, a single actuator-sensor pair (pitch-catch) was used to generate a damage index in order to be used to characterize damage at a known location. Second, a diagnostic imaging method using multiple actuator-sensor paths was introduced to characterize damage size and location without need of a structural or damage model. For validation, this method then was tested on aluminium plates and a stiffened composite panel. Ng *et al.* [44] introduced a two-phased damage imaging methodology for damage characterization in composites. Integrated PZT transducers were used to sequentially scan the structure before and after the presence of damage. In the first phase, the location of damage was determined by a damage localization image and in the second phase, a diffraction tomography technique was used to characterize the size and shape of damage. The methodology was practical because it needs only a small number of transducers compared to other diffraction tomography algorithms. Also, it was proved to be computationally efficient since damage localization image involved only cross-correlation analysis.

Vanli and Jung [45] presented a new statistical model updating method for damage detection in composites utilizing both sensor data and FE analysis model. The purpose was to use the data received from Lamb wave sensors in order to enhance damage prediction ability of FE analysis model by statistically calibrating unknown parameters of FE model and estimating a bias-correcting function to reach a good agreement between FE model predictions and experimental observations. Experiments were done on composite panel with piezoelectric elements to validate the model. Ng [46] introduced a Bayesian model updating approach for quantitatively identifying damage in beam-like structures using guided waves. It utilizes a hybrid particle swarm optimization algorithm to maximize probability density function of a damage scenario conditional on the captured waves. Not only is this model able to identify damage location, length and depth, but also it can help determine the uncertainty associated with damage identification. A number of experiments were carried out on Aluminium beams with various damage scenarios. Experiments results proved accuracy of damage identification using this model, even when the damage depth was small. A new third-order plate theories in modelling of guided Lamb waves in composites was introduced by Zhao *et al.* [47]. It presented a new HSDT of five degrees of freedom considering the stress free boundary condition in order to shorten calculations. Analytical derivation of guided Lamb wave equation for an n-layered anisotropic composite laminate was the subject of a research presented by Pant *et al.* [48]. Experiments were performed with both S_0 and A_0 Lamb wave modes on an 8-layered carbon fibre epoxy composite panel and also on a 7-layered fibre-metal laminate GLARE in order to validate analytical results.

2.1.5 Waves interaction with delamination in composites

The interaction of guided waves with delamination in composites has been studied extensively. Hayashi and Kawashima [49] carried out a brief study on multiple reflections of Lamb waves at a delamination in an eight-layered plate model using FE method. The study revealed that when Lamb wave propagates toward the delamination, it splits into two independent waves at the entrance of the delamination without any significant reflection. Rather, Lamb wave reflection occurs at the exit of delamination and large reflections happen only if there are phase differences between the divided two regions. Ramadas *et al.* [50] performed a numerical and experimental research of the primary A_0 Lamb wave mode with symmetric delaminations in a quasi-isotropic laminated composite plate. It was concluded that if A_0 is the incident wave at the entrance of delamination, a new S_0 mode wave is created which is confined in sub-laminates. It was observed that only the A_0 incident wave and A_0 mode-converted waves propagate in the main laminate. Ramadas *et al.* [51], then, presented a study on interaction of guided Lamb waves with an asymmetrically located delamination in a laminated composite plate. It was concluded from numerical analysis and also experimental works that when the A_0 mode interacts with end points of an asymmetrically located delamination, it generates a new S_0 mode which propagates in each of two sub-laminates as well as main laminate. Turning mode and a mode converted turning mode were also detected.

Ng and Veidt [52] studied on scattering of fundamental A_0 Lamb waves at delamination in a quasi-isotropic laminate using a three-dimensional explicit FE method and experimental measurements. The study suggested that scattering of A_0 Lamb wave at delamination in composite laminates has far more complexity than the scattering of wave when interacting with damage in isotropic plate. The results showed that scatter amplitude directivity depend

on the delamination size to wavelength ratio and the through thickness of delamination. Ng and Veidt [53], also, performed a study on the interaction of low frequency A_0 Lamb wave - as incident wave- with debondings at structural features in composite laminates. FE simulation of A_0 Lamb wave scattering at a debonding between an 8-ply quasi-isotropic composite laminate and a structural feature was done with software ANSYS and LS-DYNA. Results of FE analysis then were verified by experimental investigations. The study suggested that the amplitude of the A_0 Lamb wave scattered at the debonding, is sensitive to debonding size indicating the potential of low frequency Lamb waves for debonding detection. Furthermore, Ng *et al.* [54] studied on the scattering of the fundamental A_0 Lamb wave at delaminations in quasi-isotropic composite laminates using both analytical and FE investigations. Analytical study was based on the Mindlin plate theory and Born approximation and analytical results were on good agreement with those of FE simulation. Peng *et al.* [55] presented a study on Lamb wave propagation in damaged composite laminates using FE method and experimental investigations. Waves were generated by PZT elements and damage was in form of matrix cracking and delamination in a composite coupon. The study suggested that the effect of delamination highly depends on the material and the frequency of actuation. Also, matrix cracking and delamination should be incorporated in simulation as experiment showed that matrix cracking occurred along with the delamination.

It is well-known that because of multi-layered and non-isotropic architecture of composites, scattered Lamb wave signals are very complex to interpret. What adds to complexity is the presence of some environmental and operational factors which exert influence on captured signals. Schubert *et al.* [56] worked on changes in guided Lamb wave propagation which are not induced by damage. Based on that research, temperature variation, fluid loading,

mechanical loads, absorption of water or chemical into composite matrix can affect Lamb wave propagation properties. Experimental investigations were carried out on anisotropic fibre-reinforced materials to understand the influence of temperature, humidity absorption, structural features, load, fatigue, and local damage using surface-mounted PZT transducers. The study underlined the complexity of distinguishing between damage-related and non-damage-related changes in Lamb wave signals properties, posing a challenge to Lamb wave-based structural health monitoring for real carbon fibre reinforced structures.

2.2 Structural health monitoring of FRP-retrofitted concrete structures

2.2.1 Applications of FRP in concrete structures

FRP composites have been widely used for retrofitting and strengthening existing concrete structures. Applications of FRPs in civil infrastructure are exponentially growing [57-60]. FRP composites are used on concrete structures for different purposes including [61-63]:

- Flexural or shear strengthening of concrete members
- Ductility enhancement of concrete columns
- Repair of damaged or deteriorated concrete components

The need for strengthening can arise from errors in design and/or construction stage, higher loading conditions required by changes in codes and standards or new client's requirements [64]. The main advantages of FRPs over conventional retrofitting materials are [65-67]:

- The use of FRP is fast and economical.
- FRPs are lightweight; therefore; they add very little to the total dead load of the structure. Besides, they do not need temporary support after installation.
- FRPs have high specific strength and high specific stiffness.
- FRPs usually show good fatigue and creep performance.
- FRPs are more resistant to corrosion than conventional construction materials
- FRPs can have versatile fabrication and adjustable mechanical properties.

Table 2-1 compares density, modulus of elasticity, tensile strength, fatigue and sustained loading and durability in alkaline/acid environment of carbon FRP (CFRP), aramid FRP (AFRP), and glass FRP (GFRP) with steel:

Table 2-1. Comparison of typical properties of three types of FRP with steel [68]

	CFRP	AFRP	GFRP	Steel
Density (kg/m ³)	1600–900	1050–1250	1600–2000	7800
Elastic modulus (GPa)	56-300	11-125	15-70	190-210
Tensile strength (MPa)	630-4200	230-2700	500-3000	250-500
Fatigue	Excellent	Good	Adequate	Good
Sustained loading	Very good	Adequate	Adequate	Very good
Alkaline environment	Excellent	Good	A concern	Excellent
Acid/chloride exposure	Excellent	Very good	Very good	Poor

2.2.2 Importance of SHM in FRP-retrofitted concrete structures

While the use of FRPs in civil construction is extensively expanding, “SHM” and “damage detection” in FRP-retrofitted concrete structures must be given a great deal of attention. Unlike conventional construction materials such as steel, application of FRP composite for civil structures is still in early stage and very few data is available for their service life, maintainability and reparability [69]. Durability of FRP bonded to concrete has always been a concern, because many applications are outdoors and subjected to environmental factors, such as moisture and high temperature [70-72]. A number of studies have been concluded that mechanical properties of FRP composites bonded to concrete, degrade with the passage of time [73]. The “American Concrete Institute” committee 440 notifies that experimental data on durability of hybrid FRP-retrofitted concrete structures is rare, disorganized, badly-documented and not readily available [19].

Table 2-2. Stages of application of FRP on concrete structures and different causes of defect [20]

Rehabilitation process stages	Examples of defect cause
Composite constituent materials	<ul style="list-style-type: none"> • overaged, contaminated or moisture-contained resins • incorrect fibre type • loose, twisted or broken fibres • fibre gaps • wrinkled or sheared fabrics • fabric moisture • voids, process-induced or handling damage in pre-fabricated materials
Preparation of FRPs and concrete substrate on the site	<ul style="list-style-type: none"> • inappropriate storage, stoichiometry or mixing of resin • moisture absorption by fibrous materials • inadequate preparation and grinding of concrete substrate • galvanic corrosion of carbon fibres
Installation of composites on concrete substrate	<ul style="list-style-type: none"> • sagging of infiltrated composite material • non-uniform interface (resin-rich & resin-starved) • voids, air-entrancements and porosity at the FRP/concrete interface
FRP-retrofitted concrete in service	<ul style="list-style-type: none"> • penetration of moisture or chemicals at the FRP/concrete interface

In FRP-retrofitted concrete structures, defects can be initiated at any stage of rehabilitation process, including raw constituent material level, on-site preparation of FRP composites and

concrete substrate, installation of FRP composite overlays on reinforced concrete elements and finally during the service life of FRP-retrofitted concrete structure [74]. Defects in materials, preparation and installation are usually caused by human error, while in-service defects are mostly induced by environmental factors [17]. Table 2-2 demonstrates some general causes of defects during different stages of application of FRP on concrete substrate.

In general, the occurrence of defects in material, preparation, installation and in service cannot be completely avoided. If defects are not detected and remedial work is not done appropriately and in time, the defects will propagate and lead to ineffectiveness of retrofitting scheme [75]. This, in fact, underlines the necessity of precise and reliable non-destructive evaluation in FRP-retrofitted concrete structures. Sections 2.2.3 to 2.2.7 will explain the conventional NDE techniques, which are currently implemented for defect detection in FRP-retrofitted concrete structures. Also, applications of linear and nonlinear Rayleigh waves for damage detection will be discussed in Sections 2.2.9 and 2.2.10, respectively.

2.2.3 Visual testing

Visual inspection or visual testing (VT) is the most frequently used NDE method; in fact, visual inspection is the first and fundamental step in any structural inspection or defect detection process. Some types of damage in FRP-retrofitted concrete elements can be detected by VT including [76]:

- Discoloration of materials induced by UV deterioration
- Surface moisture absorption
- Fabric unravelling

However, there are several disadvantages of visual testing method [77]:

- VT is highly susceptible to misunderstanding or misconception of the inspector specially in varying inspection conditions.
- If done properly, VT is only a qualitative method and does not usually demonstrate a high level of consistency.
- Visual inspection is not capable of finding under-surface defects such as debonding between FRP composite and concrete substrate.

The above-mentioned disadvantages of VT should not make it to be put aside. Instead, visual testing is a basic method and needs to be supplemented by more sophisticated NDE techniques [78].

2.2.4 Impact testing

Impact testing, also referred to as hammer tapping, is a very simple method for finding debonding in FRP-retrofitted concrete structures. The impact testing method involves the use of a hard object such as hammer to strike the surface of the composite material which is bonded to a concrete substrate. Debonding between FRP and concrete can result in a hollow tone, which is listened to by an operator. To avoid inflicting damage on the composite, suitable impact devices with proper tapping force and angle need to be applied [79]. Impact testing is very simple and readily-available; however, the biggest drawback of this technique is that it is heavily subjective and dependent on the inspector [80]. Figure 2-3 shows typical tools that are usually used by an inspector for visual testing and hammer tapping.



Figure 2-3. Typical inspection tools for visual testing and hammer tapping [77]

2.2.5 Microwave method

Microwave methods have been implemented to find subsurface defects in FRP-retrofitted concrete structures [81]. In this method, a waveguide transmits electromagnetic wave through FRP-retrofitted concrete element, which is then captured by a probe. Changes in electronic properties of material can be a sign of subsurface damage such as debonding between FRP and concrete. Figure 2-4 displays microwave equipment for inspection of a concrete bridge to find debonding between FRP and concrete. One of the major drawbacks of microwave method is that microwaves cannot fully penetrate into conductive materials; hence, the application of this method for carbon FRP composites is limited [20].



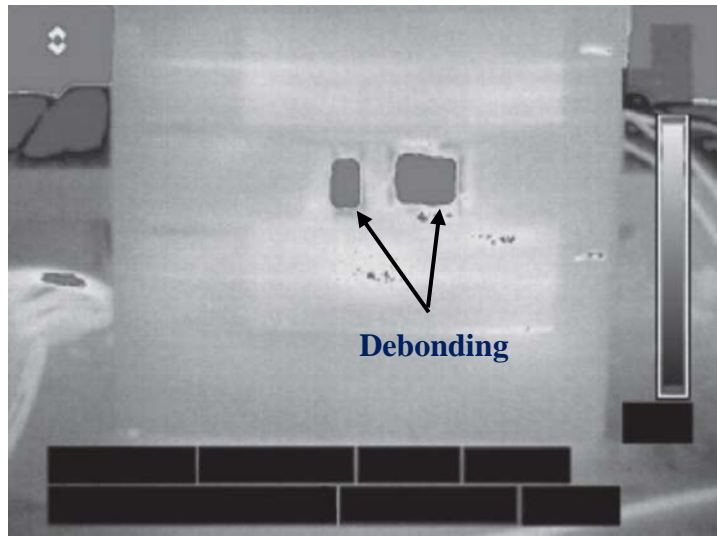
Figure 2-4. Microwave apparatus for inspection of concrete members retrofitted with FRP composites [77].

2.2.6 Infrared thermography

Infrared thermography (IRT) is another NDE technique for defect detection in FRP-retrofitted concrete structures. In this method, heat flows through FRP-retrofitted concrete element as shown in Figure 2-5a. Existence of a defect can disrupt the heat flow, which results in surface temperature change. This change can be captured by an infrared camera. Figure 2-5b shows infrared image of a FRP-retrofitted concrete column, with debonding areas obvious in the image. Despite simplicity of IRT method, some complexities can affect the accuracy of the results. The presence of coating, stain, dust or moisture can make the thermal image very obscure and therefore hide subsurface defects. Environmental conditions such as ambient temperature and wind can also have an adverse effect on the test accuracy. In addition, the initial cost of IRT method is very high and highly-skilled operators is a real necessity. Moreover, the temperature change from subsurface defects such as debonding can be very small and hard to detect [82].



(a)



(b)

Figure 2-5. a. Heating a concrete column wrapped with FRP composites; and b. IRT image showing areas of debonding [82]

2.2.7 Acoustic emission

Acoustic emission (AE) method is based on the fact that when structural elements undergo certain levels of stress, elastic waves are released provided that specific types of defect exist in the structure. Acoustic emission in FRP composites can be induced by matrix cracking, fibre breakage, and delamination. In concrete structures, cracking and debonding between aggregates and mortar can be responsible for acoustic emissions. Also, AE may occur in FRP-retrofitted concrete structures as a result of debonding between FRP composite and concrete substrate [83]. Figure 2-6 shows schematic diagram of acoustic emission technique.

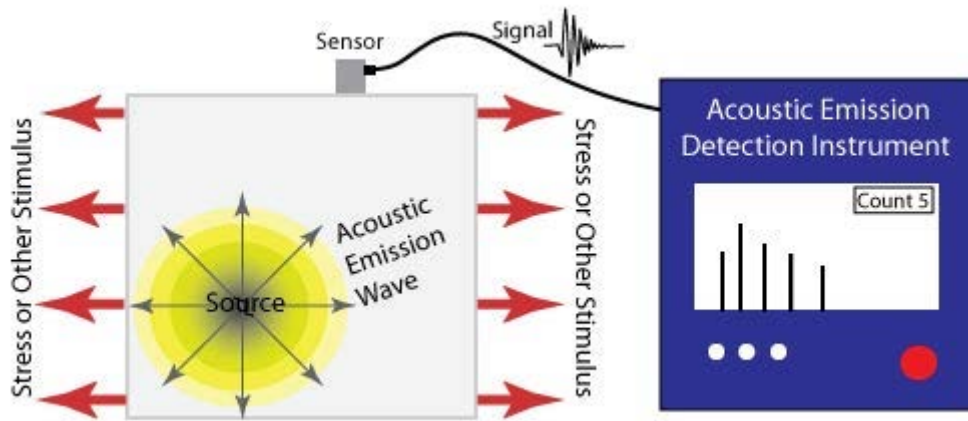


Figure 2-6. Schematic diagram of acoustic emission method. Courtesy of www.nde-ed.org.

Inspection of FRP-retrofitted concrete structures using AE method has some disadvantages. Firstly, acoustic emission is a passive method, i.e. the structure needs to be loaded to a certain level and defect must exist so that acoustic emissions are released. Secondly, AE is not capable of defining the exact location and also the size of damage. Thirdly, highly-skilled operator and very advanced equipment is needed to perform AE procedure [84].

2.2.8 Guided waves in FRP-retrofitted concrete structures

There is very limited literature on guided wave-based damage identification in FRP-retrofitted concrete structures. Kim *et al.* [21] presented a damage detection study in FRP-strengthened concrete elements based on time reversal method. Sharma *et al.* [85] studied on monitoring corrosion of FRP wrapped concrete structures using guided waves. Li *et al.* [86] studied on guided wave-based debonding detection in FRP-reinforced concrete elements using time reversal method and wavelet transform. Based on the literature, it can be found out that although few studies exist on guided waves for FRP-retrofitted concrete, guided wave-based approach is a promising method for SHM in FRP-retrofitted concrete structures [87].

2.2.9 Rayleigh waves in concrete structures

Rayleigh wave is a type of guided wave that propagates along the surface of a semi-infinite solid medium. When a harmonic load is applied on a half-space, Rayleigh wave will contain the biggest portion of energy compared to other types of body waves (S-waves and P-waves), while decaying at a much lower rate along the surface [88]. Rayleigh wave propagation characteristics depend on the geometry and mechanical properties of the medium. The wave characteristics change in the presence of defects or non-conformities. Therefore, applications of Rayleigh wave to detect surface and near-surface damage in concrete have been considered [89]. A numerical model was developed by Hevin *et al.* [90] to characterise concrete surface crack using Rayleigh wave. Edwards *et al.* [91] used low-frequency, wideband Rayleigh wave for gauging the depth of damage in concrete. Sun *et al.* [92] studied on health monitoring and damage detection in concrete structures using Rayleigh wave generated and received by PZT transducers. A study on the repair evaluation of concrete surface cracks was presented by Aggelis and Shiotani [93] using surface and through-transmission waves. Aggelis *et al.* [94] also deployed surface Rayleigh wave to characterise the depth of concrete surface cracks, which helped evaluate effectiveness of the repair. Metais *et al.* [95] studied on Rayleigh wave scattering in concrete using a global neighbourhood algorithm. Lee *et al.* [96] presented a method for estimation of concrete crack depth based on Rayleigh wave. Beside Rayleigh waves, some other types of guided waves have been studied in concrete structures. A numerical model was introduced by Godinho *et al.* [97] for a Shear horizontal (SH) wave-based crack detection in concrete structures. The authors applied two advanced numerical models to simulate, first, the progress of crack propagation and then, the propagation of waves in a

progressively damaged structure. It needs to be mentioned that the aforementioned studies focused on concrete structures only.

2.2.10 Nonlinear Rayleigh waves

Recently, the concept of ultrasonic nonlinearity has attracted growing attention from researchers because of its potentials of baseline-free damage identification and high sensitivity to early stage of defects [98, 99]. Upon interaction of guided waves with a contact-type defect, such as crack [100, 101] and delamination [102, 103], the compressive and tensile components of the signal close and open the contact-type defect, respectively. Therefore, the compressive component passes through the defect while the tensile component is reflected. This phenomenon is referred to as contact nonlinearity, which contributes to generation of higher harmonics with frequency at twice, three times or more of the excitation frequency.

A number of studies have been carried out on nonlinear Rayleigh wave and generation of higher harmonics due to surface defects. Zhang *et al.* [104] studied the higher harmonic generation of Rayleigh waves due to surface scratches in glass. Kawashima *et al.* [105] investigated nonlinear Rayleigh waves due to surface cracks in aluminium using a numerical model and experimental measurements. Yuan *et al.* [106] presented a numerical model of simulating higher harmonics of Rayleigh waves generated by closed cracks. Besides, a number of studies have been performed on material nonlinearity in aluminium [107], titanium [108] and steel [109] using Rayleigh wave.

2.3 Conclusions and research gaps

Having done a very thorough literature review, it is concluded that damage detection in FRP composites with the use of guided waves has been a frequent subject of research. Because of different combinations of wave modes, actuators and sensors, numerous approaches towards guided wave problem can be adopted. Meanwhile, the growing use of FRPs for repairing and strengthening concrete structures and susceptibility of FRP-retrofitted concrete structures to defects, all underscore the strong need for a reliable and precise SHM scheme in those structures. Considering the limitations of current NDE methods in FRP-retrofitted concrete structures, applications of Rayleigh wave have the potential for active and real-time monitoring of the FRP-retrofitted concrete structures using embedded actuating/sensing system.

This research explores the applications of Rayleigh waves for damage identification in FRP-retrofitted concrete structures. Numerical models have been developed to simulate Rayleigh wave propagation. Scattering of Rayleigh wave at debonding at FRP/concrete interface has been characterised. A debonding localisation method has been developed using scattering of linear Rayleigh wave. Furthermore, higher harmonics generation of Rayleigh waves at debonding has been studied. Scattering characteristic of nonlinear Rayleigh waves have also been defined. Nonlinear Rayleigh waves have been used to identify debonding in FRP-retrofitted concrete structures.

3 Research Methodology

3.1 Explicit numerical simulations

In this research, numerical simulations were performed using dynamic/explicit module of ABAQUS version 6.14. In the context of structural dynamics, when the excitation source changes arbitrarily with time or when the system is nonlinear, the dynamic response can be obtained with numerical time-stepping methods. An appropriate numerical procedure needs to fulfil these requirements [110, 111]:

- **Convergence:** the smaller the time step is, the closer the numerical results to the exact solution will be.
- **Stability:** when numerical round-off errors occur, the numerical solution needs to remain stable.
- **Accuracy:** numerical time-stepping methods should yield results that are close enough to the exact solution.

Generally, when response at time $i+1$ is obtained from solving equilibrium equation only at time i without considering equilibrium condition at time $i+1$, the method is called explicit method. On the other hand, if response at time $i+1$ is obtained from solving equilibrium condition only at time $i+1$, the method is called implicit method [110].

For the numerical method, ABAQUS/explicit was used in this research to solve the wave propagation and scattering problem. The explicit solution is well-suited for high speed, short duration dynamic problems including wave propagation. For these types of problems, the explicit procedure offers higher accuracy as well as lower computational cost compared to

implicit solution. The explicit dynamics procedure in ABAQUS is based on an explicit dynamic integration method along with the use of a lumped mass matrix as:

$$\ddot{u}_i = M^{-1} \cdot (P_i - I_i) \quad (24)$$

where M is the lumped mass matrix, P is the external load vector and I is the internal load vector. It should be noted that explicit procedure does not require any iterations and tangent stiffness matrix. The explicit solution in ABAQUS is based on central difference method. For the central different method to be stable, the time increment needs to fulfil the following criterion:

$$\Delta t < \frac{T_n}{\pi} \quad (25)$$

where T_n is the natural period. The time increment in numerical calculations is usually much smaller than this value. For guided wave propagation, the stability limit is often approximated by the smallest transit time of a wave component across any elements in the meshed model:

$$\Delta t_{stable} \approx \frac{L_{min}}{c_L} \quad (26)$$

where L_{min} is the smallest mesh dimension and c_L is the dilatational wave speed. In numerical simulations, the stable time increment is automatically chosen by ABAQUS, which is between 1 to $\frac{1}{\sqrt{3}}$ of the time increment in Equation 26.

3.2 Analytical solution

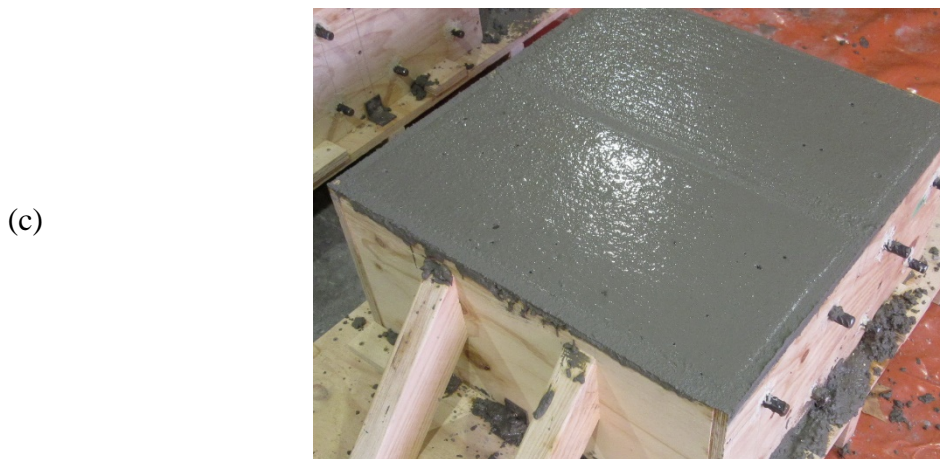
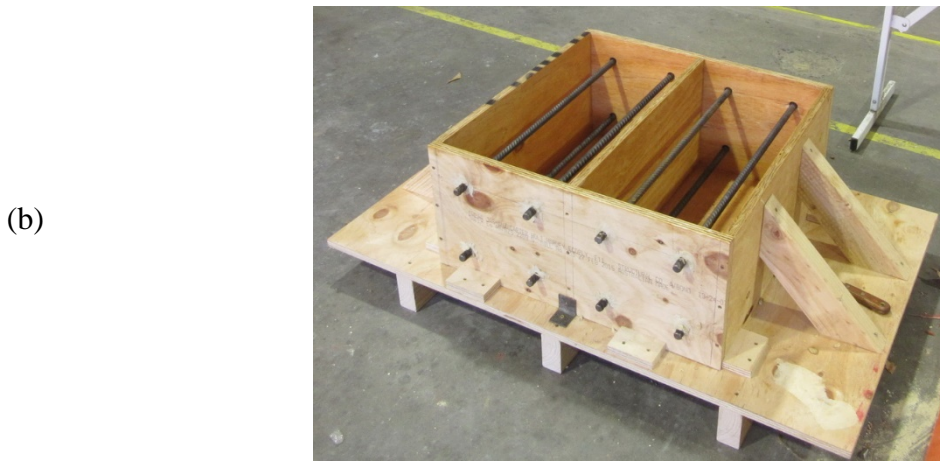
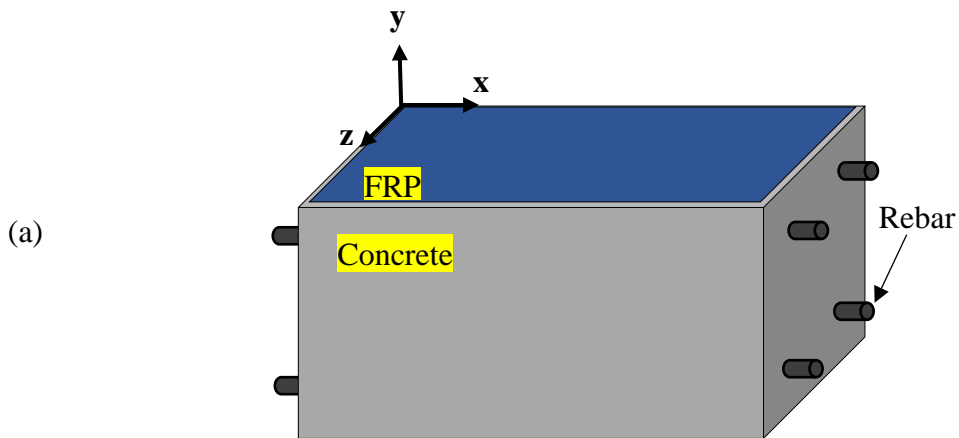
Results of numerical simulations have been analytically verified using DISPERSE. It is a computer program developed by non-destructive testing laboratory of Imperial College London. DISPERSE is aimed at obtaining dispersion curves and helping users get a better understanding of guided wave propagation and develop more efficient non-destructive evaluation methods [112]. DISPERSE version 2.0.16d is able to model and acquire dispersion curves of different geometrical and material properties including Cartesian or cylindrical geometries, single or multiple layers, free or leaky systems, elastic or viscoelastic isotropic materials and anisotropic materials in non-leaky Cartesian geometries.

The global matrix method is employed in DISPERSE. In this method, the propagation of waves in each layer can be described and related to displacements and stresses at any location in the layer through a field matrix. The field matrix coefficients depend on through-thickness position in the layer and mechanical properties of the layer material. The assembly of field matrices forms the global matrix. The whole system is modelled by superposition of wave components and the imposition of boundary conditions at the interface of each two adjacent layers [113]. It should be noted that the global matrix method is based on continuity of stresses and displacements at interfaces of layers. Therefore, numerical results of a damage-free model (without debonding at FRP/concrete interface) can be verified by DISPERSE. For the models with debonding, the numerical simulations were validated with experimental measurements.

3.3 Preparation of FRP-retrofitted concrete experimental specimens

In this research, Rayleigh wave propagation in FRP-retrofitted concrete structures and wave scattering at debonding are simulated by FE method. To validate FE simulation results, experimental measurements have been carried out. For this purpose, four concrete blocks with the Young's modulus of 26.8GPa, density of 2350kg/m³ and a maximum aggregate size of 10mm were cast as shown in Figures 3-1b and 3-1c. The dimensions of the concrete blocks were 300mm×600mm×300mm (W×L×H). Concrete specimen 1 had no steel bars. Concrete specimens 2, 3 and 4 had four 16mm diameter rebars at four corners of the cross section, with 6cm of concrete cover as schematically shown in Figure 3-1a.

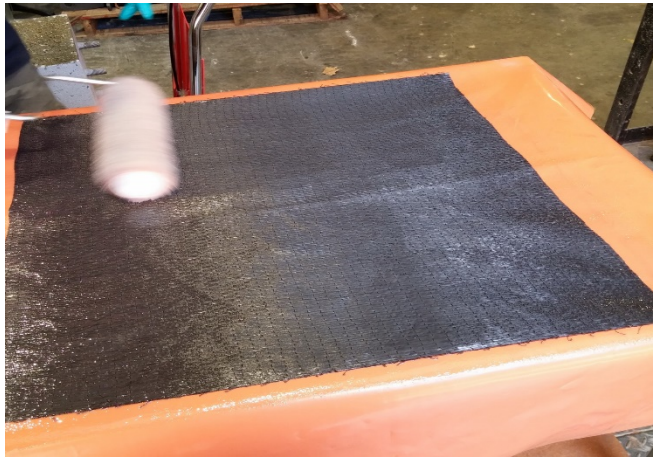
In each specimen, the FRP composite consisted of four unidirectional carbon fibre layers with dimensions of 300mm×600mm and the stacking sequence is [0]₄. The BASF MasterBrace 4500 epoxy resin was applied to saturate each carbon fabric layer. The hand lay-up method was used to sequentially bond saturated fibre layers on the concrete blocks as shown in Figures 3-1d to 3-1f. The constructed 4-ply FRP-bonded concrete was then left at room temperature to cure and harden. Concrete specimens 1 and 2 had no debonding at FRP/concrete interface. The debonding in concrete specimens 3 and 4 was created by inserting Mylar sheet on the surface of concrete before bonding the first layer of fabric. Considering Cartesian coordinates shown in Figure 3-1a, the debonding in concrete specimen 3 was 60mm×60mm with the debonding centre located at $x = 300\text{mm}$ and $z = 150\text{mm}$ and debonding edges parallel to x and y axis. In concrete specimen 4, the debonding was located between $x = 280\text{mm}$ and $x = 320\text{mm}$, and was across whole width of the concrete block.



(d)



(e)



(f)

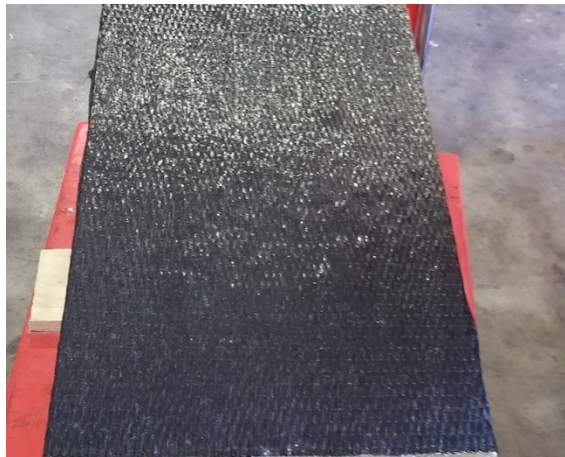


Figure 3-1. a. Schematic of FRP-retrofitted concrete with rebars ; b. formwork preparation; c. concrete pour; d. preparation of carbon fabric and epoxy resin; e. saturating carbon fabric with epoxy resin; and f. applying carbon fibre on concrete specimen

In all experimental measurements, Rayleigh wave signals were actuated by PZT transducers bonded on FRP surface. However, various equipment setups were used based on the conditions and requirements of the signal measurements. Details of the experimental setup have been explained in each following section.

4 Scattering of linear Rayleigh wave

When Rayleigh wave interacts with debonding between FRP and concrete, it is scattered. This chapter investigates the capability of linear Rayleigh wave for debonding detection in FRP-retrofitted concrete structures through studying wave scattering phenomena at debonding between FRP and concrete. A 3D FE model is presented to simulate Rayleigh wave propagation and scattering at the debonding. Numerical simulations of Rayleigh wave propagation are validated with analytical solutions. Absorbing layers are employed in the FRP-retrofitted concrete numerical model to maximise computational efficiency in the scattering study. Experimental measurements are also carried out using a 3D laser Doppler vibrometer to validate the 3D FE model. Very good agreement is observed between the numerical and experimental results. The experimentally and analytically validated FE model is then used in numerical case studies to investigate the wave scattering characteristic at the debonding. This chapter investigates the directivity patterns of scattered linear Rayleigh waves, in both backward and forward directions, with respect to different debonding size-to-wavelength ratios. This chapter; besides; investigates the suitability of using bonded mass to simulate debonding between FRP and concrete. By providing physical insight into Rayleigh wave scattering at the debonding at FRP/concrete interface, further advance of Rayleigh wave-based damage detection in FRP-retrofitted concrete structures can be achieved.

4.1 Finite element model description

In this chapter, the 3D FE model of the FRP-retrofitted concrete structure is consisted of three parts: 1) FRP, 2) concrete, and 3) the absorbing region. This section describes the FRP and concrete modelling. The dimensions of the FRP used in this section are 300mm×600mm

(W×L), and it is attached to the surface of a 300mm×600mm×300mm (W×L×H) concrete block. The 4-ply FRP composite has stacking sequence of [0]4. Each lamina is 0.5mm thick. The elastic properties of each lamina are given in Table 4-1. A mesh converge study was carried out to determine the optimal mesh size. In this section, the FRP is modelled using 2mm×2mm, 4-noded, S4R shell elements with reduced integration. The concrete block is modelled using 2mm×2mm×2mm, 8-noded, C3D8R solid elements with reduced integration. In this study, the body of the steel rebars and PZT transducer are also modelled using the C3D8R elements. The Young's modulus, density and Poisson's ratio of the PZT transducer is 58.8 GPa, 7700 kg/m³ and 0.39, respectively. Tie constraint is used to bond the FRP shell elements and the solid concrete elements. The debonding is created by untying the FRP shell from the concrete solid elements at the debonding area. A schematic diagram of the FE model used in this chapter is shown in Figure 4-1.

Table 4-1. Elastic properties of each FRP lamina

E_{11} (GPa)	E_{22} (GPa)	E_{33} (GPa)	G_{12} (GPa)	G_{13} (GPa)	G_{23} (GPa)
78.86	5.97	5.97	2.15	2.15	2.13
	ν_{12}	ν_{13}	ν_{23}	ρ (kg/m ³)	
	0.336	0.336	0.40	1348	

Based on the literature, a minimum of ten nodes should exist per wavelength to ensure the accuracy of the FE simulated wave signals [101, 114]. In the Section 4.4, the wave velocities from 60kHz to 85kHz are validated with the analytical results. After that, 65kHz excitation frequency is considered for the rest of the chapter. For the excitation frequency ranges from 60kHz to 85kHz, the wavelength is between 24mm and 36mm. Therefore, a mesh size of 2 mm is small enough to ensure the accuracy of simulated Rayleigh wave signals in this frequency

range. The Rayleigh wave is generated by applying nodal displacements in radial direction on the nodes located at the circumference of the PZT transducer top surface. The time step is automatically controlled by ABAQUS.

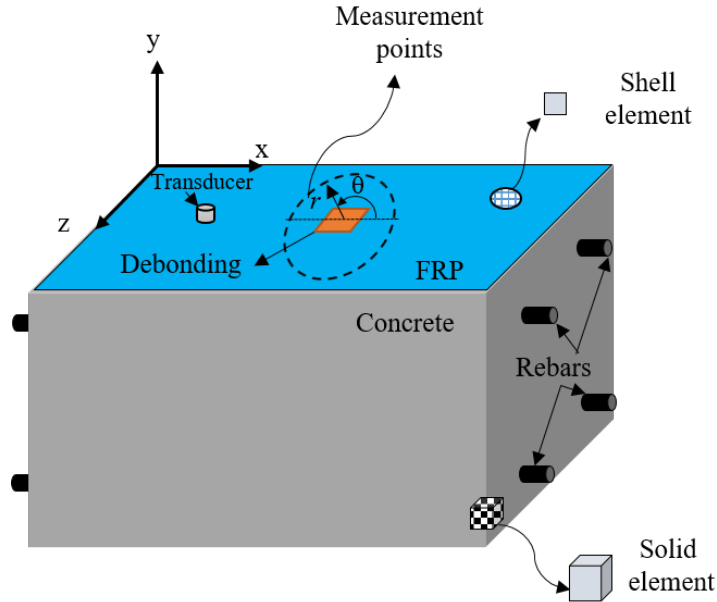


Figure 4-1. Schematic diagram of the FRP-retrofitted concrete FE model

To calculate the group and phase velocities, the out-of-plane nodal displacements are captured at measurement points on the FRP composite. It should be noted that out-of-plane displacement is dominant in Rayleigh wave propagation; therefore, calculations are based on out-of-plane displacements. Group and phase velocity of Rayleigh wave, denoted by C_g and C_p respectively, can be calculated from Equations 7 and 8 in Section 2.1.1. The arrival time of a signal is calculated from a signal envelope obtained by the Hilbert transform.

Figure 4-2 shows snapshots of the out-of-plane displacement contours for the Rayleigh wave propagation and scattering waves at the debonding in the FRP-retrofitted concrete structure. Figure 4-2a displays the propagation of the Rayleigh wave in the FRP-retrofitted concrete model before they reached the debonding at the FRP/concrete interface. After the interaction of

the incident wave with the debonding, the incident wave is transmitted through and reflected back from the debonding as shown in Figure 4-2b. Figure 4-2 demonstrates that the Rayleigh wave is sensitive to the debonding between the FRP and concrete. Therefore, it is feasible to detect the debonding using Rayleigh wave. This highlights the major importance of investigating characteristics of the scattered Rayleigh wave at debonding at the FRP/concrete interface.

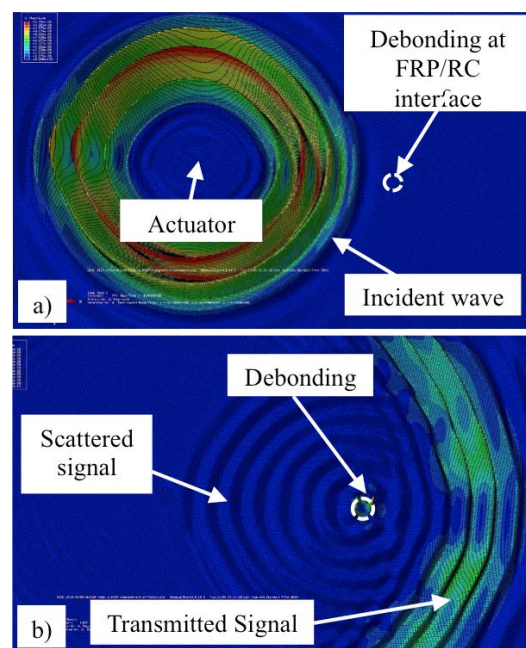


Figure 4-2. Typical contour snapshots of out-of-plane displacement for numerical FRP-retrofitted concrete model with a circular debonding at FRP/concrete interface a. before Rayleigh wave reach debonding; and b. after interaction of Rayleigh wave with debonding.

4.2 Absorbing regions to improve the computational efficiency in scattering analysis

As discussed in Section 4.1, the FE element size was set to 2mm, based on the wavelength of the excited Rayleigh wave. However, the numerical study of the scattered wave characteristics needs to be carried out in an FRP-retrofitted concrete model that is representative of real

conditions, i.e. large size of a structure. Modelling the actual size of a structure results in a large number of FE elements, which is computationally very expensive. Since the wave propagation is a local phenomenon and the purpose of the study is to examine the characteristics of the wave scattered at the debonding, only a section of the FRP-retrofitted concrete model is modelled in the study. Absorbing regions were employed to avoid the reflected wave from the boundaries of the FRP-retrofitted concrete model, and hence, a small section of the FE model can be used to represent a large structure. Therefore, the computational cost can be significantly reduced for investigating the scattering characteristics of the Rayleigh wave at debonding in the FRP-retrofitted concrete structure.

Absorbing layers by increasing damping (ALID) is proposed and implemented in commercial FE software for guided wave problems [39]. In this method, successive layers with gradually increasing values of damping are added to the extremities of a main structure. According to Rayleigh damping relation, damping can be expressed as a linear combination of mass and stiffness as:

$$[C] = \alpha[M] + \beta[K] \quad (27)$$

where α and β denote mass-proportional and stiffness-proportional damping coefficients, respectively. To employ the ALID in explicit FE simulation, stiffness-proportional damping is to be set to zero in order to limit the effects on stable time increment. Then, mass-proportional damping across absorbing layers can be expressed as [38]:

$$\alpha(x) = \alpha_{max}X(x)^P \quad (28)$$

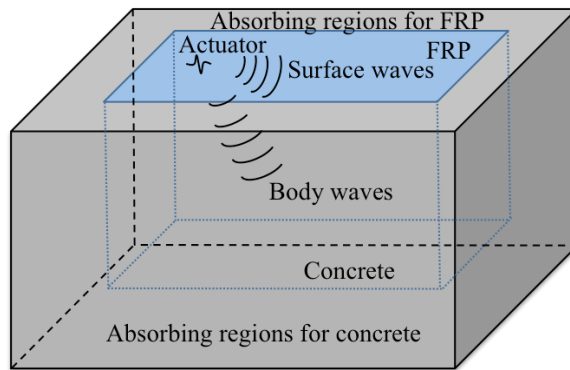


Figure 4-3. Schematic diagram of absorbing regions for wave scattering studies

To implement the absorbing layers in the FRP-retrofitted concrete structure, the ALID was separately applied to the FRP shell element and the concrete solid element models, respectively. For the purpose of the present scattering study, the target of the ALID is to reduce the maximum magnitude of the waves reflected from the boundaries to less than -46 dB. The excitation frequency used in the scattering study was 65kHz. At this frequency, the width of the absorbing region was determined to be 80mm. The absorbing regions were applied to all four sides of the FRP and concrete and also concrete bottom. Each of the absorbing regions had 40 layers of elements with gradually increasing values of damping. The thickness of each layer was 2mm, which was equal to the element size. Using Equation 28, P was set to 3 and α_{max} was 2.5×10^6 . A schematic diagram of the ALID in FRP-retrofitted concrete model is shown in Figure 4-3.

Figures 4-4a to 4-4d show the Rayleigh wave propagation on the FRP-retrofitted concrete with and without absorbing layers. Figure 4-4a and 4-4b show the typical out-of-plane displacement contours for the FE model without absorbing layers. In these figures, both incident wave and boundary reflections are obvious. Figures 4-4c and 4-4d display the out-of-plane displacements in the FE model with absorbing region and they show that Rayleigh wave gradually diminishes in the absorbing layers.

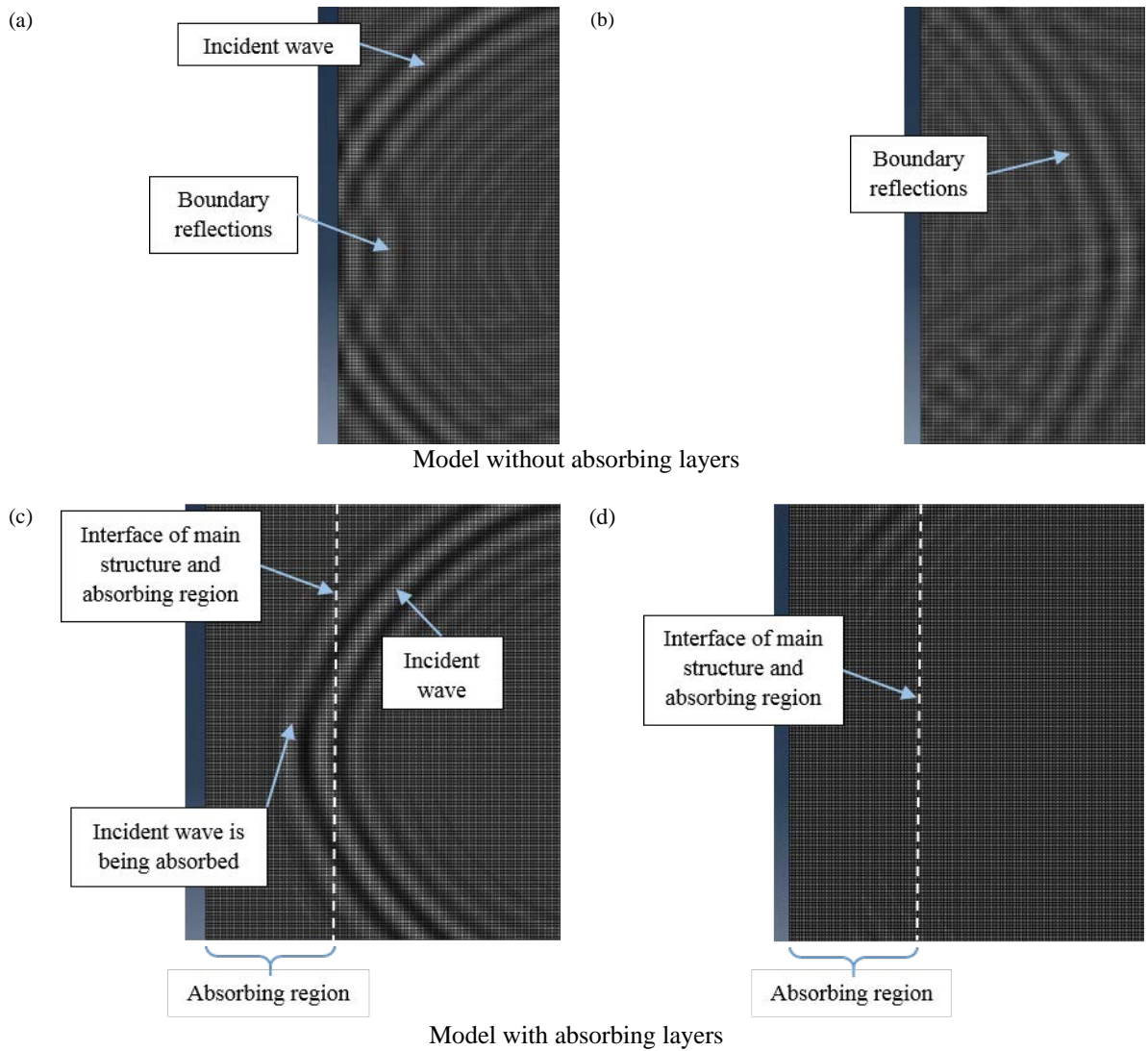


Figure 4-4. Typical contour snapshots of out-of-plane displacement for Rayleigh wave in FRP-retrofitted concrete model without and with absorbing layers a. when the incident wave interacts with the boundary; b. soon after the wave reflection; c. when the incident wave is being absorbed by the absorbing region; and d. soon after the wave absorption.

4.3 Attenuation of Rayleigh wave signals

When the waves propagate in composites, the energy of the wave dissipates due to the viscoelasticity of the waveguide [13]. The attenuation coefficient k_i can be defined by fitting the curve of the signal data using the following relationship [115]:

$$\frac{A_1}{A_2} = \exp(k_i(x_2 - x_1)) \quad (29)$$

where A_1 and A_2 are the wave amplitude at locations x_1 and x_2 respectively. Based on the value of k_i , the mass-proportional and stiffness-proportional damping constants for a particular angular frequency could be calculated as:

$$\alpha_\omega = 2k_i C_g \quad (30)$$

$$\beta_\omega = \frac{2k_i C_g}{\omega^2} \quad (31)$$

where α_ω , β_ω , C_g and ω represent the mass-proportional damping constant, the stiffness-proportional damping constant, the group velocity and the angular frequency, respectively.

4.4 Analytical validation of numerical model

As explained in Section 3.2, DISPERSE program has been used to analytically validate numerical results. One of the main characteristics of Rayleigh wave is signal velocity. Numerical values of group and phase velocity were obtained from FE simulation results. Figure 4-5 compares the group and phase velocities of the FRP-retrofitted concrete structure calculated using FE simulations and DISPERSE. As shown, the group and phase velocities calculated using the FE simulations matches quite well with the results calculated from DISPERSE.

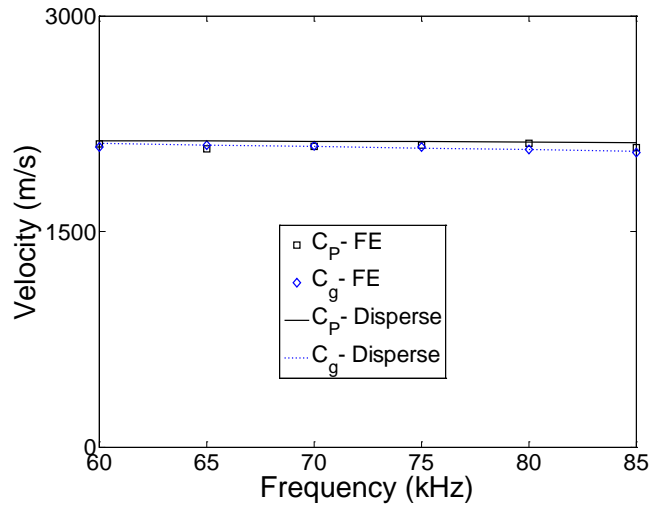


Figure 4-5. Numerical and analytical values of group and phase velocity

To further validate the FE results, the in-plane and out-of-plane displacement mode shapes of Rayleigh wave at the frequency of 65kHz are compared and verified with DISPERSSE. The results are shown in Figure 4-6. The mode shapes indicate the deformation along the thickness direction during the Rayleigh wave propagation in the FRP-retrofitted concrete. The Rayleigh wave mode shapes shown in Figure 4-6 were obtained by capturing both in-plane and out-of-plane displacements at vertical measurement points along a cross-section of the FRP-retrofitted concrete. As expected, the deformation of the Rayleigh wave is concentrated on the surface of the waveguide, which is consistent with the nature of the Rayleigh wave, i.e. wave travel along the surface of the solids. Figures 4-5 and 4-6 show that there is good agreement between the results calculated by FE and DISPERSSE.

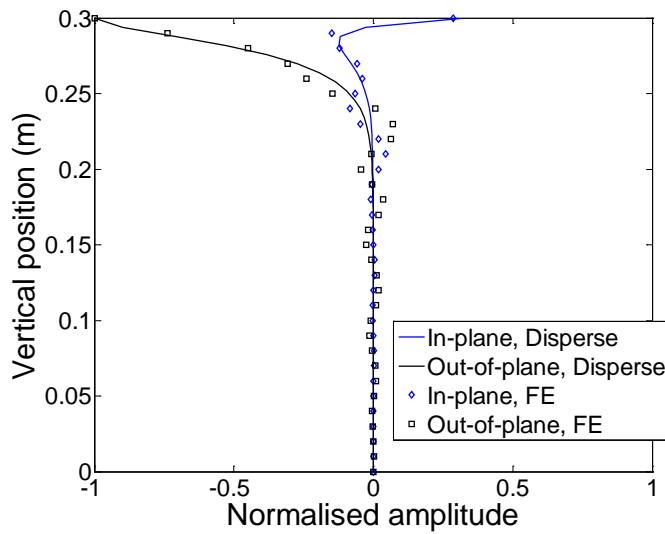


Figure 4-6. Analytical and numerical mode shapes for FRP-retrofitted concrete model

4.5 Experimental validation

4.5.1 Equipment setup

The Rayleigh wave were generated and measured using a PZT transducer and a Polytec PSV-400-3D laser Doppler vibrometer, respectively. The laser Doppler vibrometer system includes a data management system, three sensor heads and vibrometer controllers, and a junction box as schematically shown in Figure 4-7. The data management system PSV-W-400 incorporates a computer, a built-in signal generator, and a data acquisition unit. The excitation signal was a narrow-band 5-cycle sinusoidal tone burst pulse modulated by a Hanning window. The central frequency of the excitation signal was 65kHz, which ensures minimum reflections from the concrete aggregates [116]. The signal was generated at 4.3V, which was amplified four times by a Playmaster SERVO amplifier before being sent to the actuator. The actuator was a 10mm diameter circular and 2mm thick PZT transducer bonded on the FRP surface. The Rayleigh wave signals were sensed by three PSV-I-400 sensor heads controlled by the OFV-5000 vibrometer controllers. The interface between the sensor heads, vibrometer controllers, and data

management system was provided by a PSV-E-400 junction box. The sampling frequency of the measurement system was set to 2.5MHz. To improve the signal quality and reduce the signal-to-noise ratio (SNR), an averaging of 2000 times of the signals was carried out. The acquired data was fed into the computer, from which output results were obtained.

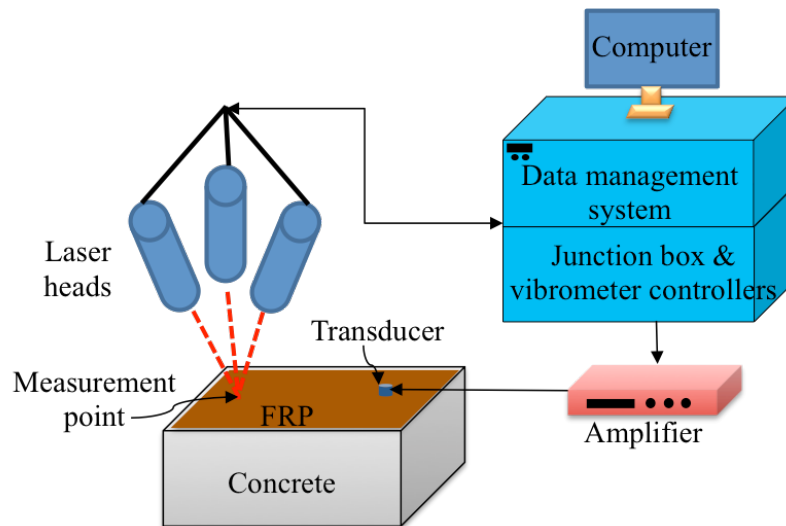


Figure 4-7. Schematic diagram of the experimental setup using 3D laser

4.5.2 Validation of Rayleigh wave propagation

To experimentally validate the accuracy of the FE model, the 3D laser Doppler vibrometer was used to measure the Rayleigh wave signals. The measured data was then compared with the FE simulation results. To ensure the numerical and experimental results can be compared directly, the maximum absolute amplitude of signals was normalised to be one. In this chapter, the FRP-retrofitted concrete was modelled in FE with real dimensions; i.e. four layers of 300mm×600mm FRP bonded on 300mm×600mm×300mm concrete. Since the arrival time and magnitude of the boundary reflections needed to be verified with experiments, absorbing layers were not applied to the FE models in the experimental validation.

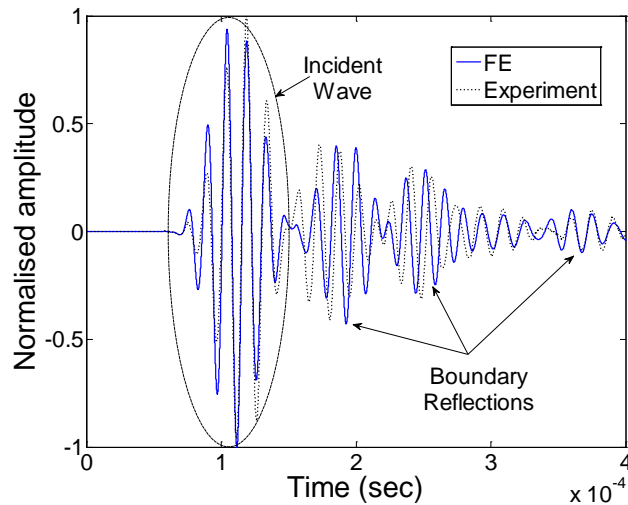


Figure 4-8. FE calculated and experimentally measured Rayleigh wave signals for concrete specimen 1 (without rebar)

Concrete Specimen 1, which has no rebar and no debonding at the FRP/RC interface, is used to verify the Rayleigh wave propagation. Based on the Cartesian coordinate system shown in Figure 4-1, Rayleigh wave was actuated at $x = 516\text{mm}$ and $z = 190\text{mm}$. The out-of-plane displacements were measured at $x = 376\text{mm}$ and $z = 190\text{mm}$. As shown in Figure 4-8, there is good agreement between the FE calculated and experimentally measured results.

Reinforcement in concrete is usually in the form of steel bars; therefore, the FE model with rebar needs to be experimentally verified. As explained in Section 3.3, the concrete specimen 2 has longitudinal steel bars. The dimensions of the numerical model and the experimental specimen are the same, and absorbing layers were not applied to the FE model. There was no debonding in the FRP-retrofitted concrete structure. The Rayleigh wave was generated at $x = 170\text{mm}$ and $z = 120\text{mm}$. The out-of-plane displacements were sensed at $x = 120\text{mm}$ and $z = 120\text{mm}$ using the 3D laser Doppler vibrometer. A very good agreement on the arrival time and magnitude is observed between the numerically simulated and experimentally measured signals as shown in Figure 4-9.

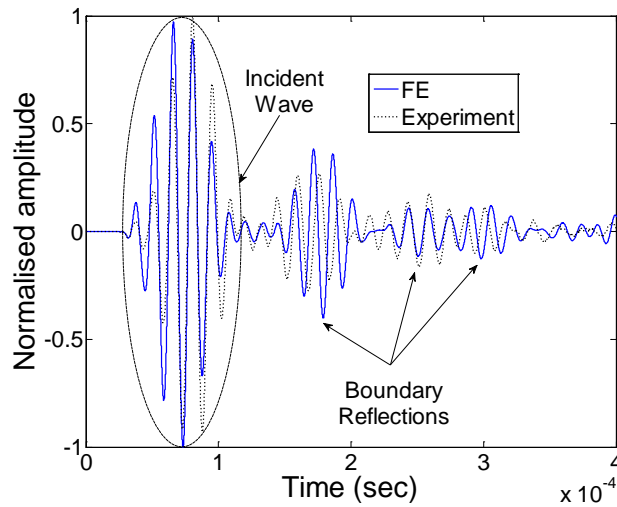


Figure 4-9. FE calculated and experimentally measured Rayleigh wave signals for concrete specimen 2 (with rebar)

A polar directivity plot of the maximum absolute amplitude of the incident wave is shown in Figure 4-10. The out-of-plane displacements were sensed at 36 points, with a circular path of $r = 50\text{mm}$, $0^\circ \leq \theta \leq 360^\circ$, and step increments of 10° . The PZT transducer was located at the centre of the circular path. Figure 4-10 shows the amplitude of the excited Rayleigh wave in different propagation directions. Since the concrete is retrofitted by 4-ply unidirectional FRP on the surface, the amplitude distribution of the Rayleigh wave has anisotropic behaviour. To compare the numerical with experimental results, the amplitude at each point is normalised to the maximum absolute amplitude of all points. As shown in Figure 4-10, there is good agreement between the numerical and the experimental results. Figure 4-11 shows the setup of experimental measurements using 3D laser Doppler vibrometer.

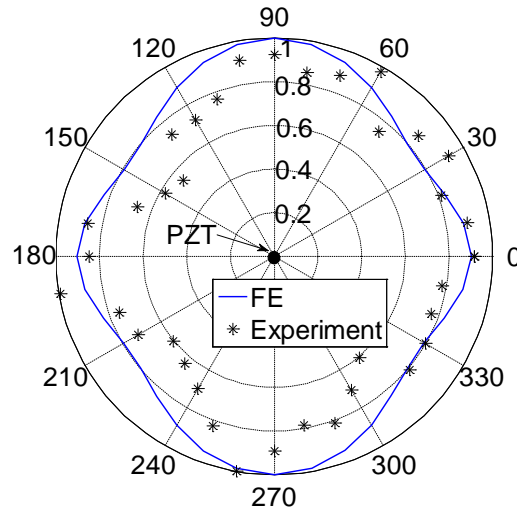


Figure 4-10. Polar directivity of the normalised amplitude of Rayleigh incident wave measured on a circular path with $r = 50\text{mm}$, $0^\circ \leq \theta \leq 360^\circ$ and the actuator located at the centre.

To investigate the attenuation of Rayleigh wave in FRP-retrofitted concrete, the out-of-plane displacements were measured at $20\text{mm} \leq r \leq 160\text{mm}$ away from the PZT transducer, along the direction $\theta = 0^\circ$. Because of the possible non-uniformity of the FRP-retrofitted concrete specimen, four different locations of the PZT transducer were considered. The wave signal at each measurement point was normalised by the maximum absolute amplitude of the signal at $r = 20\text{mm}$, so that the numerical and experimental results could be compared. Figure 4-12 shows the normalised maximum amplitude of the incident wave signals as a function of the distance from the PZT transducer. Using Equation 29, the attenuation coefficient for this FRP-retrofitted concrete structure is $k_i = 2.87\text{Np/m}$. Considering Equations 30 and 31, the calculated damping constants are $\alpha_\omega = 12,065\text{rad/s}$ and $\beta_\omega = 7.234 \times 10^{-8}\text{s/rad}$.

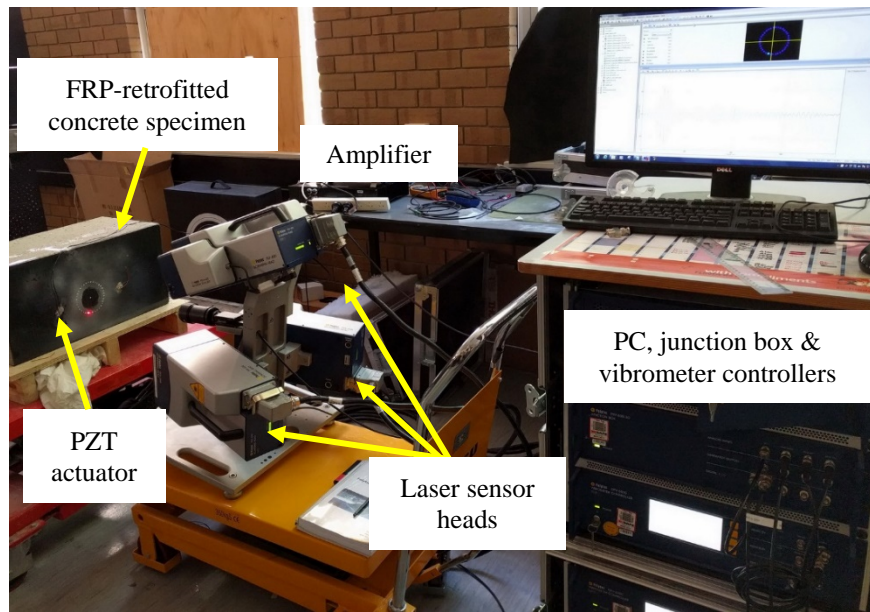


Figure 4-11. Experimental measurements using 3D laser Doppler vibrometer

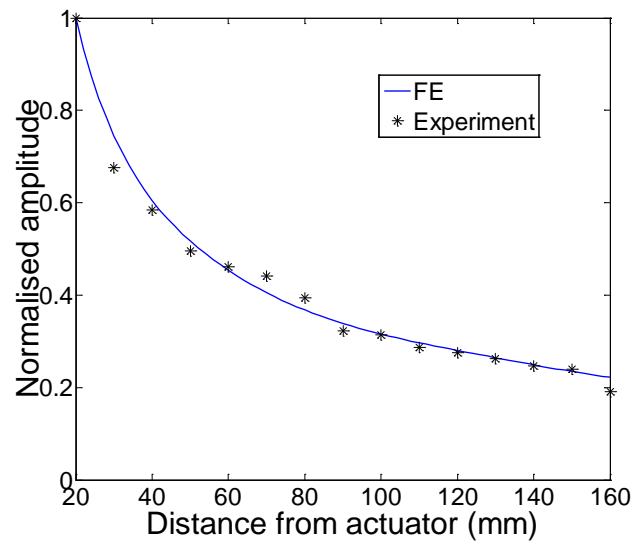


Figure 4-12. Attenuation of Rayleigh waves in FRP-retrofitted concrete.

4.5.3 Rayleigh wave scattering at bonded mass

To further validate the 3D FE model, experimental measurements are also used to validate the Rayleigh wave scattering phenomenon. In this section, the accuracy of the 3D FE model in predicting the scattering waves are investigated by means of the scattering directivity pattern (SDP) [117], which displays the maximum amplitude of the scattered signal as a function of the angular direction of the measurement points. To obtain the scattered wave signals for calculating the SDP, it requires the baseline data obtained from undamaged structures for extracting the scattered wave signals. Although this is practical in real SHM applications, it is hard to obtain the baseline data for delamination/debonding type of damage in the wave scattering study. Therefore, the bonded mass is used to verify the accuracy of the 3D FE in predicting the SDP. In addition, the damage has been frequently simulated bonding masses to surface of the structures for verification of damage detection method [43, 118]. It is still an open question whether or not the debonding can be well represented by bonding masses to the surface of the retrofitted concrete structure. The suitability of using bonded mass to represent the debonding is also investigated.

Based on the polar coordinate system shown in Figure 4-1, the PZT transducer was located at $r = 110\text{mm}$ and $\theta = 180^\circ$. The out-of-plane displacements were sensed by the 3D laser Doppler vibrometer at 36 points on a circular path with $r = 50\text{mm}$, $0^\circ \leq \theta \leq 360^\circ$ and step increments of 10° . The measurements were obtained before and after a 40mm cubic steel mass bonding onto the FRP with the centre of the mass area located at $r = 0\text{mm}$ and mass edges parallel to the x or y axis. The measured signal at each point was normalised by the maximum absolute amplitude of the signal at $\theta = 180^\circ$ in the model without the bonded mass. After that,

the scattered waves were obtained by subtracting the signals without the bonded mass from the signals with the bonded mass. The magnitudes of the scattered waves at different directions are then calculated and represented by the SDP. In the FE simulations, the same measurement location and excitation frequency are used. The bonded mass was modelled in FE simulation using C3D8R solid elements with the same dimensions and mechanical properties as the bonded mass used in the experiments. Two simulations, one with bonded mass and the other without the bonded mass, were carried out to obtain the scattered wave signals for calculating the SDP.

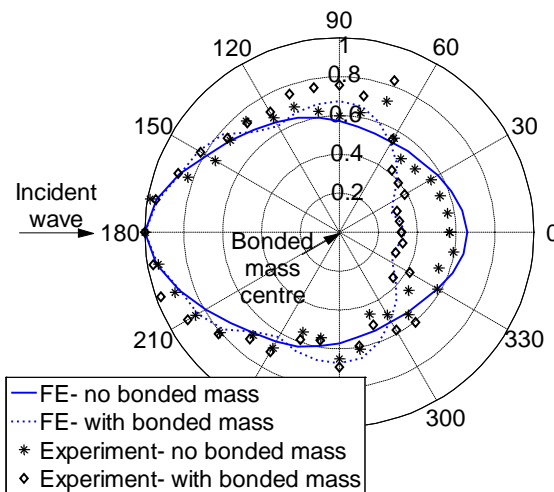


Figure 4-13. Normalised polar directivity pattern for the measured signal, with and without cubic 40mm bonded mass.

Figure 4-13 compares the FE simulated with experimentally measured signals before and after bonding the mass on the FRP. The numerical results match quite well with the experimental results. As shown in Figure 4-13, the bonded mass has the maximum effect on the measured signal, from angle $\theta = 60^\circ$ to $\theta = 300^\circ$ (clockwise) with a reduction of up to 50% in wave magnitude. The scattered signal at each measurement point is the difference between the baseline signal (without a bonded mass) and the signal measured with the mass bonded. Figure

4-14 shows the Rayleigh wave SDP for the 40mm cubic bonded mass. The figure shows amplitude of the scattered wave in different directions, which indicates the energy distribution of the scattered wave signals. There is good agreement between the FE results and the experimental measurements. The results show that the maximum magnitude of scattering waves is around 0.35 and 0.20 for forward and backward scattering direction, respectively. As shown in Figure 4-14, the scattered wave energy concentrates in the forward scattering direction.

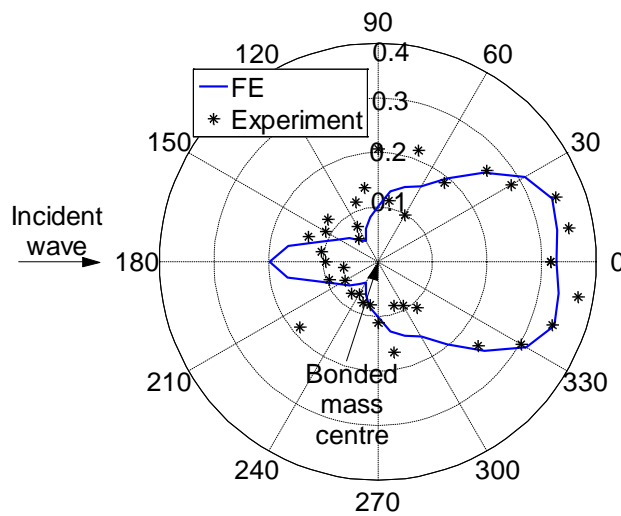


Figure 4-14. SDP for a cubic 40mm bonded mass.

4.6 Scattering of Rayleigh wave at debonding at FRP/concrete interface

Experimental verifications of the numerical models have been presented in Section 4.5. It has been demonstrated that the 3D FE model can precisely simulate the propagation of Rayleigh wave in FRP-retrofitted concrete structures and scattering of wave at the bonded mass. Also, group and phase velocity and mode shapes of Rayleigh wave have been analytically verified in Section 4.4. The experimentally and analytically validated 3D FE model is then used to study the scattering characteristics of Rayleigh wave at the debonding at FRP/concrete interface in this section.

4.6.1 Effect of rebars

To investigate the effects of embedded steel rebars on Rayleigh wave propagation, two FRP-retrofitted concrete models are considered: one with rebars, and the other without rebars. The Rayleigh wave was generated at $x = 170\text{mm}$ and $z = 120\text{mm}$. The out-of-plane displacements were measured at $x = 120\text{mm}$ and $z = 120\text{mm}$. In the model with rebars, reflections can come from both rebars and boundaries. As explained in Section 4.2, absorbing layers were applied to all boundaries of both models to remove all boundary reflections. Therefore, only the incident waves and the rebar reflections can be seen in the signals. As illustrated in Figure 4-15, the rebars have a minor effect on the incident waves, and only cause some reflections of body waves. It means that in Figure 4-9, the first reflected signal coming after the incident wave is a combination of the rebar reflections and boundary reflections. The rebar reflections exist in the signals of both intact model and the model with the debonding. Since the baseline subtraction method [119, 120] is applied to obtain scattered wave signals from the debonding, the rebar reflections have a minimal effect on the scattered waves.

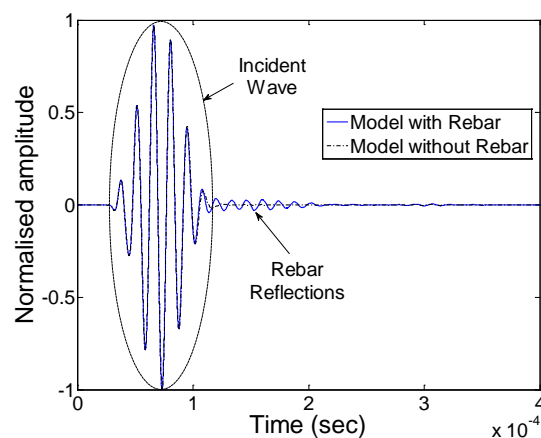


Figure 4-15. Effect of rebars on Rayleigh wave propagation.

4.6.2 Effect of debonding size and shape

According to the polar coordinate system shown in Figure 4-1, Rayleigh wave is actuated at $r = 110\text{mm}$ and $\theta = 180^\circ$. For each debonding case, two sets of FE simulations were performed, one without debonding and the other with debonding. The scattered signal was obtained by subtracting the signals of the model without the debonding from the model with the debonding [121]. Absorbing layers were applied in all FE models. Two different shapes of debonding, rectangular and circular debonding, are considered in this study. To examine effects of the debonding size on the scattering wave, results are presented in terms of R_{DW} . For rectangular and circular debonding, R_{DW} is defined as the ratio of the debonding size to wavelength, and the debonding diameter to wavelength, respectively. The wavelength of Rayleigh wave at the frequency of 65kHz is around 32mm. Rectangular debondings with sizes and circular debondings with diameters of 10, 16, 20, 24, 30, 36, 40, 44, 50, 56 and 60mm are considered in this section.

For all rectangular debonding cases considered in this study, the centre of the debonding area is located at $r = 0\text{mm}$ and debonding edges are parallel to the x - or y -axis. The out-of-plane displacements are measured at 36 points, at $r = 50\text{mm}$, $0^\circ \leq \theta \leq 360^\circ$ at intervals of 10° . The signal at each measurement point is normalised by the maximum absolute amplitude of the incident wave at $r = 50\text{mm}$ and $\theta = 180^\circ$. Figure 4-16 displays the SDP for 40mm×40mm rectangular and 40mm diameter circular debonding. It has been shown that the amplitude of the forward scattering direction is larger than that of the backward scattering direction. The amplitude distribution of the forward scattering waves is quite similar for both rectangular and circular debonding. The maximum amplitude of the forward scattering wave occurs at $\theta = 0^\circ$

with magnitudes of 0.298 and 0.272 for rectangular and circular debonding, respectively. The maximum amplitude of the backward scattering occurs at $\theta = 180^\circ$, with magnitudes of 0.091 and 0.046 for rectangular and circular debonding, respectively.

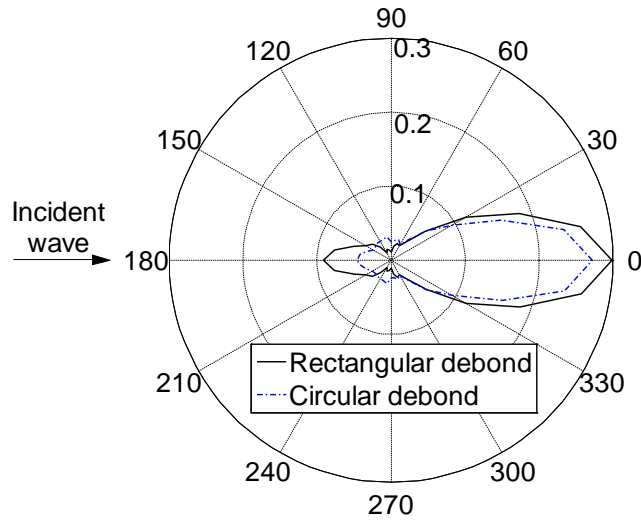


Figure 4-16. SDP for 40mm×40mm rectangular debonding and 40mm diameter circular debonding.

To demonstrate the effects of debonding size and shape on the scattering phenomenon, the normalised forward and backward scattering amplitude of rectangular and circular debondings are displayed as a function of R_{DW} in Figures 4-17 to 4-20. The forward scattering results are presented in Figures 4-17 and 4-18 at $\theta = 90^\circ, 60^\circ, 30^\circ, 0^\circ, 330^\circ, 300^\circ$ and 270° . The backward scattering results are presented in Figures 4-19 and 4-20 at $\theta = 90^\circ, 120^\circ, 150^\circ, 180^\circ, 210^\circ, 240^\circ$ and 270° .

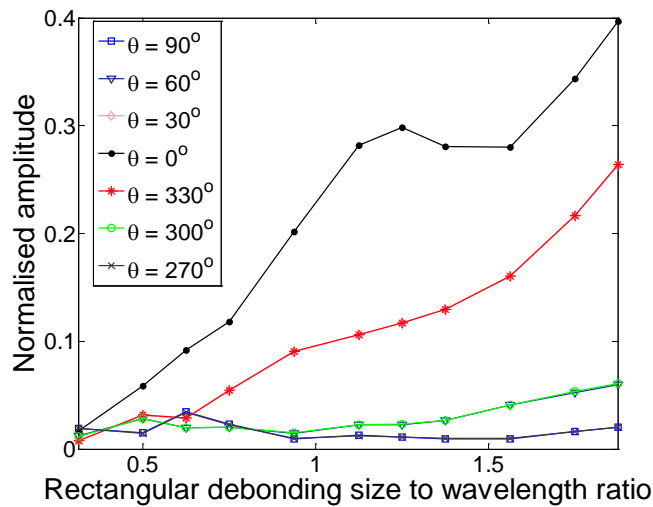


Figure 4-17. Normalised amplitude for the forward scattering of rectangular debonding as a function of debonding size to wavelength ratio.

Figure 4-17 displays the normalised amplitude of the forward scattering wave for rectangular debonding as a function of debonding size to wavelength ratio. At $\theta = 0^\circ$, the scattering amplitude rises quite sharply to 0.298 at $R_{DW} = 1.25$ and then falls slightly to 0.280 at $R_{DW} = 1.563$. After that, it increases sharply again to 0.397. For $\theta = 30^\circ$ and 330° , the amplitude increases steadily to 0.263 with a small decrease at $R_{DW} = 0.50$. The magnitudes of the scattering amplitude at $\theta = 60^\circ$ and 300° , and $\theta = 90^\circ$ and 270° exhibit moderate fluctuations with R_{DW} .

Figure 4-18 shows the normalised amplitude of the forward scattering of circular debonding as a function of the debonding diameter to wavelength ratio. The amplitude at $\theta = 0^\circ$ increases constantly to a peak of 0.360. The rise in amplitude is sharper for $R_{DW} \leq 1.375$. For $\theta = 30^\circ$ and 330° , the amplitude rises steadily to 0.193 except for a small decline at $R_{DW} = 0.50$. The forward scattering amplitudes at $\theta = 60^\circ$ and 300° , and $\theta = 90^\circ$ and 270° show a similar trend to those of the rectangular debonding. For both rectangular and circular debondings, the forward scattering amplitudes at $\theta = 60^\circ$ and 300° , and $\theta = 90^\circ$ and 270° are considerably smaller than

those at $\theta = 0^\circ$, $\theta = 30^\circ$ and 330° especially for larger values of R_{DW} . Therefore, selecting an appropriate measurement direction is critical in the damage detection.

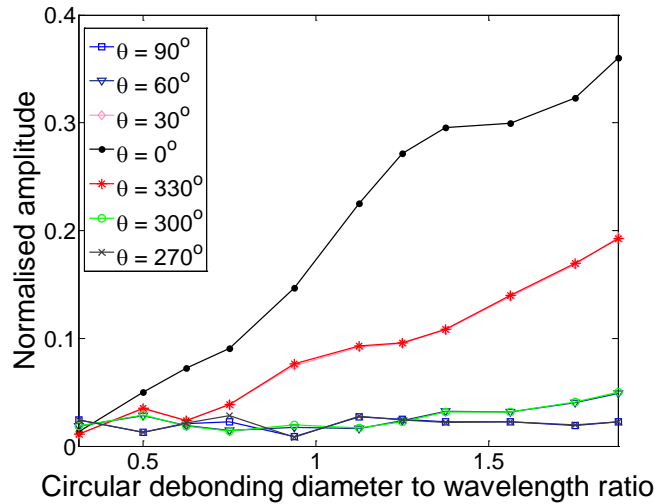


Figure 4-18. Normalised amplitude for the forward scattering of circular debonding as a function of debonding diameter to wavelength ratio.

The normalised amplitude for backward scattering of rectangular debonding as a function of debonding size to wavelength ratio is shown in Figure 4-19. It is obvious that the overall trend of the backward scattering is quite different to that of the forward scattering. For $\theta = 180^\circ$, which is along the incident wave direction, the backward scattering amplitude first rises to a local peak and then drops at $R_{DW} = 0.625$. The amplitude then increases steeply to a peak of 0.092 at $R_{DW} = 1.25$, and decreases sharply to 0.056. After this point, it increases gradually to 0.070. The trend at $\theta = 150^\circ$ and 210° is of a slow increase with moderate fluctuations. The amplitude at $\theta = 120^\circ$ and 240° shows some variations without a dominant trend.

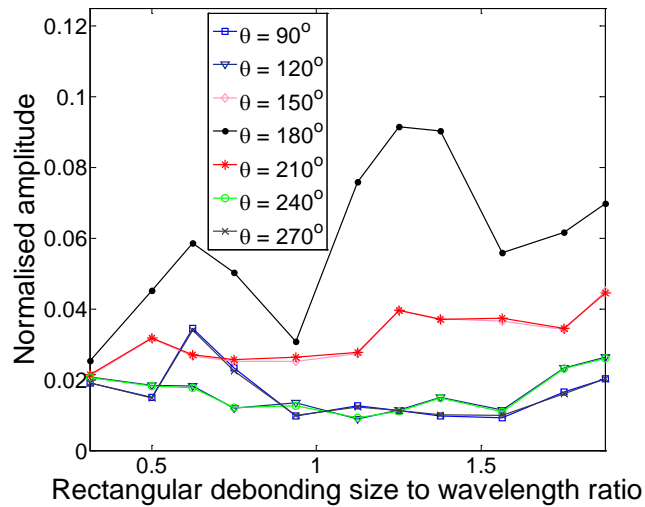


Figure 4-19. Normalised amplitude for the backward scattering of rectangular debonding as a function of debonding size to wavelength ratio.

Figure 4-20 shows the normalised amplitude of the backward scattering for circular debonding as a function of debonding diameter to wavelength ratio. For $\theta = 180^\circ$, the amplitude rises dramatically and then falls sharply at $R_{DW} = 0.5$. The amplitude then has an increasing trend with fluctuations. The amplitude at $\theta = 150^\circ$ and 210° starts with a rapid increase and a sharp decline at $R_{DW} = 0.5$. Then, an increasing trend is observed and it reaches a peak at $R_{DW} = 1.75$. For $\theta = 120^\circ$ and 240° , the amplitude shows a gradual decrease for R_{DW} less than 0.938 and then they have moderate fluctuations. In general, the magnitudes of the backward scattering amplitude at $\theta = 120^\circ$ and 240° are smaller than those at $\theta = 180^\circ$, $\theta = 150^\circ$ and $\theta = 210^\circ$.

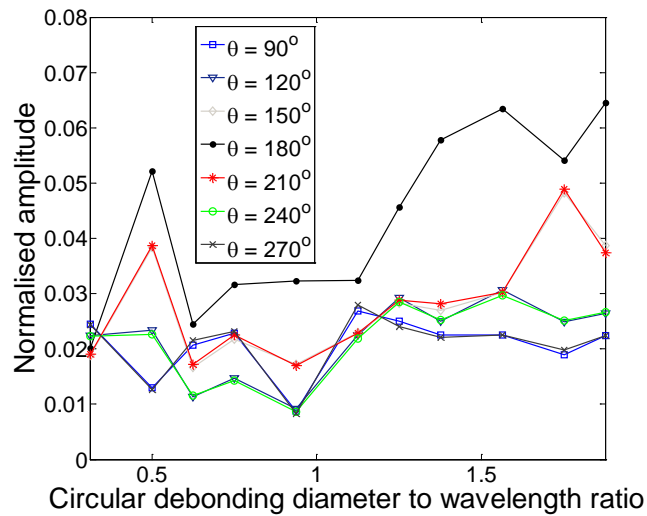


Figure 4-20. Normalised amplitude for the backward scattering of circular debonding as a function of debonding diameter to wavelength ratio.

For both rectangular and circular debondings, a major, increasing trend is obvious for the forward scattering amplitude at the same direction of the incident wave ($\theta = 0^\circ$) and also at $\theta = 30^\circ$ and 330° . The trend for the backward scattering is complicated and shows some fluctuations. It is shown that Rayleigh wave are sensitive to the debonding between FRP and concrete. However, measurement direction should be chosen appropriately in the damage detection.

5 Scattering of nonlinear Rayleigh wave

This chapter investigates higher harmonic generation of Rayleigh waves in FRP-retrofitted concrete structures due to debonding between FRP and concrete. As discussed in Section 2.2.10, the use of ultrasonic nonlinearity for damage detection and monitoring of structures has attracted growing attention. Interaction of guided waves with contact-type damage, such as debonding, is one of the major sources of ultrasonic nonlinearity. In this chapter, propagation and scattering of Rayleigh wave are simulated using a 3D FE model. The numerical simulations of both linear and nonlinear Rayleigh wave are validated with experimentally measured data. There is very good agreement between numerical and experimental results. This chapter also investigates the scattering directivity patterns of second and third harmonics of Rayleigh wave. The results provide physical insights into nonlinear Rayleigh wave generated by debonding between FRP and concrete.

5.1 Numerical model

The explicit module of ABAQUS version 6.14 was used to simulate the actuation and propagation of Rayleigh waves in FRP-retrofitted concrete structures. The dimensions of the 4-ply FRP composite are 300mm×400mm (W×L) and the thickness of each ply is 0.5 mm. The stacking sequence of the FRP composite is [0]₄. The elastic properties of each lamina are shown in Table 4-1. The FRP was meshed using 1mm×1mm S4 shell elements. The dimensions of the concrete block are 300mm×400mm×150mm (W×L×H). The concrete was meshed using 1mm×1mm×1mm C3D8 solid elements. This element size ensures the accuracy of the numerical simulations for the linear and nonlinear Rayleigh wave. The FRP and concrete are connected by tie constraint. The debonding was created by removing the tie constraint over

debonding area. A surface-to-surface frictionless hard contact was used to simulate clapping effect at the debonding. Figure 4-1 in Section 4.1 shows the schematic diagram of the FE model.

The Rayleigh wave was actuated by applying radial displacements on nodes located on the circumference of the upper surface of a 2 mm thick and 10 mm diameter circular PZT transducer. Mechanical properties of PZT transducer are the same as mentioned in Section 4.1. The PZT transducer was meshed using C3D8 solid elements in the FE model. The excitation signal is a 15-cycle tone burst modulated by a Hanning window. The central excitation frequency for both numerical simulations and experimental measurements is 95 kHz. Since the out-of-plane motion is dominant in the Rayleigh wave propagation, the wave signals were measured based on out-of-plane nodal displacements at measurement points on FRP composite.

5.2 Validation of numerical model

5.2.1 Analytical verification

Similar to Section 4.4, DISPERSE has been used for analytical validation of the FE model. This solution employs the global matrix method, which is based on consistency of displacements and stresses at interfaces of layers. Therefore, propagation of Rayleigh wave in the FRP-retrofitted concrete model without debonding can be theoretically validated. In this section, the phase velocity of Rayleigh wave in FRP-retrofitted concrete model is obtained by DISPERSE and compared with the FE results as shown in Figure 5-1. There is good agreement between numerical and analytical results

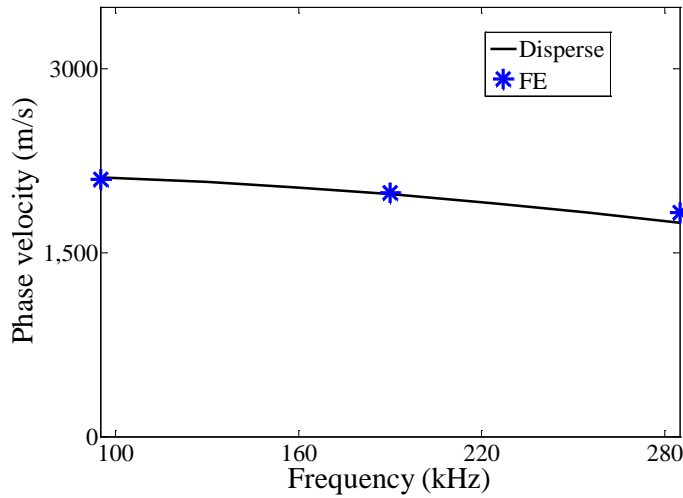


Figure 5-1. Numerical and analytical results of the Rayleigh wave phase velocity

5.2.2 Equipment setup

The concrete specimen 3 was used for experimental verification in this chapter. A 2mm thick and 10 mm diameter circular PZT transducer was used to actuate Rayleigh wave. The PZT transducer is made of Ferroperm Pz27, which has the same mechanical properties described in Section 4.1. The actuator was bonded to the FRP surface at $x = 200\text{mm}$ and $z = 150\text{mm}$. The excitation signal is a 15-cycle tone burst modulated by a Hanning window wave, which is the same as the excitation signal used in the FE simulation. The excitation signal was generated by a Tektronix AFG 3021B arbitrary function generator. The amplitude of the generated signal was 10V (peak-to-peak), which was then amplified five times by a KROHN-HITE 7500 amplifier. The Rayleigh wave signals were measured using Polytec PSV-400 1D laser Doppler vibrometer system. The laser head controlled by vibrometer controller captured the out-of-plane displacements. The data was recorded by a data acquisition unit and fed into the PC. The sampling frequency of the measurement was set to 10.24 MHz. A bandpass filter of frequency band 10kHz-600kHz was applied to the measured signals. Considering the excitation frequency

of 95 kHz, the frequency band of the bandpass is wide enough to capture the higher harmonics. In order to increase the signal-to-noise ratio, an averaging of 5000 times was applied to the measured signals. A schematic diagram of the experimental setup is shown in Figure 5-2.

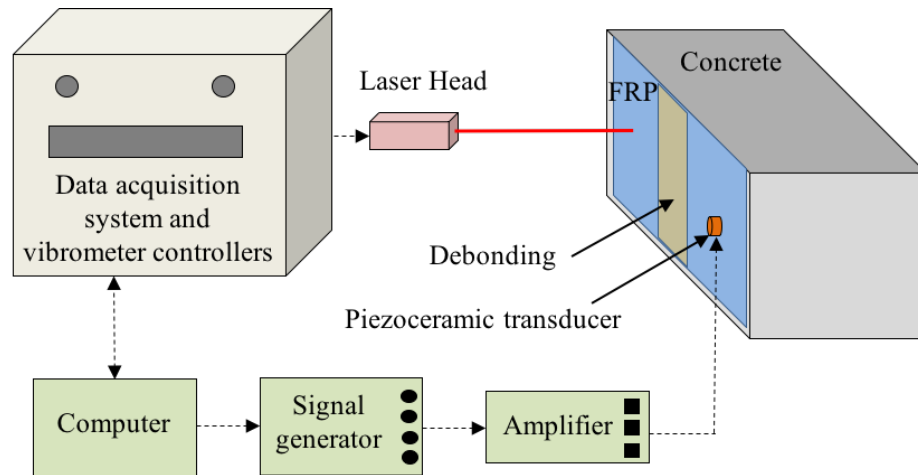


Figure 5-2. Schematic diagram of experimental setup

5.2.3 Higher harmonics generation due to contact nonlinearity at debonding

The results of the FE model need to be verified by experimental measurements. However, if the FE model with the element size of 1 mm has the same dimensions as the test specimen, the required computational cost will be extremely high. Therefore, a 300mm×400mm FRP bonded to 300mm×400mm×150mm concrete was used as the FE model in the experimental verification. For the numerical model in this section, the debonding is 40mm×300mm with left and right end at $x = 180\text{mm}$ and $x = 220\text{mm}$, respectively, and across the whole width of the concrete block. Based on the cylindrical coordinate shown in Figure 4-1, the actuator is located at $r = 100\text{mm}$ and $\theta = 180^\circ$ away from the debonding centre. For both FE simulation and experiment, the measurement point is at $r = 50\text{mm}$ and $\theta = 0^\circ$ away from the debonding centre. Figure 5-3 compares the FE simulated with experimentally measured Rayleigh wave signals in the time-domain. There is good agreement between numerical and experimental results.

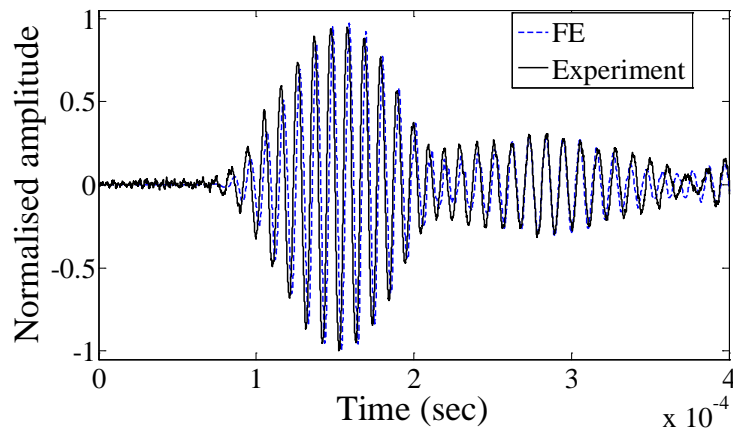


Figure 5-3. Experimental validation of FE simulated linear Rayleigh wave results

To compare the generated higher harmonic due to the contact nonlinearity at the debonding of the numerical and experimental signals, the measured time-domain signals are transformed to frequency-domain using FFT. The measured time-domain signals contain incident wave and reflected wave from boundaries. Thus, the scattered wave from the debondings caused by the incident wave and wave reflected from boundaries can contribute to the generation of higher harmonics in the frequency-domain. As explained above, the FE model has the same width but smaller length than experimental specimen. Therefore, the reflected wave from the boundaries in FE simulation are different to the experiment. On the other hand, the location of the actuator and the measurement point with respect to the debonding is similar in the FE simulation and experiment. Considering the actuator/sensor arrangement, the FE model is large enough to separate incident waves reflected from boundaries; therefore, the higher harmonics induced by the incident wave do not mix with the boundary reflections. In this study, the signal obtained at the measurement point only contains incident wave and also the scattered signal from the debonding. Therefore, the higher harmonics can be compared between the numerically calculated and experimentally measured data.

In addition to the contact nonlinearity, higher harmonics in the measured Rayleigh wave signals can be caused by experimental instrument and also nonlinearity of materials. It has been shown that the instrument nonlinearity has a negligible effect on higher harmonics of the experimentally measured Rayleigh waves [122, 123]. Furthermore, it has been proved that contact nonlinearity has a dominant contribution to higher harmonic generation than material nonlinearity [124]. Therefore, it is assumed that the experimentally measured higher harmonics in this study are mainly due to contact nonlinearity at the debonding between the FRP and concrete interface.

To investigate the higher harmonics, the measured signals were transformed from time-domain to the frequency-domain using FFT. It should be noted that the FFT was only applied to the signal from $t = 0$ until $t = 2.3 \times 10^{-4}$ sec. This ensures the higher harmonics in the signals are only due to the incident wave interaction with the debonding. Within the time duration, the signal mainly contains incident wave and scattered wave from the debonding caused by the incident wave. Figure 5-4 shows the normalised FFT amplitude of numerically calculated and experimentally measured signals. Considering the excitation frequency of 95 kHz, the second harmonic and third harmonic frequency are 190 kHz and 285 kHz, respectively. As shown in Figure 5-4, there is good agreement between the numerical calculated and experimentally measured second and third harmonic magnitude.

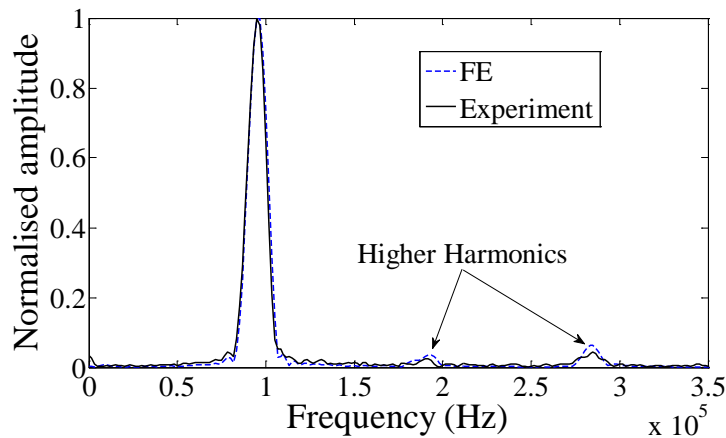


Figure 5-4. Experimental validation of FE simulated higher harmonics

5.2.4 Accuracy of the element type in simulating higher harmonics

The results of the FE model with S4 and C3D8 elements were proved to have good agreement with the experimental measurements. To investigate the accuracy of the reduced integration elements in the higher harmonic prediction, FE simulations were carried out using reduced integration elements with hourglass effect, i.e. S4R shell elements for the FRP and C3D8R solid elements for the concrete. Figure 5-5 compares the FFT results simulated by the FE model with full and reduced integration elements, and also the experimental results. As shown in Figure 5-5, the FE results with the reduced integration elements have some discrepancies between the numerically calculated and experimentally measured second harmonic. Therefore, it is not preferred to use elements with reduced integration for simulating higher harmonics generation of Rayleigh wave.

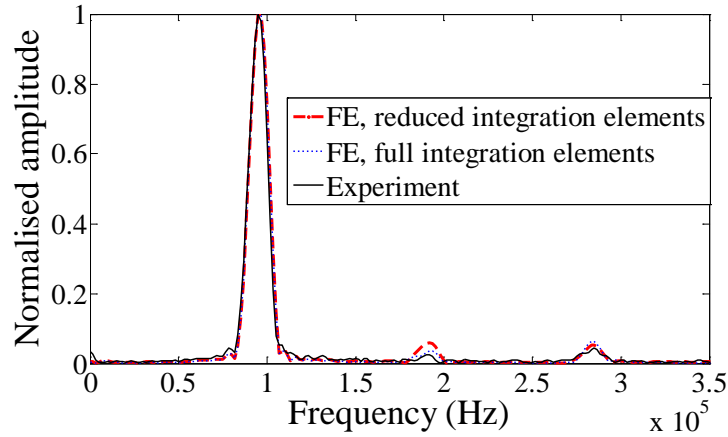


Figure 5-5. Comparison between the FE simulations using reduced integration elements and full integration elements

5.3 Directivity patterns of higher harmonics generated at debondings

The experimentally and theoretically validated FE model is used in the parametric studies. Based on the cylindrical coordinate system shown in Figure 4-1, the Rayleigh wave is generated at $r = 100\text{mm}$ and $\theta = 0^\circ$. Considering the Cartesian coordinate in Figure 4-1, the actuator is located at $x = 100\text{mm}$ and $z = 150\text{mm}$. Rectangular debondings with sizes of 8, 14, 22, 30, 38 and 44mm are considered in the case studies. In all debonding cases, the centre of the debonding is located at $r = 0\text{mm}$ and the debonding edges are parallel to the x - and z -axis. To study the effect of the debonding size on the directivity pattern of the generated higher harmonics, the results are presented in terms of debonding size to wavelength ratio (R_{DW}). The out-of-plane displacements are monitored at 36 points at $r = 50\text{mm}$ and $0^\circ \leq \theta \leq 360^\circ$ with intervals of 10° .

To investigate the measured signals in time-frequency domain, energy density spectra of the signals are obtained using short-time Fourier transform (STFT). Figures 5-6a and 5-6b show the energy density spectrum of the signal for the case with debonding size of 38mm at $\theta = 30^\circ$,

and 22mm at $\theta = 330^\circ$, respectively. Second and third harmonics of the Rayleigh wave are visible in the energy density spectra.

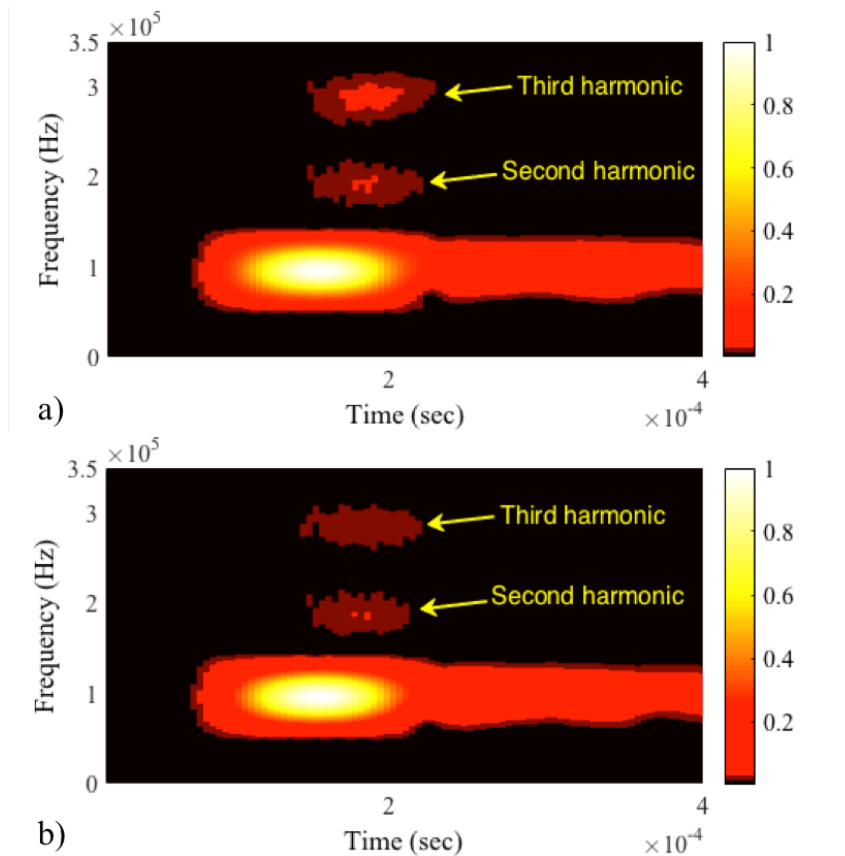


Figure 5-6. Energy density spectrum in time-frequency domain for a. debonding size of 38×38 mm and $\theta = 30^\circ$; and b. debonding size of 22×22 mm and $\theta = 330^\circ$

For each debonding case, the amplitudes of the fundamental harmonic (f_0), the second harmonic ($2f_0$) and the third harmonic ($3f_0$) are obtained from the energy density spectrum at the respective frequencies. The ratio of the second harmonic amplitude to the fundamental harmonic amplitude (A_2/A_1), and ratio of the third harmonic amplitude to the fundamental harmonic amplitude (A_3/A_1) are considered. These ratios for each debonding case are presented against θ in the form of directivity pattern. Figure 5-7 displays the directivity pattern of A_2/A_1 for the case of debonding size 38mm×38mm. The maximum value of the A_2/A_1 ratio is around

0.08, which occurs at $\theta = 0^\circ$. As shown in Figure 5-7, the scattering energy is mainly concentrated in the forward scattering direction. The directivity pattern of A_3/A_1 for the case of debonding size $22\text{mm} \times 22\text{mm}$ is shown in Figure 5-8. As shown in Figure 5-8, the energy in the forward scattering direction is larger than that in the backward scattering direction. The maximum value of the A_3/A_1 is around 0.03 and occurs at $\theta = 30^\circ$ and $\theta = 330^\circ$.

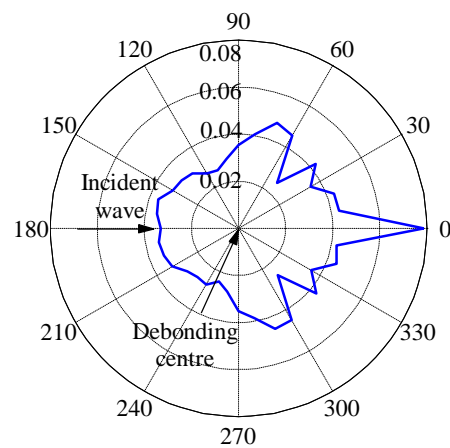


Figure 5-7. Directivity pattern for second harmonic amplitude to fundamental harmonic amplitude ratio (A_2/A_1) in the model with debonding size $38\text{mm} \times 38\text{mm}$

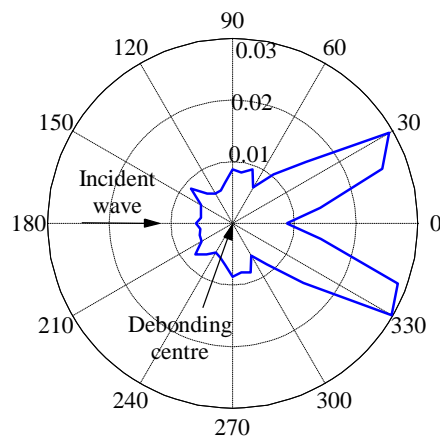


Figure 5-8. Directivity pattern for third harmonic amplitude to fundamental harmonic amplitude ratio (A_3/A_1) in the model with debonding size $22\text{mm} \times 22\text{mm}$

Figures 5-9 to 5-12 show the higher harmonic amplitudes of Rayleigh wave with respect to RDW at different directions. Figure 5-9 shows the A_2/A_1 ratio in the forward scattering direction as a function of R_{DW} . At $\theta = 0^\circ$, the A_2/A_1 ratio starts with a rapid rise and a then a sharp drop until $R_{DW}=1$. After that, it increases constantly to a peak of 0.0864 at $R_{DW} = 2$. At $\theta = 30^\circ$ and $\theta = 330^\circ$, the A_2/A_1 ratio first increases sharply to a peak of 0.0683 and then decreases steeply to 0.0343 at $R_{DW} = 1$. It then shows some fluctuations with a decreasing trend. The A_2/A_1 ratio at $\theta = 60^\circ$ and $\theta = 300^\circ$ drops slowly until $R_{DW} = 1$, and then exhibits moderate fluctuations. At $\theta = 90^\circ$ and $\theta = 270^\circ$, the A_2/A_1 ratio rises gradually to 0.0480 until $R_{DW} = 1$, it then falls to 0.0334 at $R_{DW} = 1.36$. After this point, it increases slowly to 0.0363 at $R_{DW} = 2$.

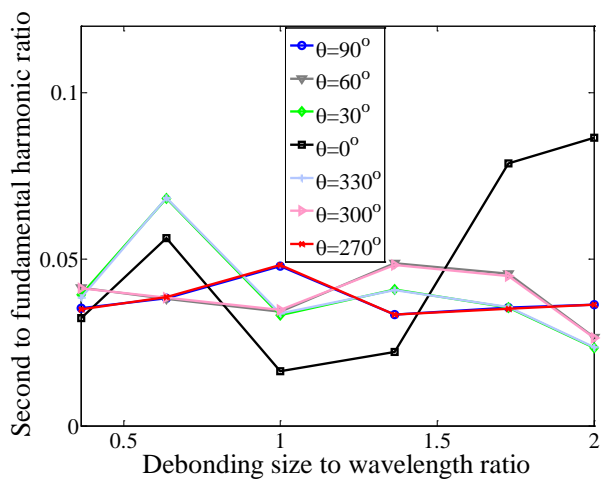


Figure 5-9. Second harmonic amplitude to fundamental harmonic amplitude ratio (A_2/A_1) in the forward scattering direction as a function of debonding size to wavelength ratio

Figure 5-10 shows the A_3/A_1 ratio in the forward scattering direction as a function of R_{DW} . At $\theta = 0^\circ$, the A_3/A_1 ratio begins with a sudden rise, next a sharp drop, and then a steep increase to a peak of 0.0420 at $R_{DW} = 1.36$. Then, it decreases slowly to 0.0375 at $R_{DW} = 2$. At $\theta = 30^\circ$ and $\theta = 330^\circ$, the A_3/A_1 ratio first increases rapidly to 0.0335 and then falls gradually to 0.0229 at $R_{DW} = 1.36$. Then, it increases steadily to a peak of 0.0416 at $R_{DW} = 1.73$. The A_3/A_1 ratio at

$\theta = 60^\circ$, $\theta = 300^\circ$, $\theta = 90^\circ$ and $\theta = 270^\circ$ is notably smaller than amplitude ratio at $\theta = 0^\circ$, $\theta = 30^\circ$ and $\theta = 330^\circ$ while exhibiting moderate fluctuations.

The A_2/A_1 ratio in the backward scattering direction as a function of R_{DW} is shown in Figure 5-11. The A_2/A_1 ratios at $\theta = 120^\circ$, $\theta = 240^\circ$, $\theta = 150^\circ$, $\theta = 210^\circ$ and $\theta = 180^\circ$ show slight fluctuations. As shown in Figure 5-11, the A_2/A_1 ratio at $\theta = 150^\circ$, $\theta = 210^\circ$ and $\theta = 180^\circ$ is slightly bigger than that at $\theta = 120^\circ$ and $\theta = 240^\circ$. Figure 5-12 displays the A_3/A_1 ratio in the backward scattering direction as a function of R_{DW} . At $\theta = 150^\circ$, $\theta = 210^\circ$ and $\theta = 180^\circ$, it is obvious that the A_3/A_1 ratio in the backward scattering direction is markedly smaller than that of A_2/A_1 ratio and it fluctuates around 0.006-0.009. However, at $\theta = 120^\circ$ and $\theta = 240^\circ$, the amplitude starts with small values and slight fluctuations until $R_{DW} = 1.36$. After that, it increases steadily to a peak of 0.0024, and then falls steeply to 0.0062 at $R_{DW} = 2$.

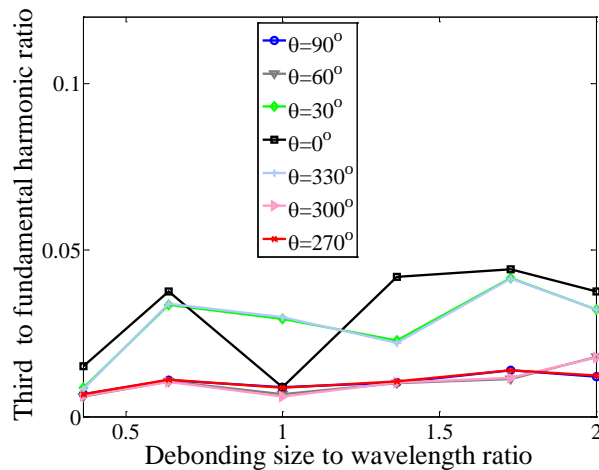


Figure 5-10. Third harmonic amplitude to fundamental harmonic amplitude ratio (A_3/A_1) in the forward scattering direction as a function of debonding size to wavelength ratio

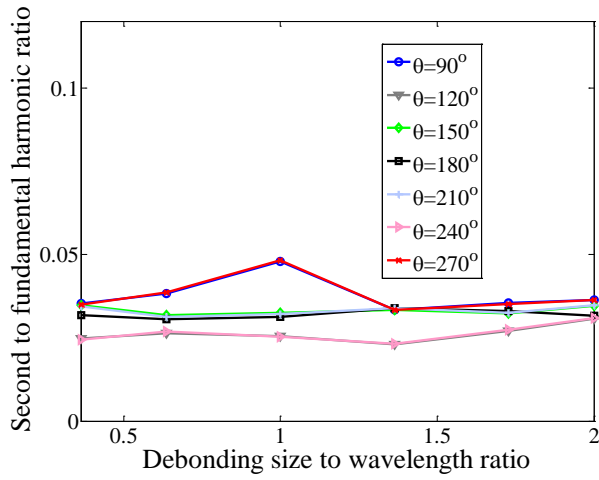


Figure 5-11. Second harmonic amplitude to fundamental harmonic amplitude ratio (A_2/A_1) in the backward scattering direction as a function of debonding size to wavelength ratio

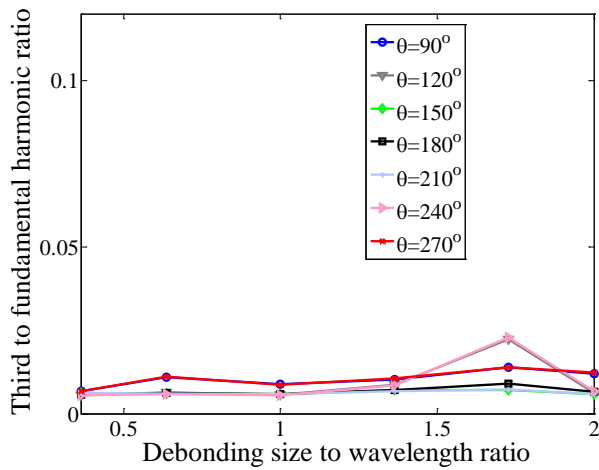


Figure 5-12. Third harmonic amplitude to fundamental harmonic amplitude ratio (A_3/A_1) in backward scattering direction as a function of debonding size to wavelength ratio

The overall trends of the second harmonic and third harmonic of the Rayleigh wave in the forward and backward scattering direction are discussed for the cases of rectangular debondings. For smaller values of R_{DW} , the A_2/A_1 ratio has larger values at $\theta = 30^\circ$ and $\theta = 330^\circ$ than $\theta = 0^\circ$. However, for $R_{DW} > 1.36$, the largest values of A_2/A_1 ratio are at $\theta = 0^\circ$. The maximum values of A_3/A_1 ratio in the forward scattering direction occur at $\theta = 0^\circ$, and then at $\theta = 30^\circ$ and $\theta = 330^\circ$. In general, the second and third harmonics in backward scattering

direction have smaller amplitudes than that in the forward scattering direction. Besides, it is obvious that the third harmonic in the backward scattering direction are smaller than that of second harmonic for cases of rectangular debondings.

6 Debonding localisation in FRP-retrofitted concrete based on scattering of linear Rayleigh wave

This chapter investigates the application of linear Rayleigh wave for detecting debonding in FRP-retrofitted concrete structures. A method based on Time-of-flight (ToF) is developed to locate debonding between the FRP and concrete. A 3D FE model is used to simulate the Rayleigh wave propagation and scattering at the debonding in the FRP-retrofitted concrete structure. A series of numerical case studies are carried out to demonstrate the capability of the proposed debonding detection method. Different debonding sizes and locations are considered in the case studies. It is demonstrated that the ToF-based method is capable of locating debonding at FRP/concrete interface.

6.1 Basics of debonding localisation method

ToF is an important feature of a guided wave signal in time domain. ToF-based damage localization has been widely used in guided wave damage detection [125-128]. Basically, ToF can be defined as the time difference between the incident wave and damage-scattered wave, actuated and captured by the same pair of actuator-sensor. Considering FRP-retrofitted concrete model with debonding between FRP and concrete, the simplest case is when debonding is located exactly on the projection of actuator and sensor connection. First, the sensor captures the incident wave. Then, wave propagates and reflects back from debonding, which is captured again by the sensor as shown in Figure 6-1. Difference of ToF of debonding-scattered wave and that of incident wave (Δt) and the group velocity of the wave (C_g) can be used to locate the debonding:

$$L = \frac{1}{2}(C_g \cdot \Delta t) \quad (32)$$

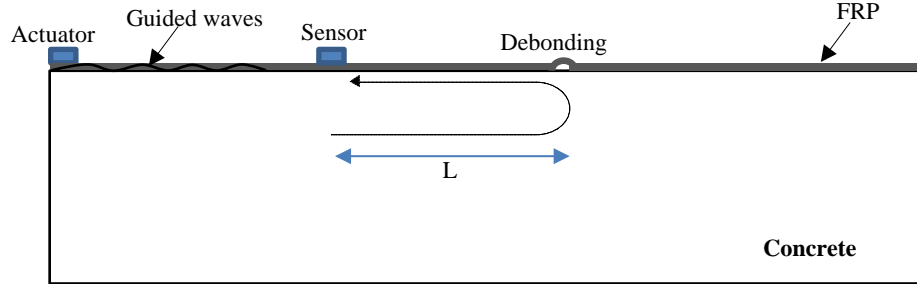


Figure 6-1. Schematic diagram of 1D damage localization in FRP-retrofitted concrete using ToF

Figure 6-2 illustrates an FRP-retrofitted concrete element with a pair of actuator-sensor attached on FRP composite. Actuator, sensor and debonding are assumed to be located at (x_A, z_A) , (x_S, z_S) and (x_D, z_D) respectively. Now, Equation 32 can be expanded as:

$$\begin{aligned} \Delta t &= t_{A-D-S} - t_{A-S} \\ &= \left(\frac{\sqrt{(x_D - x_A)^2 + (z_D - z_A)^2}}{C_g} + \frac{\sqrt{(x_D - x_S)^2 + (z_D - z_S)^2}}{C_g} \right) \\ &\quad - \frac{\sqrt{(x_S - x_A)^2 + (z_S - z_A)^2}}{C_g} \end{aligned} \quad (33)$$

where C_g is the group velocity. The solution to this equation is an ellipse, presented by dotted line, which indicates the potential locations of the damage.

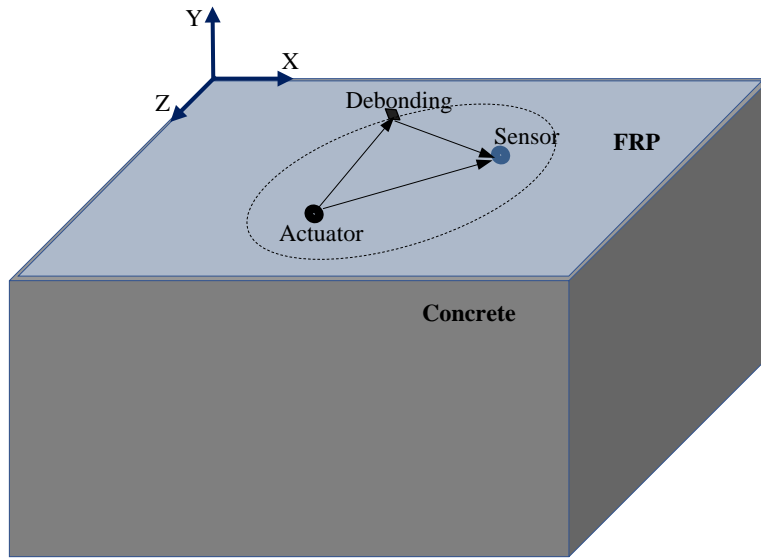


Figure 6-2. Schematic diagram of damage localization in FRP-retrofitted concrete element using a pair of actuator/sensor

In the real situation, where we have a network of transducers, each operating as both actuator and sensor, Equation 33 can be further expanded. With a network consisting of N transducers, this equation can be applied to each pair of transducers, transducer (i) and transducer (j), where $i, j = 1, 2, \dots, N$ and $i \neq j$. If Δt_{i-j} denotes difference between ToF of wave generated by actuator (i), scattered by damage and then captured by sensor (j), and ToF of wave generated by actuator (i) and captured directly by sensor (j), we can expand Equation 33 as [28]:

$$\Delta t_{i-j} = \left(\frac{\sqrt{(x_D - x_i)^2 + (z_D - z_i)^2}}{c_g} + \frac{\sqrt{(x_D - x_j)^2 + (z_D - z_j)^2}}{c_g} \right) - \frac{\sqrt{(x_i - x_j)^2 + (z_i - z_j)^2}}{c_g} \quad (34)$$

The solution of a set of above-mentioned equations will result in a number of elliptic shapes, the common intersections of which, can locate the damage.

6.2 Numerical model description

In the FE model in this chapter, S4R shell elements are used to model the FRP laminate and C3D8R solid elements are used to model the concrete. As discussed in Section 4.6.1, rebars in the concrete has minor effects on the measured Rayleigh wave and only cause body wave reflections, which could be removed by baseline subtraction. Effects of rebars on Rayleigh wave scattering from debonding are further discussed in Section 6.3. Therefore, the rebars are not modelled in the FE model in this chapter. In the literature, it is shown that limiting the excitation frequency up to 150 kHz could minimise the Rayleigh wave scattered from concrete aggregates [116]. Therefore, a 150 kHz narrow-band five-cycle sinusoidal tone burst pulse modulated by a Hanning window is used as the excitation signal in this section. The Rayleigh wave is generated by applying out-of-plane nodal displacement to the FE nodes covered by a 10mm diameter circular transducer area. The Rayleigh wave was measured by monitoring out-of-plane nodal displacements. Shell elements with dimension $1\text{mm} \times 1\text{mm}$ and solid elements with dimension $1\text{mm} \times 1\text{mm} \times 1\text{mm}$ are used in ABAQUS models. This ensures at least 12 FE nodes exist per wavelength, and hence, guarantees the accuracy of the FE simulations. The stable time increment is automatically controlled by ABAQUS as described in Section 3.1. To simulate the FRP-retrofitted concrete, surface-to-surface tie constraint is applied to connect nodes between the shell and solid elements. The debonding between FRP and concrete is simulated by untying nodes covered by the debonding area.

The Young's modulus and density of the concrete are assumed to be 25GPa and 2400kg/m^3 , respectively. The FRP composite is 4-ply with layup sequence of $[0/90]_s$. The thickness of each lamina is 0.2mm. The fibre weight fraction; W_f ; is assumed to be 0.8. Table 6-1 shows the mechanical properties of the carbon fibre and epoxy resin.

Table 6-1. Elastic properties of carbon fibre and epoxy resin

Elastic properties of carbon fibre					
E_{f11} (GPa)	E_{f22} (GPa)	G_{f12} (GPa)	G_{f23} (GPa)	ρ_f (kg/m ³)	ν_{f12}
231	14.48	22.75	4.83	1760	0.27
Elastic properties of epoxy matrix					
E_m (GPa)	G_m (GPa)	ρ_m (kg/m ³)	ν_m		
3.77	1.35	1220	0.40		

Chamis [129] formulated mechanical properties of a composite ply based on the properties of fibre and matrix as:

$$\rho = V_f \rho_f + V_m \rho_m \quad (35)$$

$$E_{11} = V_f E_{f11} + V_m E_m \quad (36)$$

$$E_{22} = E_{33} = \frac{E_m}{1 - \sqrt{V_f} \left(1 - \frac{E_m}{E_{f22}}\right)} \quad (37)$$

$$G_{12} = G_{13} = \frac{G_m}{1 - \sqrt{V_f} \left(1 - \frac{G_m}{G_{f12}}\right)} \quad (38)$$

$$G_{23} = \frac{G_m}{1 - \sqrt{V_f} \left(1 - \frac{G_m}{G_{f23}}\right)} \quad (39)$$

$$\nu_{12} = \nu_{13} = V_f \nu_{f12} + V_m \nu_m \quad (40)$$

$$\nu_{23} = \frac{E_{22}}{2G_{23}} - 1 \quad (41)$$

where V , W , E , G , ρ and ν represent the volume fraction, weight fraction, modulus of elasticity, shear modulus, density and Poisson's ratio of constituent materials, respectively. Also, the

subscripts f and m denote the properties of fibre and matrix. Based on the elastic properties of carbon fibre and epoxy matrix, and carbon fibre weight fraction, the elastic properties of each FRP lamina are shown in Table 6-2.

Table 6-2. Mechanical properties of each FRP ply

E_{11} (GPa)	E_{22} (GPa)	E_{33} (GPa)	G_{12} (GPa)	G_{13} (GPa)	G_{23} (GPa)	ν_{12}	ν_{13}	ν_{23}	ρ (kg/m ³)
170.78	10.30	10.30	6.97	6.97	3.53	0.30	0.30	0.46	1617

6.3 Numerical case studies

To validate the ToF-based damage localisation explained in Section 6.1, a series of numerical case studies are considered. In the numerical case studies, the dimensions of the 4-ply FRP are 250mm × 200mm, which is bonded to a 250mm × 200mm × 80mm (L×W×H) concrete. 40mm wide ALIDs are applied to the boundaries of FRP and concrete parts. ALID is consisted of 40 layers; each 1mm thick; which is equal to the element size. Considering Equation 28, P was set to 3 and α_{max} was 2.5×10^6 . The assembly of FRP/concrete model is shown in Figure 6-3.

Four cases are considered in the numerical case studies. Cases 1–3 consider a 6mm diameter circular debonding located at three different locations as shown in Figure 6-4. Based on the Cartesian coordinate shown in Fig. 46, the coordinates of the PZT and the centres of the debondings are summarised in Tables 6-3 and 6-4, respectively. Case 4 considers a debonding at the same location as Case 3 but the diameter of the debonding is increased to 8mm.

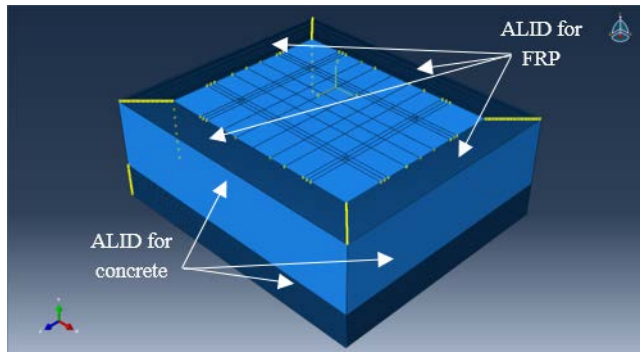


Figure 6-3. FE model of FRP-retrofitted concrete

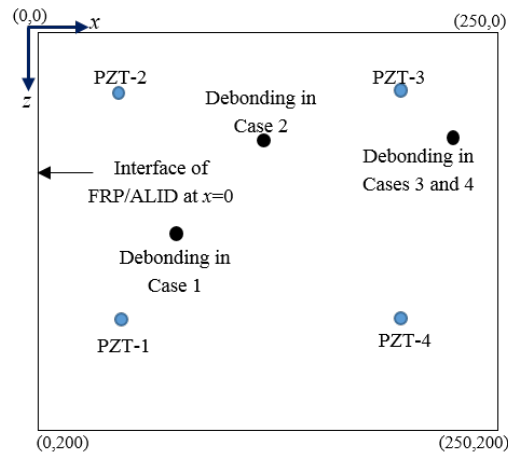


Figure 6-4. PZT and debonding locations in Cases 1-3 of the numerical studies

In each case, Rayleigh wave is sequentially generated by each PZT, and at the same time the wave signals are measured by the rest of the PZTs. A model without the debonding is used for baseline subtracting purpose to extract the scattered wave signal. The scattered wave is obtained by subtracting the simulated displacement responses of the model with debonding from those of the intact model. Rayleigh wave signals are normalised based on the maximum absolute amplitude of signal in the model without debonding. Figure 6-5a shows the incident wave generated by PZT-1 and captured at PZT-3 in the model without debonding in Case 4. Figure 6-5b presents wave generated by PZT-1, scattered at the debonding and then captured by PZT-3. The scattered signal is shown in Figure 6-5c.

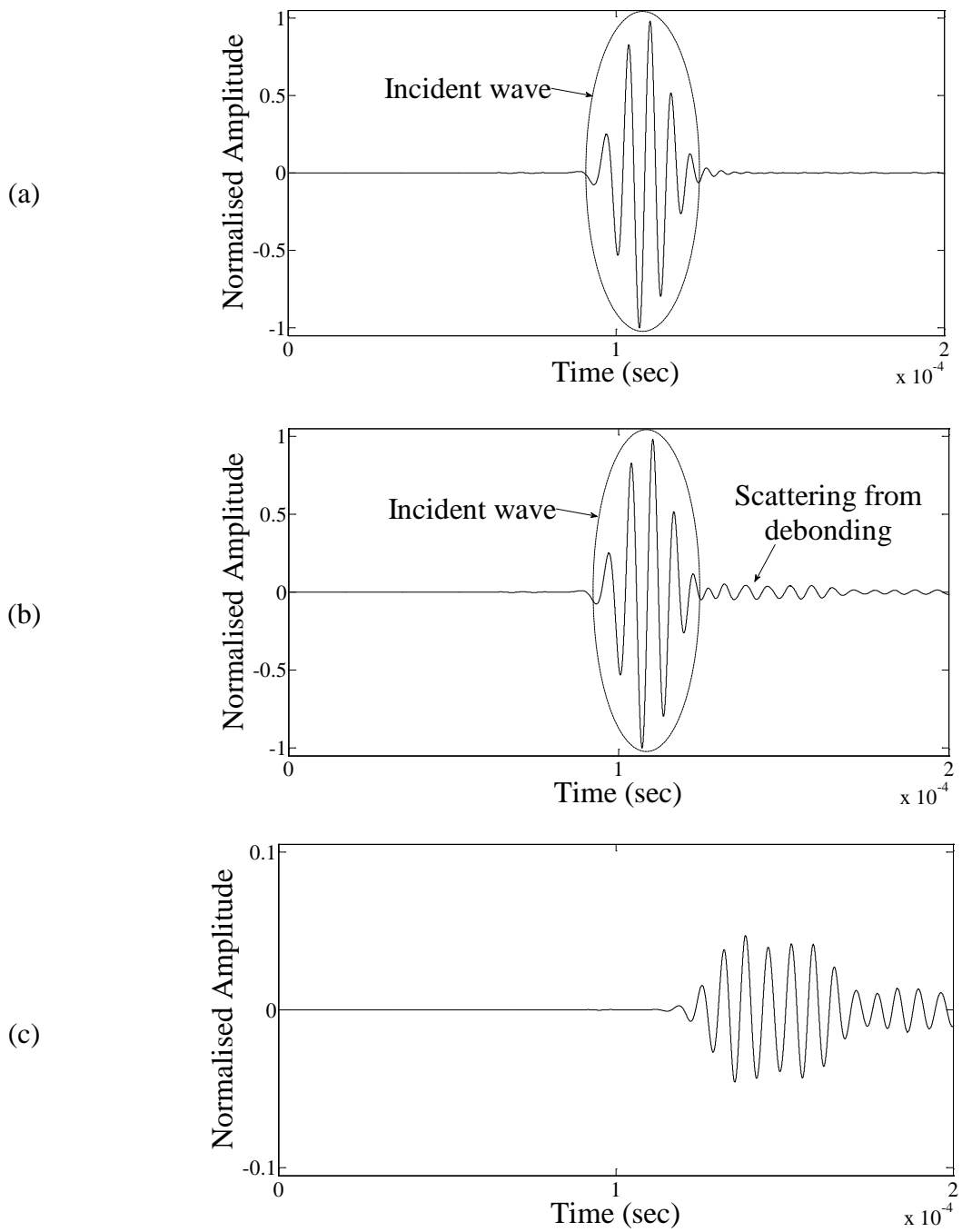


Figure 6-5. Wave signals generated by PZT-1 and captured by PZT-3 in the model without rebars a. signal from model without debonding; b. signal from model with debonding; and c. scattered signal obtained from baseline subtraction

As discussed in Section 4.6.1, rebars have minor effects on incident Rayleigh waves and rebar reflections can be removed by the baseline subtraction. To demonstrate the effect of rebar in wave propagation, 10mm diameter steel bars with a concrete cover of 50mm are added to the FE model. Figure 6-6a displays the incident wave generated by PZT-1 and captured at PZT-3 in the model with rebar and without debonding between FRP and concrete. Figure 6-6b shows the wave signal generated by PZT-1, scattered at the debonding and then captured by PZT-3. The scattered signal from debonding in the model with rebars is shown in Figure 6-6c. As demonstrated in Figures 6-5c and 6-6c, the scattered signal is the same for both models, i.e. without and with rebars.

Table 6-3. Coordinates of the PZT centres in numerical case studies

PZT	x (mm)	z (mm)
1	50	150
2	50	50
3	200	50
4	200	150

Table 6-4. Coordinates of the debonding centres and diameters in numerical case studies

Case	x (mm)	z (mm)	Debonding diameter (mm)
1	80	120	6
2	125	80	6
3	225	80	6
4	225	80	8

It should be noted that experimentally measured Rayleigh wave signals contain some degrees of noise. The quality of signals can be improved significantly by averaging and also applying a bandpass filter. Thus, for all numerical case studies of damage localisation, 2% of noise was added to the signals obtained from FE simulations. That could ensure that the proposed method can be used in practical situations. Figure 6-7 shows the signal generated by PZT-4 and captured by PZT-3 for debonding Case 4 with the added noise.

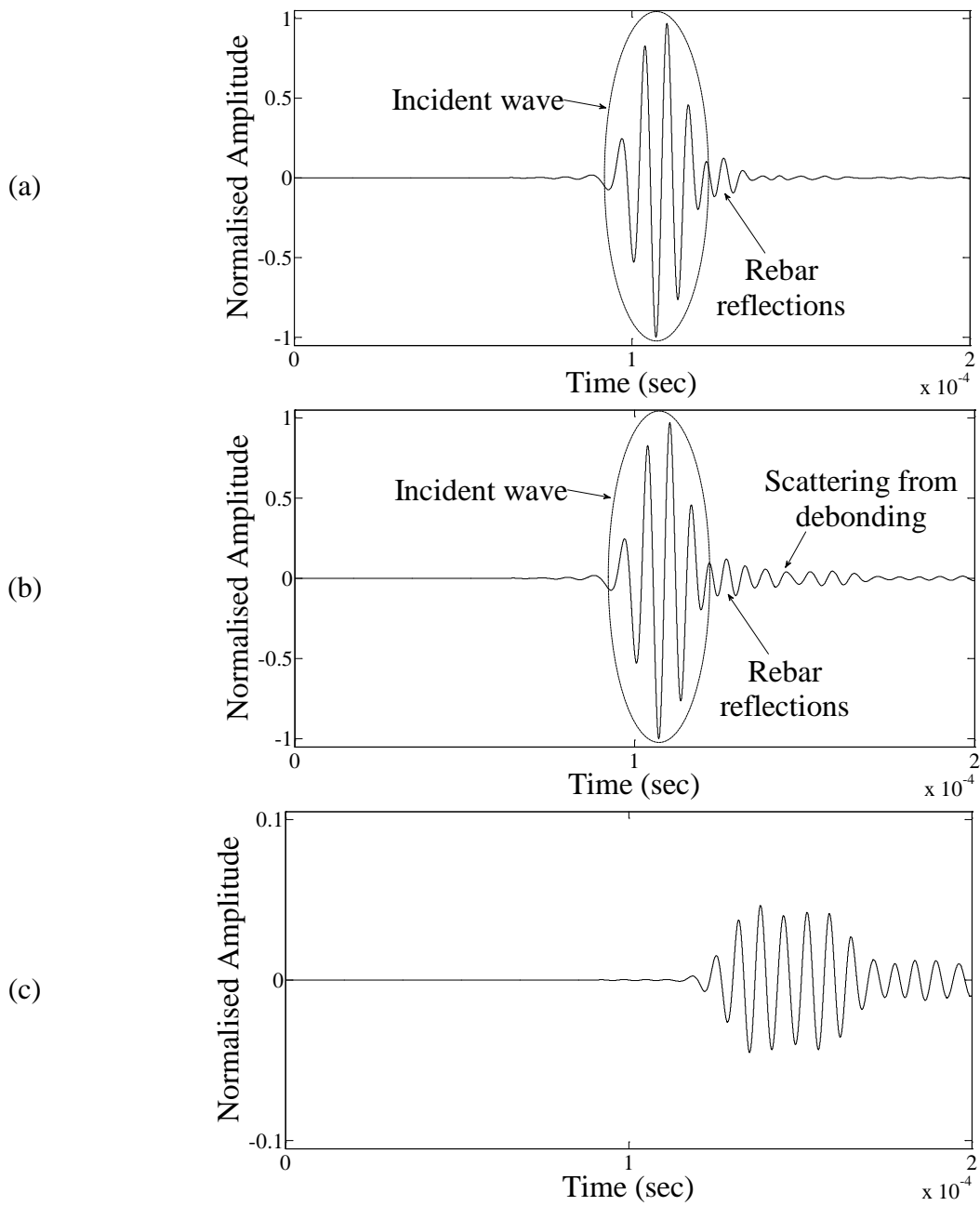


Figure 6-6. Wave signals generated by PZT-1 and captured by PZT-3 in the model with rebars a. signal from model without debonding; b. signal from model with debonding; and c. scattered signal obtained from baseline subtraction

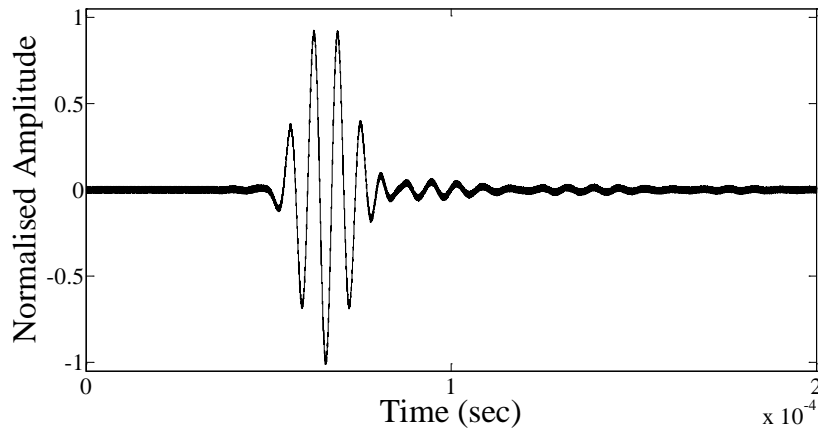
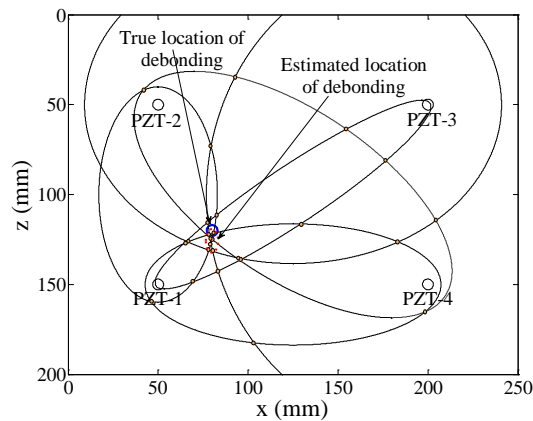


Figure 6-7. Wave signals generated by PZT-4 and captured by PZT-3 for debonding Case 4

The ToF is calculated based on the difference of arrival time of incident wave and the scattered wave from the debonding. Elliptic solutions of Cases 1–3 are obtained based on Equation 36 for each debonding location and are shown in Figures 6-8a to 6-8c, respectively. The intersection of each pair of ellipses is indicated by a solid circle. The area with the highest concentration of circles, as indicated by an ellipse with red dotted line, is the most probable location of the debonding. The true debonding location and size are indicated by circles with solid blue line.

(a)



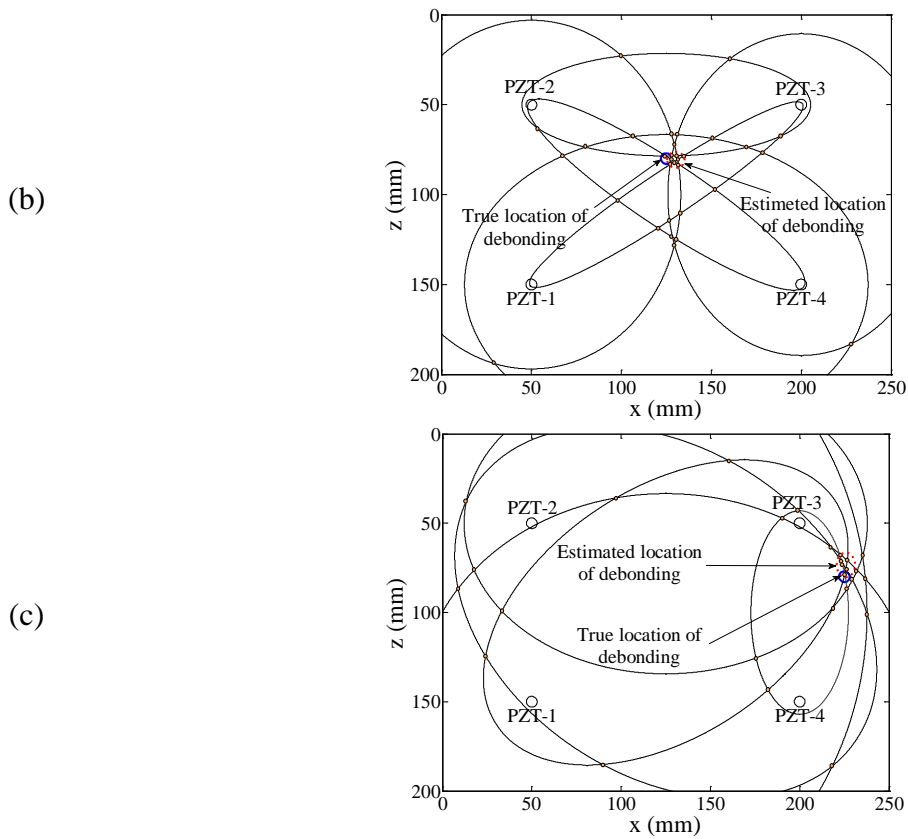


Figure 6-8. Elliptic solutions for 6mm diameter circular debonding in a. Case 1; b. Case 2; and c. Case 3

To validate the proposed ToF-based damage localisation method for larger size of debonding, Case 4 considers an 8mm diameter circular debonding located at the same location as the debonding in Case 3. The elliptic solution for this case is shown in Figure 6-9.

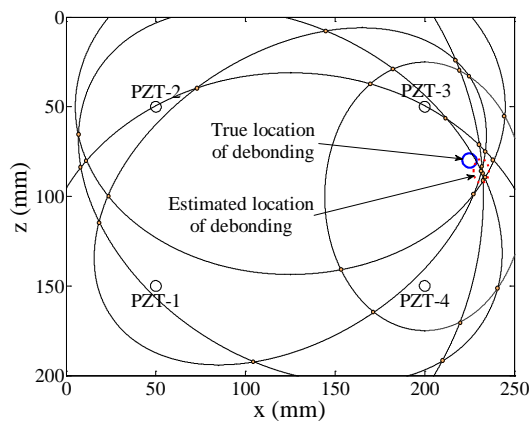


Figure 6-9. Elliptic solutions for 8mm diameter circular debonding in Case 4

As shown in Figures 6-8 and 6-9, the ToF-based damage localisation method is successfully applied to detect debonding at FRP/concrete interface.

7 Locating debonding in FRP-retrofitted concrete using nonlinear

Rayleigh wave

This chapter presents the application of nonlinear Rayleigh wave to detect debonding in CFRP-retrofitted concrete structures. The proposed method requires a network of transducers that are used to sequentially scan the CFRP-retrofitted reinforced concrete structures by transmitting and receiving Rayleigh wave. The second harmonic of Rayleigh wave due to contact nonlinearity at debonding between CFRP and concrete is used to detect debonding. A damage image reconstruction algorithm is proposed to provide a graphical representation for detecting and locating the debonding in the CFRP-retrofitted reinforced concrete structures. In this chapter, experimental case studies are used to demonstrate the performance of the proposed damage detection technique. A transducer array using four piezoelectric transducers to actuate Rayleigh wave and measure the second harmonic wave in the experiments. The results show that the proposed debonding detection technique is reliable in detecting and locating the debonding in the CFRP-retrofitted reinforced concrete structures.

7.1 Debonding detection method using nonlinear Rayleigh wave

The proposed damage detection method determines the existence and location of the debonding based on second harmonic Rayleigh wave. A transducer array with N transducers is required to sequentially scan the targeted structures using Rayleigh wave. Each of the transducer can be used as both actuator and sensor to excite and measure the wave signals, respectively. In the sequential scan, one of the transducers is used to generate the Rayleigh wave in the CFRP-

retrofitted reinforced concrete structure, the rest of the transducers are used to measure the wave signals. This provides a total of $N(N-1)$ actuator/sensor signal paths.

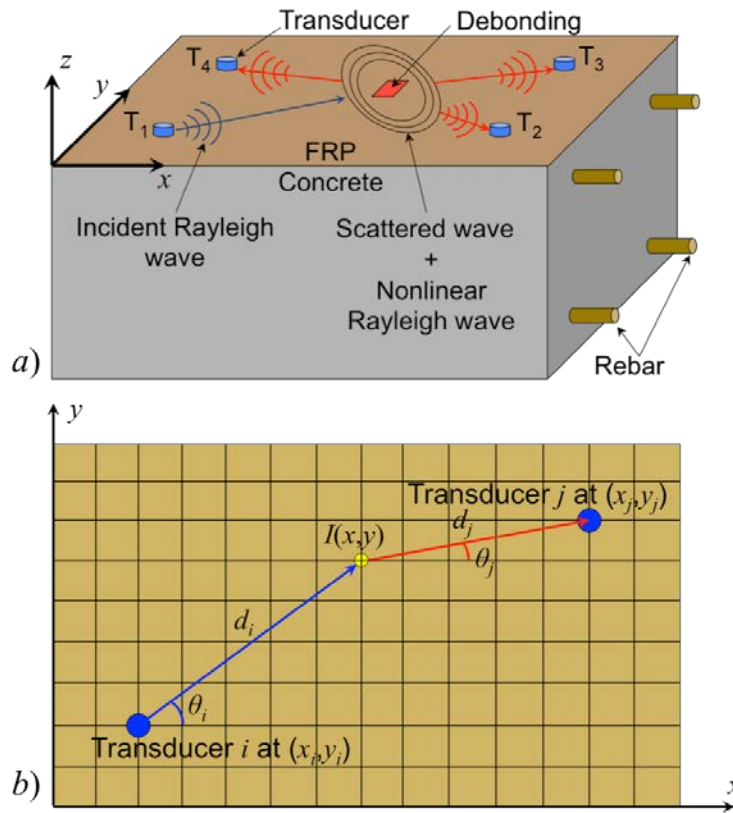


Figure 7-1. a. Rayleigh wave propagation and scattering at debonding between CFRP and concrete interface; and b. discretization of inspection area by image pixels

Figure 7-1a shows a transducer array with four transducers, $T1$, $T2$, $T3$ and $T4$, which is used as an example to illustrate the proposed debonding detection method. In the sequential scan, the transducer $T1$ is first used as the actuator to excite the Rayleigh wave, while the transducers $T2$, $T3$ and $T4$ are used as the sensor to measure the wave signals. The incident Rayleigh wave propagates and reaches the debonding. When the incident Rayleigh wave interacts with the debonding, wave scattering occurs and the second harmonic of Rayleigh wave is also generated due to the contact nonlinearity at the debonding. Therefore, the signals measured by the transducers include the incident Rayleigh wave, the scattered waves from the debonding, which

contain components at fundamental and second harmonic frequency, and also the wave reflected from the boundaries of the structure. This process is repeated $N-1$ times with transducer $T2$, $T3$ and $T4$ being used as the actuator, respectively. Once the sequential scan process is completed, the measured signals are post-processed to determine the debonding location using the proposed damage detection method.

The idea of the proposed damage detection method is to discretise the inspection area into image pixels as shown in Figure 7-1b. Without loss of generality, transducers i and j are used as an example to illustrate the damage detection algorithm. When Rayleigh wave interacts with the debonding, the second harmonic of Rayleigh wave is generated. Therefore, it is assumed that the wave propagation can be separated into two stages. In the first stage, the Rayleigh wave is generated from the transducer i at (x_i, y_i) and then propagate to the image pixel at (x, y) . In the second stage, it is assumed that the image pixel is considered as the potential debonding location, and hence, the second stage considers the second harmonic of Rayleigh wave is generated at the debonding location (the image pixel being considered) and propagates to the transducer j at (x_j, y_j) . Since the locations of the transducers and image pixels are known in advance before carrying out the damage inspection, the group velocity of Rayleigh wave at fundamental and second harmonic frequency can be obtained theoretically or measured experimentally. The arrival time of the second harmonic Rayleigh wave can be calculated by:

$$T_{ij}(x, y) = \frac{\sqrt{(y - y_i)^2 + (x - x_i)^2}}{c_{g,f}(\theta_i)} + \frac{\sqrt{(y_j - y)^2 + (x_j - x)^2}}{c_{g,2f}(\theta_j)} \quad (42)$$

where $C_{g,f}$ and $C_{g,2f}$ are the group velocity of the Rayleigh wave at fundamental and second harmonic frequency, respectively. θ_i and θ_j are the Rayleigh wave propagation direction from

transducer i to the image pixel and from the image pixel to the transducer j . The first and second term at the right-hand side of the Equation 42 is the arrival time of the fundamental frequency of Rayleigh wave from the transducer i to the image pixel (x,y) , and the second harmonic of Rayleigh wave from the image pixel (x,y) to the transducer j , respectively.

Since the measured wave signal at transducer j contains both fundamental and second harmonic of Rayleigh wave, a short-time Fourier transform (STFT) is used to extract the second harmonic of Rayleigh wave and it is defined in Equation 20.

In the proposed method, a cross-correlation analysis between the incident pulse at fundamental frequency input to transducer i and second harmonic of Rayleigh wave measured at transducer j is used to determine the time shift for describing the source location of the second harmonic of Rayleigh wave. As the second harmonic is induced due to the contact nonlinearity at debonding, it can be used to determine the debonding location. Figure 7-2 shows a schematic diagram of the incident wave and the measured nonlinear Rayleigh wave in the proposed debonding detection technique. The incident Rayleigh wave only contains components excited fundamental frequency. The incident Rayleigh wave propagates and interacts with the debonding. The second harmonic Rayleigh wave is then induced due to the contact nonlinearity at the debonding. Therefore, the measured signal by the transducer contains components at both excited fundamental frequency and second harmonic frequency as shown in Figure 7-2. With the information of the incident wave components at the excited fundamental frequency and damage information at the second harmonic frequency, the cross-correlation C_{ij} is defined as:

$$C_{ij}(t) = \int_0^T S_F(\tau, f_c) S_{ij}(\tau + t, 2f_c) d\tau \quad (43)$$

where S_F is the STFT transformed incident pulse. S_{ij} is the STFT transformed signal measured by transducer j while transducer i is used as actuator. f_c and $2f_c$ is the central frequency of the excitation signal and the corresponding second harmonic frequency, respectively.

In the sequential scan, there are $N(N-1)$ actuator/sensor paths. For each actuator/sensor path, the magnitude of a set of image pixels in the inspection area can be calculated and the magnitude of the cross-correlation at the possible damage location has the largest value. To determine the debonding location, the image indicating the possible debonding location can be obtained by superimposing the power flux of all actuator/sensor path images as [130]

$$I(x, y) = \sum_{i=1}^N \sum_{j \neq i}^N \kappa_{ij} C_{ij} [T_{ij}(x, y)]^2 \quad (44)$$

where κ_{ij} is the weighting factor used to take into account the varying sensitivity of each actuator/sensor path image. In this section, it is assumed to be uniform aperture weighting, i.e. equals to unity.

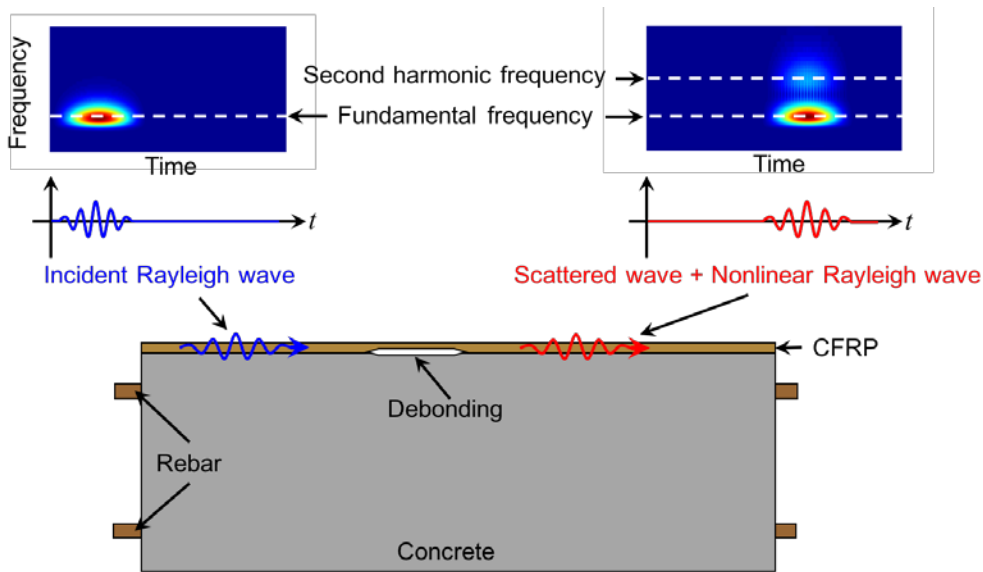


Figure 7-2. Schematic diagram of the proposed damage debonding method and signal processing

7.2 Experimental studies

7.2.1 Experiment equipment setup

Concrete specimens 3 and 4 with debonding at FRP/concrete interface were used for experimental measurements. Four 2mm thick and 10mm diameter circular PZT transducers (Ferroperm Pz27) were used to actuate and sense Rayleigh wave on each specimen. The transducers were bonded to the surface of the CFRP and they are located at $T1$ ($x_1 = 160\text{mm}$, $y_1 = 70\text{mm}$), $T2$ ($x_2 = 360\text{mm}$, $y_2 = 70\text{mm}$), $T3$ ($x_3 = 360\text{mm}$, $y_3 = 220\text{mm}$), and $T4$ ($x_4 = 160\text{mm}$, $y_4 = 220\text{mm}$). The excitation signal is a 95kHz, 15-cycle sinusoidal tone burst modulated by a Hanning window. Case 1 considers the concrete specimen 3 which has a 60mm×60mm debonding between the CFRP and concrete interface. In Case 2, the concrete specimen 4 with a 40mm×300mm debonding was used as shown in Figure 7-3.

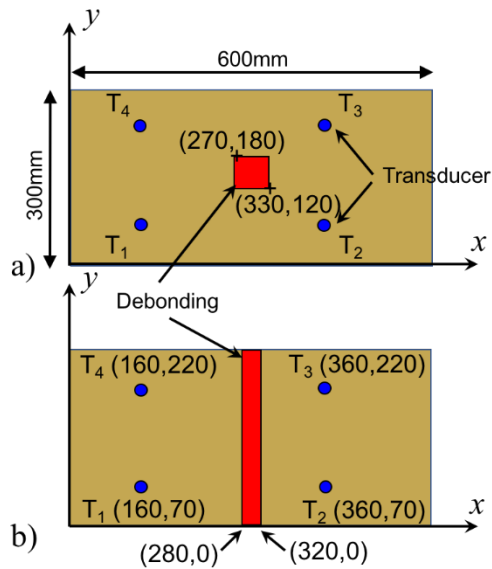


Figure 7-3. Schematic diagram of the CFRP-retrofitted concrete block and the layout of the surface-mounted transducer array (top view) a. concrete specimen 3 with 60mm×60mm debonding; and b. concrete specimen 4 with 40mm×300mm debonding

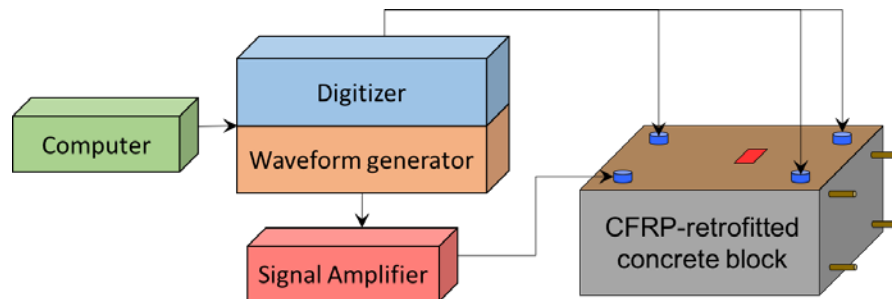


Figure 7-4. Experiment setup for one of the scanning processes in the sequential scan

Figure 7-4 shows the experimental setup used in this study. A PC-controlled NI PXI-5412 waveform generator was used to generate the excitation signal. The amplitude of the generated signal was then amplified by five times to 50V (peak-to-peak) using a KROHN-HITE 7500 amplifier. The Rayleigh wave signals measured by the PZT transducers and were recorded by NI PXI-5105 digitizer and the data was then sent to computer for analysis. The sampling

frequency was set to 10.24 MHz and the signals were averaged 5000 times to improve the signal-to-noise ratio.

7.2.2 Results and discussion

Figure 7-5 shows the data measured from signal path T_1 - T_4 for the specimen in Case 1, in which the transducer T_1 is used as actuator to excite Rayleigh wave while the transducer T_4 is used as sensor to measure the scattered wave signals. It is used as an example to illustrate and explain the wave packages in the measured signal. As mentioned in Section 7.1, the specimen has a 60mm×60mm debonding. As shown in Figure 7-5, the signal contains a number of wave packages. The first wave package is the incident wave, which propagates directly from the transducer T_1 to T_4 . The second wave package is the scattered wave from the debonding. As shown in Figure 7-3a, signal path from the transducer T_1 to the debonding, and then transducer T_4 is longer than the direct signal path from the transducer T_1 to T_4 . Therefore, the scattered wave arrives after the incident wave. The last wave package is the waves reflected from the boundaries and they are overlapped together as shown in Figure 7-5.

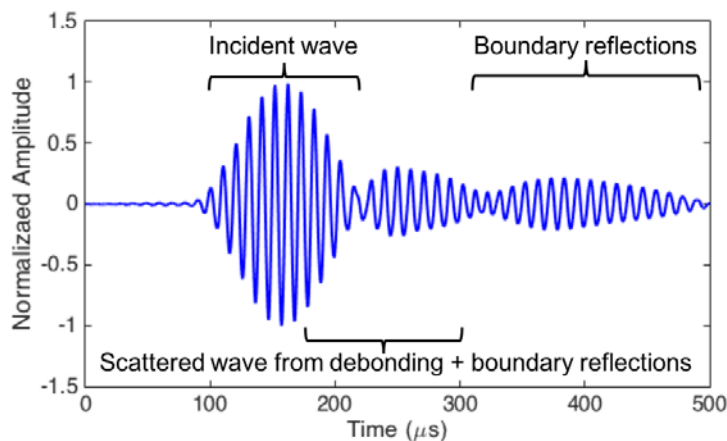


Figure 7-5. Measured data of signal path T_1 - T_4 with debonding size 60mm × 60mm

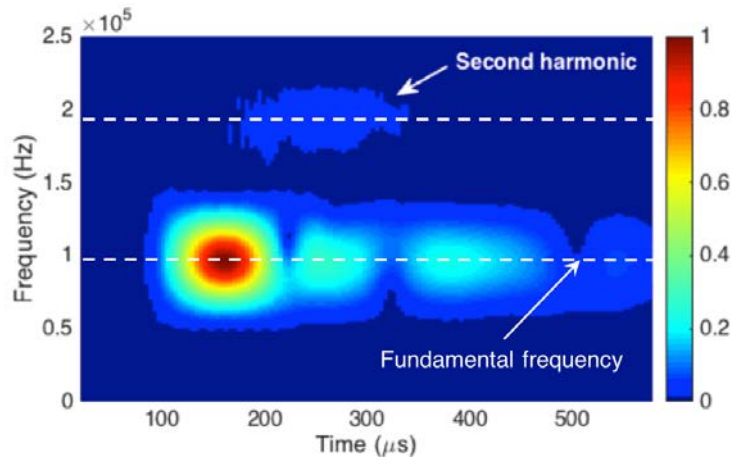


Figure 7-6. Energy density spectrum in time-frequency domain for the data of signal path T1-T4 with debonding size 60mm × 60mm

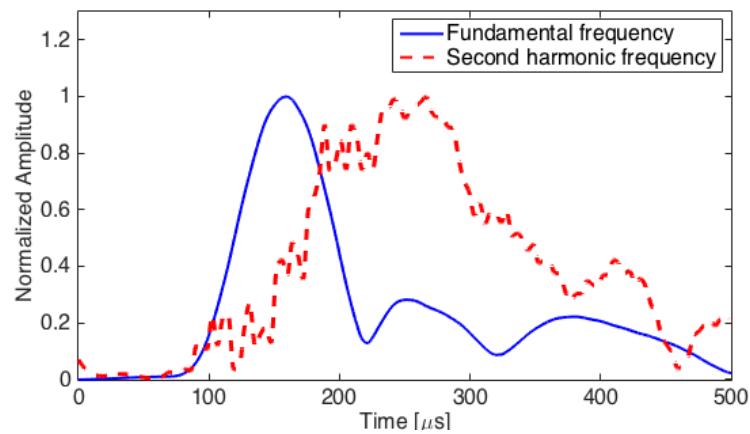


Figure 7-7. Normalised spectral amplitude of signal path T1-T4 at fundamental frequency and second harmonic frequency for debonding size 60mm × 60mm

As shown in Figure 7-5, the scattered wave package is partially mixed with the incident wave and boundary reflections. For damage detection technique based on the linear feature, it is essential to extract the scattered wave signal for damage detection using baseline data. Different to the linear feature, the second harmonic Rayleigh wave can be extracted using the time-frequency analysis without the baseline data. Figure 7-6 shows the corresponding time-frequency energy spectrum of the signal transformed using the STFT described in Section 7.1.

The figure shows that the time-frequency spectrum contains not only the signal components at the excited fundamental frequency (95kHz), but also the second harmonic frequency (190kHz).

Figure 7-7 also shows the corresponding normalised spectral amplitude at the excited fundamental frequency and second harmonic frequency. The second harmonic wave is generated due to the contact nonlinearity at the debonding. When the incident wave reaches and interacts with the debonding, the second harmonic wave is generated due to the contact nonlinearity. The second harmonic wave propagates and is then measured by the transducer T_4 . The results show that the arrival time is consistent with the scattered wave from the debonding. Since the second harmonic wave exists at the second harmonic frequency, it does not require the baseline data to extract the damage information.

As the specimen is the CFRP-retrofitted reinforced concrete structure, in which the CFRP is anisotropic material while the concrete can be considered as isotropic material, the group velocity is different in each propagation direction. Figure 7-8 shows the angular dependence of the measured group velocity for Rayleigh wave propagation in different directions on the CFRP-retrofitted reinforced concrete structure. The measured group velocity is used in the proposed damage detection technique to detect and locate the debonding.

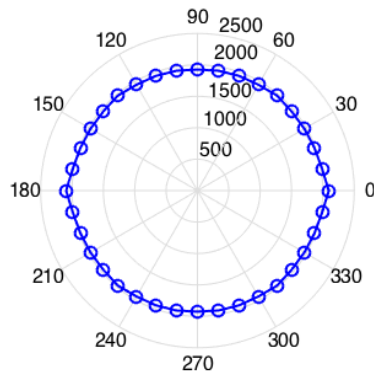


Figure 7-8. Angular dependence of group velocity in m/s for the CFRP-retrofitted concrete

Once the sequential scan process is completed, the measured signals are then processed using the STFT to extract the spectral amplitude at the second harmonic frequency. Using the data obtained at from signal path T_1 - T_4 as an example, it is $S_{14}(t, 190\text{kHz})$. With this information and the spectral amplitude of the incident wave at the excited fundamental frequency $S_F(t, 95\text{kHz})$, an actuator/sensor path image for T_1 - T_4 is obtained and shown in Figure 7-9. The image indicates the feasible debonding location based on the data measured by signal path T_1 - T_4 . The white dashed lines in the figure indicate the actual debonding location, size and shape.

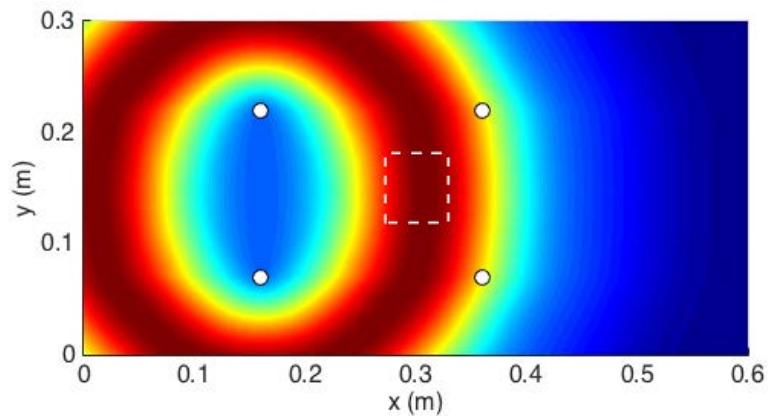


Figure 7-9. Typical image of actuator/sensor signal paths T1-T4 for debonding size 60mm × 60mm

Using Equation 44, the reconstructed image for indicating the debonding location can be obtained by superimposing all the actuator/sensor path images. Figure 7-10a shows the reconstructed image for Case 1. Figure 7-10b shows a binary image created from Figure 7-10a

by only accounting for image pixels whose intensity is larger than an arbitrary threshold value. In this chapter, it is chosen to be 95% of the maximum intensity of the reconstructed image. In this section, the predicted damage location is the centroid of the binary image, which is determined as the ratio of the first- and zeroth-order spatial moments of the binary image [131]. The predicted damage location for Case 1 is at $x = 0.3213\text{m}$ and $z = 0.1710\text{m}$ and it is indicated by a cross marker in Figure 7-10b.

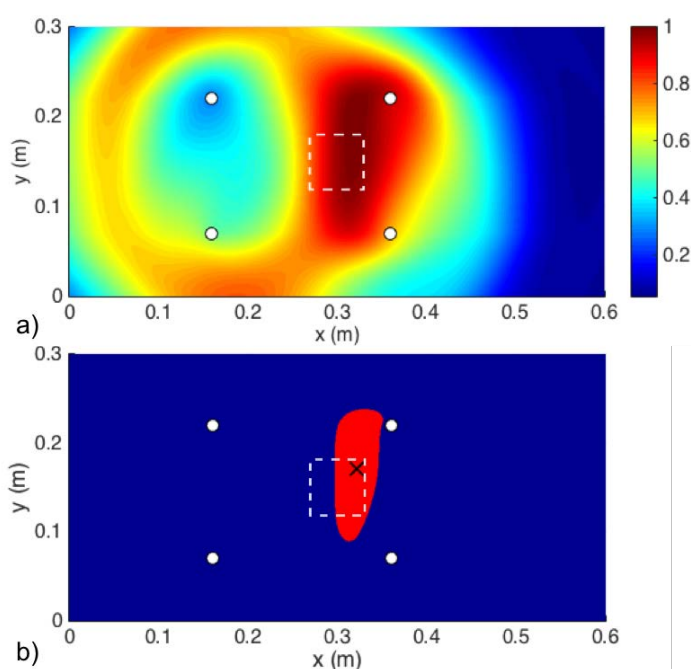


Figure 7-10. a. Debonding location image; and b. corresponding binary image for debonding size 60mm \times 60mm (Circles: PZT transducers, dashed line: actual debonding location and size, cross: centroid of the binary image)

Different to Case 1, Case 2 considers a debonding, which is across the whole width of the concrete block. The reconstructed image for Case 2 is shown in Figure 7-11a and the corresponding binary image is shown in Figure 7-11b. The same as Case 1, dashed lines are used to indicate the actual debonding location, size and shape. The predicted damage location

for Case 2 is at $x = 0.3188\text{m}$ and $y = 0.1413\text{m}$, and it is indicated by a cross marker in Figure 7-11b.

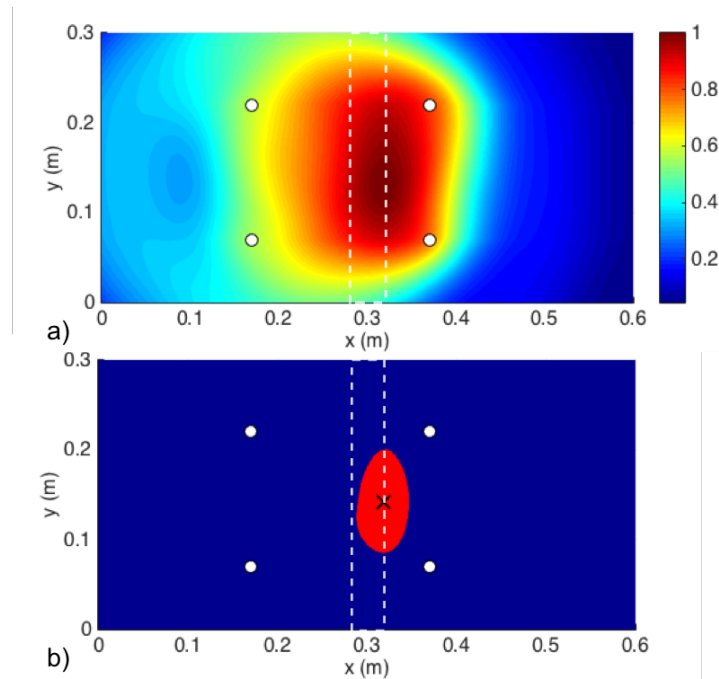


Figure 7-11. a. Debonding location image; and b. corresponding binary image for debonding size $40\text{mm} \times 300\text{mm}$ (Circles: PZT transducers, dashed line: actual debonding location and size)

Overall, the predicted debonding locations for Cases 1 and 2 are within the actual debonding region. The results demonstrate that the proposed damage detection technique is able to provide a reliable prediction of the debonding location in the CFRP-retrofitted reinforced concrete structures.

8 Conclusions and suggestions for future research

8.1 Conclusions

This thesis has presented a comprehensive study on the applications of Rayleigh wave for SHM in FRP-retrofitted concrete structures. The 3D FE model has been developed to simulate Rayleigh wave propagation in FRP-retrofitted concrete structures and scattering of signals at debonding at FRP/concrete interface. The numerical results of group and phase velocity, and of mode shapes of Rayleigh wave, have been verified by analytical solutions. The analytical solution is based on the global matrix method. To experimentally validate the numerical results of Rayleigh wave propagation and scattering, FRP-retrofitted concrete specimens have been prepared. As discussed in Chapter 4, experimental measurements have been carried out on test specimens to validate numerical results of Rayleigh wave propagation in FRP-retrofitted concrete structures. Very good agreement has been observed between numerical and experimental results. Furthermore, the numerical results of the Rayleigh wave scattering at the bonded mass have been verified by experimental measurements. By analytical and experimental validation of the numerical results, it has been shown that the 3D FE model can accurately simulate the propagation and scattering of Rayleigh wave in FRP-retrofitted concrete structures.

The scattering directivity patterns of linear Rayleigh wave at debonding at FRP/concrete interface have also been investigated in Chapter 4. Absorbing layers by increasing damping have been developed and applied to the numerical model in order to improve computational efficiency of scattering analyses. Different sizes and shapes of debonding have been considered for linear scattering studies. Scattering results have been presented in terms of R_{DW} which is

defined as debonding size/diameter to the wavelength ratio. For small values of R_{DW} , magnitudes of forward and backward scattering are close. For larger values of R_{DW} , the forward scattering is more sensitive to debonding than backward scattering, demonstrating larger magnitudes and a less complicated directivity pattern. It has been shown that the forward scattering for rectangular and circular debonding follows a similar trend while rectangular debonding demonstrates slightly larger magnitudes. Rectangular debondings cause larger backward scattering than do circular debondings; however, the trend of backward scattering is complex for both debonding shapes.

Nonlinear Rayleigh wave and higher harmonics generation of Rayleigh wave at the debondings in FRP-retrofitted concrete structures, have been investigated in Chapter 5. The numerical results of Rayleigh wave propagation and scattering have been presented in time, frequency and time-frequency domains. Both second and third harmonics of Rayleigh wave, induced by the debonding at FRP and concrete interface, have been studied in detail. Very good agreement has been observed between numerically calculated and experimentally measured results. It has been shown that the 3D FE model is capable of simulating nonlinear Rayleigh wave and higher harmonic generation at the debondings. The experimentally validated 3D FE model has been used in the parametric case studies.

To investigate scattering directivity of nonlinear Rayleigh wave, different sizes of debonding have been considered in Chapter 5. Second and third harmonics in the forward and backward scattering directions have been studied. The second and third harmonic amplitudes have been presented in terms of R_{DW} . For rectangular debondings, the amplitude of the second harmonic is generally larger than that of the third harmonic. Also, the second and third harmonic

amplitudes in the forward scattering direction are larger than that in the backward scattering direction. That means that the second and third harmonic energy is mainly concentrated in forward scattering direction.

Scattering of linear Rayleigh wave has been used to locate debonding in FRP-retrofitted concrete structures in Chapter 6. The proposed method is based on ToF of the incident wave generated by actuator and directly captured by a sensor, and ToF of the wave scattered by debonding at FRP/concrete interface. The 3D FE model has been used to simulate Rayleigh wave propagation and scattering. Numerical case studies have been presented for different locations and sizes of debonding. It has been demonstrated that the proposed ToF-based method can accurately locate debonding at FRP/concrete interface in FRP-retrofitted concrete structures.

A reference-free debonding detection technique for FRP-retrofitted concrete structures has been presented in Chapter 7. The technique is based on nonlinear Rayleigh wave and second harmonic generated due to contact nonlinearity at the debonding. In this chapter, the proposed debonding detection technique has been verified using experimental results. The results show that the reconstructed binary damage image is able to accurately predict the debonding location. One of the advantages of the proposed debonding detection technique is that it only requires a few transducers to locate the debonding within a reasonable size of inspection area. The proposed technique only involves computationally efficient algorithms, such as signal processing using STFT, and simple cross-correlation analyses. The technique can be practically implemented using a multiplexed data acquisition system, which allows sequential excitation of Rayleigh wave at each transducer and simultaneous measurement of signals from different

transducers. Therefore, the proposed imaging technique has the potential to achieve real-time in-situ debonding detection.

Overall, this PhD research has provided physical insights into propagation of Rayleigh wave in FRP-retrofitted concrete structures and scattering of signals at debondings at FRP/concrete interface. It has been demonstrated that Rayleigh wave signals are sensitive to debonding between FRP and concrete; therefore, scattering characteristics of Rayleigh wave can be used to identify the debonding. The introduced ToF-based method proves accurate to locate the debonding using scattering of linear Rayleigh wave. Besides, the proposed reference-free damage localisation technique can facilitate practical applications of nonlinear Rayleigh wave for SHM in FRP-retrofitted concrete structures.

8.2 Suggestions for further research

The current PhD thesis has thoroughly investigated the applications of Rayleigh wave in FRP-retrofitted concrete structures. The following topics are suggested for further research:

- The current research has explored applications of linear and nonlinear Rayleigh waves in FRP-retrofitted concrete structures to detect and locate debonding at FRP/concrete interface. However, debonding size should be defined as well. Therefore, determination of size/severity of debonding in FRP-retrofitted concrete structures can be considered for future studies.
- In this research, the debonding in experimental specimens was created by using Mylar sheet. For future studies, generation of real debonding conditions in test specimens can be considered.
- In addition to debonding at FRP/concrete interface, delamination inside FRP composite can be considered. In this regard, different combinations of debonding/delamination can be investigated. For instance, various cases of delamination; e.g. different orientations can be studied.
- FRP composites are not only applied on concrete structures and can be used to retrofit different types of structures. For those cases, debonding between FRP and the substrate can be investigated.
- In this research, only CFRP composites have been considered in numerical simulations and experimental measurements. It is suggested that other types of FRPs be considered for investigation.

9 References

- [1] Worden K, Farrar CR, Manson G and Park G. The fundamental axioms of structural health monitoring. *The Royal Society A* 2007; 463: 1639-1664.
- [2] Rosalie C, Chan A, Chiu WK, Galea SC, Rose F and Rajic N. Structural health monitoring of composite structures using stress wave methods. *Composite Structures* 2005; 67: 157-166.
- [3] Heslehurst RB. *Defects and damage in composite materials and structures*. Boca Raton, FL, USA: CRC Press, 2014.
- [4] Sundararaman S. Static damage phenomena and models. In: Boller C, Chang F-K and Fujino Y (eds) *Encyclopedia of structural health monitoring*. John Wiley and Sons, 2009.
- [5] Wenzel H. *Health monitoring of bridges*. Chichester, UK: John Wiley and Sons, 2009.
- [6] Ostachowicz W, Kudela P, Krawczuk M and Zak A. *Guided waves in structures for SHM : the time-domain spectral element method*. Chichester, United Kingdom: John Wiley and Sons, 2012.
- [7] Gianneo A, Carboni M and Giglio M. Feasibility study of a multi-parameter probability of detection formulation for a Lamb waves-based structural health monitoring approach to light alloy aeronautical plates. *Structural Health Monitoring* 2017; 16: 225-249.
- [8] Bijudas CR, Mitra M and Mujumdar PM. Time reversed Lamb wave for damage detection in a stiffened aluminum plate. *Smart Materials and Structures* 2013; 22: 1-8.
- [9] Zhang B, Sun XC, Eaton MJ, Marks R, Clarke A, Featherston CA, Kawashita LF and Hallett SR. An integrated numerical model for investigating guided waves in impact-damaged composite laminates. *Composite Structures* 2017; 176: 945-960.
- [10] Tian Z, Yu L and Leckey C. Delamination detection and quantification on laminated composite structures with Lamb waves and wavenumber analysis. *Journal of Intelligent Material Systems and Structures* 2015; 26: 1723-1738.
- [11] Sherfat MH, Guitel R, Quaegebeur N, Lessard L, Hubert P and Masson P. Guided wave scattering behavior in composite bonded assemblies. *Composite Structures* 2016; 136: 696-705.

- [12] Harb MS and Yuan FG. A rapid, fully non-contact, hybrid system for generating Lamb wave dispersion curves. *Ultrasonics* 2015; 61: 62-70.
- [13] Rose JL. *Ultrasonic guided waves in solid media*. New York, NY, USA: Cambridge University Press, 2014.
- [14] Turco A, Bocciarelli M, Nanni A and Poggi C. Influence of width and thickness of composite laminates on the flexural behavior of reinforced concrete beams and slabs. *Composite Structures* 2017; 178: 186-194.
- [15] Shaw I and Andrawes B. Repair of damaged end regions of PC beams using externally bonded FRP shear reinforcement. *Construction and Building Materials* 2017; 148: 184-194.
- [16] Jiang G, Dawood M, Peters K and Rizkalla S. Global and local fiber optic sensors for health monitoring of civil engineering infrastructure retrofit with FRP materials. *Structural Health Monitoring* 2010; 9: 309-314.
- [17] Nassr AA and Dakhkhni WWE. Damage detection of FRP-strengthened concrete structures using capacitance measurements. *Journal of Composites for Construction* 2009; 13: 486-497.
- [18] Karbhari VM, Chin JW, Hunston D, Benmokrane B, Juska T, Morgan R, Lesko JJ, Sorathia U and Reynaud D. Durability gap analysis for fiber-reinforced polymer composites in civil infrastructure. *Composites for Construction* 2003; 7: 238-247.
- [19] ACI-440R-07. *Report on fiber-reinforced polymer (FRP) reinforcement for concrete structures*. ACI Committee 440, 2007.
- [20] Karbhari VM, Kaiser H, Navada R, Ghosh K and Lee L. *Methods for detecting defects in composite rehabilitated concrete structures*. Report no. SPR 336, 2005. Submitted to Oregon Department of Transportation, and Federal Highway Administration.
- [21] Kim SD, In CW, Cronin KE, Sohn H and Harries K. Reference-free NDT technique for debonding detection in CFRP-strengthened RC structures. *Journal of Structural Engineering* 2007; 133: 1080-1091.

- [22] Giurgiutiu V and Bao J. Embedded-ultrasonics structural radar for in situ structural health monitoring of thin-wall structures. *Structural Health Monitoring* 2004; 3: 121-140.
- [23] Clarke T and Cawley P. Enhancing the defect localization capability of a guided wave SHM system applied to a complex structure. *Structural Health Monitoring* 2010; 10: 247-259.
- [24] Chakraborty A. Modeling of Lamb waves in composite structures. In: Boller C, Chang F-K and Fujino Y (eds) *Encyclopedia of structural health monitoring*. John Wiley and Sons, 2009.
- [25] Memmolo V, Monaco E, Boffa ND, Maio L and Ricci F. Guided wave propagation and scattering for structural health monitoring of stiffened composites. *Composite Structures* 2018; 184: 568-580.
- [26] Lamb H. On waves in an elastic plate. *Proceedings of the Royal Society of London, Series A: Mathematical, Physical and Engineering Sciences* 1917; 93: 114-128.
- [27] Rayleigh L. On waves propagated along the plane surface of an elastic solid. *Proceedings of the London Mathematical Society* 1889; 1: 4-11.
- [28] Su Z and Ye L. *Identification of damage using lamb waves: from fundamentals to applications*. Berlin: Springer, 2009.
- [29] Giurgiutiu V. *Structural health monitoring with piezoelectric wafer active sensors*. Kidlington, United Kingdom: Academic Press, 2014.
- [30] Mitra M and Gopalakrishnan S. Guided wave based structural health monitoring: a review. *Smart Materials and Structures* 2016; 25: 1-27.
- [31] Youbi FE, Grondel S and Assaad J. Signal processing for damage detection using two different array transducers. *Ultrasonics* 2004; 42: 803-806.
- [32] Koh YL, Chiu WK and Rajic N. Effects of local stiffness changes and delamination on Lamb wave transmission using surface-mounted piezoelectric transducers. *Composite Structures* 2002; 57: 437-443.
- [33] Raghavan A and Cesnik CES. Review of guided-wave structural health monitoring. *The Shock and Vibration Digest* 2007; 39: 91-114.

- [34] Rose JL. A baseline and vision of ultrasonic guided wave inspection potential. *Journal of Pressure Vessel Technology* 2002; 124: 273-282.
- [35] Diamanti K, Hodgkinson JM and Soutis C. Detection of low-velocity impact damage in composite plates using Lamb waves. *Structural Health Monitoring* 2004; 3: 33-41.
- [36] Diamanti K, Soutis C and Hodgkinson JM. Piezoelectric transducer arrangement for the inspection of large composite structures. *Composites: Part A* 2007; 38: 1121-1130.
- [37] Drozd M, Moreau L, Castaings M, Lowe MJS and Cawley P. Efficient numerical modelling of absorbing regions for boundaries of guided waves problems. *AIP Conference Proceedings* 2006; 820: 126-133.
- [38] Rajagopal P, Drozd M, A.Skelton E, Lowe MJS and V.Craster R. On the use of absorbing layers to simulate the propagation of elastic waves in unbounded isotropic media using commercially available finite element packages. *NDT&E International* 2012; 51: 30-40.
- [39] Pettit JR, Walker A, Cawley P and Lowe MJS. A stiffness reduction method for efficient absorption of waves at boundaries for use in commercial finite element codes. *Ultrasonics* 2014; 54: 1868-1879.
- [40] Hosseini SMH, Duczek S and Gabbert U. Non-reflecting boundary condition for Lamb wave propagation problems in honeycomb and CFRP plates using dashpot elements. *Composites: Part B* 2013; 54: 1-10.
- [41] Moreau L and Castaings M. The use of an orthogonality relation for reducing the size of finite element models for 3D guided waves scattering problems. *Ultrasonics* 2008; 48: 357-366.
- [42] Cegla FB, Rohde A and Veidt M. Analytical prediction and experimental measurement for mode conversion and scattering of plate waves at non-symmetric circular blind holes in isotropic plates. *Wave Motion* 2008; 45: 162-177.
- [43] Ihn JB and Chang FK. Pitch-catch active sensing methods in structural health monitoring for aircraft structures. *Structural Health Monitoring* 2008; 7: 5-19.

- [44] Ng CT, Veidt M and Rajic N. Integrated piezoceramic transducers for imaging damage in composite laminates. *Proceeding of the 2nd International Conference on Smart Materials and Nanotechnology in Engineering*. China: SPIE, 2009.
- [45] Vanli OA and Jung S. Statistical updating of finite element model with Lamb wave sensing data for damage detection problems. *Mechanical Systems and Signal Processing* 2014; 42: 137-151.
- [46] Ng CT. Bayesian model updating approach for experimental identification of damage in beams using guided waves. *Structural Health Monitoring* 2014; 13: 359-373.
- [47] Zhao J, Ji H and Qiu J. Modeling of Lamb waves in composites using new third-order plate theories. *Smart Materials and Structures* 2014; 23.
- [48] Pant S, Laliberte, Martinez M and Rocha B. Derivation and experimental validation of Lamb wave equations for an n-layered anisotropic composite laminate. *Composite Structures* 2014; 111: 566-579.
- [49] Hayashi T and Kawashima K. Multiple reflections of Lamb waves at a delamination. *Ultrasonics* 2002; 40: 193-197.
- [50] Ramadas C, Balasubramaniam K, Joshi M and Krishnamurthy CV. Interaction of the primary anti-symmetric Lamb mode (A_0) with symmetric delaminations: numerical and experimental studies. *Smart Materials and Structures* 2009; 18: 1-7.
- [51] Ramadas C, Balasubramaniam K, Joshi M and Krishnamurthy CV. Interaction of guided Lamb waves with an asymmetrically located delamination in a laminated composite plate. *Smart Materials and Structures* 2010; 19: 1-11.
- [52] Ng CT and Veidt M. Scattering of the fundamental anti-symmetric Lamb wave at delaminations in composite laminates. *The Journal of the Acoustical Society of America* 2011; 129: 1288–1296.
- [53] Ng CT and Veidt M. Scattering characteristics of Lamb waves from debondings at structural features in composite laminates. *The Journal of the Acoustical Society of America* 2012; 132: 115–123.

- [54] Ng CT, Veidt M, Rose LRF and Wang CH. Analytical and finite element prediction of Lamb wave scattering at delaminations in quasi-isotropic composite laminates. *Journal of Sound and Vibration* 2012; 331: 4870-4883.
- [55] Peng T, Saxena A, Goebel K, Xiang Y and Liu Y. Finite element simulation of Lamb wave propagation in damaged composite laminates and experimental validation. *Adaptive Structures Conference*. National Harbor, Maryland 2014.
- [56] Schubert KJ, Brauner C and Herrmann AS. Non-damage-related influences on Lamb wave-based structural health monitoring of carbon fiber-reinforced plastic structures. *Structural Health Monitoring* 2014; 13: 158-176.
- [57] Choi E, Utui N and Kim HS. Experimental and analytical investigations on debonding of hybrid FRPs for flexural strengthening of RC beams. *Composites: Part B* 2013; 45: 248-256.
- [58] D'Antino T and Pellegrino C. Bond between FRP composites and concrete: Assessment of design procedures and analytical models. *Composites: Part B* 2014; 60: 440-456.
- [59] Perera R, Sevillano E, Arteaga A and Diego AD. Identification of intermediate debonding damage in FRP-plated RC beams based on multi-objective particle swarm optimization without updated baseline model. *Composites: Part B* 2014; 62: 205-217.
- [60] Zhang SS and Teng JG. Finite element analysis of end cover separation in RC beams strengthened in flexure with FRP. *Engineering Structures* 2014; 75: 550-560.
- [61] Haddad RH, Al-Rousan RZ and Al-Sedyiri BK. Repair of shear-deficient and sulfate-damaged reinforced concrete beams using FRP composites. *Engineering Structures* 2013; 56: 228-238.
- [62] Cao VV and Ronagh HR. Reducing the seismic damage of reinforced concrete frames using FRP confinement. *Composite Structures* 2014; 118: 403-415.
- [63] Teng JG, Chen JF, Smith ST and Lam L. *FRP-strengthened RC structures*. Chichester, UK: John Wiley and Sons, 2001.

- [64] Pan J and Wu Y-F. Analytical modeling of bond behavior between FRP plate and concrete. *Composites: Part B* 2014; 61: 17-25.
- [65] Biolzi L, Ghittoni C, Fedele R and Rosati G. Experimental and theoretical issues in FRP-concrete bonding. *Construction and Building Materials* 2013; 41: 182-190.
- [66] Bocciarelli M and Pisani MA. Survey on the interface behaviour in reinforced concrete beams strengthened with externally bonded FRP reinforcement. *Composites: Part B* 2017; 118: 169-176.
- [67] Alampalli S. Effectiveness of FRP materials with alternative concrete removal strategies for reinforced concrete bridge column wrapping. *International Journal of Materials and Product Technology* 2005; 23: 338 - 347.
- [68] Li Z, Leung C and Xi Y. *Structural Renovation in Concrete*. New York, USA: Taylor and Francis, 2009.
- [69] Alampalli S and Ettouney MM. Structural health monitoring. In: Zoghi M (ed) *The international handbook of FRP composites in civil engineering*. Boca Raton, FL, USA: CRC Press, 2014.
- [70] Mahmoud AM, Ammara HH, Mukdadi OM, Ray I, Imani FS, Chen A and Davalos JF. Non-destructive ultrasonic evaluation of CFRP–concrete specimens subjected to accelerated aging condition. *NDT&E International* 2010; 43: 635-641.
- [71] Hollaway LC. A review of the present and future utilisation of FRP composites in the civil infrastructure with reference to their important in-service properties. *Construction and Building Materials* 2010; 24: 2419–2445.
- [72] Nishizaki I and Meiarashi S. Long-term deterioration of GFRP in water and moist environment. *Journal of Composites for Construction* 2002; 6: 21-27.
- [73] GangaRao HVS, Taly N and Vijay PV. *Reinforced Concrete Design with FRP composites*. Boca Raton, FL, USA: CRC Press, 2007.

- [74] Akuthota B, Hughes D, Zoughi R, Myers J and Nanni A. Near-field microwave detection of disbond in carbon fiber reinforced polymer composites used for strengthening cement-based structures and disbond repair verification. *JOURNAL OF MATERIALS IN CIVIL ENGINEERING* 2004; 16: 540-546.
- [75] Brown JR and Hamilton HR. Quantitative infrared thermography inspection for FRP applied to concrete using single pixel analysis. *Construction and Building Materials* 2013; 38: 1292-1302.
- [76] ACI-440.2R-08. *Guide for the design and construction of externally bonded FRP systems for strengthening concrete structures*. ACI Committee 440, 2008.
- [77] Washer GA and Alampalli S. Nondestructive evaluation methods for composite materials: general overview, visual inspection, and microwave methods. In: Zoghi M (ed) *The international handbook of FRP composites in civil engineering*. Boca Raton, FL, USA: CRC Press, 2014.
- [78] Tonnias DE and Zhao JJ. *Bridge engineering: rehabilitation, and maintenance of modern highway bridges*. New York, USA: McGraw-Hill, 2007.
- [79] Ettouney MM and Alampalli S. *Infrastructure health in civil engineering: application and management*. Boca Raton, FL, USA: CRC Press, 2012.
- [80] Taillade F, Quiertant M, Benzarti K and Aubagnac C. Shearography and pulsed stimulated infrared thermography applied to a nondestructive evaluation of FRP strengthening systems bonded on concrete structures. *Construction and Building Materials* 2011; 25: 568-574.
- [81] Feng MQ, Flaviis FD and Kim YJ. Use of microwaves for damage detection in fiber reinforced polymer-wrapped concrete structures. *Journal of Engineering Mechanics* 2002; 128: 172-183.
- [82] Washer GA and Alampalli S. Nondestructive evaluation methods for composite materials: infrared thermography. In: Zoghi M (ed) *The international handbook of FRP composites in civil engineering*. Boca Raton, FL, USA: CRC Press, 2014.
- [83] Fam A and Mirmiran A. QA/QC, maintenance, and repair of hybrid structures. In: Zoghi M (ed) *The international handbook of FRP composites in civil engineering*. Boca Raton, FL, USA: CRC Press, 2014.

- [84] Telang NM, Dumlao C, Mehrabi AB, Ciolko AT and Gutierrez J. *Field inspection of in-service FRP bridge decks- NCHRP report 564*. National Cooperative Highway Research Program 2006.
- [85] Sharma A, Sharma S, Sharma S and Mukherjee A. Ultrasonic guided waves for monitoring corrosion of FRP wrapped concrete structures. *Construction and Building Materials* 2015; 96: 690-702.
- [86] Li J, Lu Y, Guan R and Qu W. Guided waves for debonding identification in CFRP-reinforced concrete beams. *Construction and Building Materials* 2017; 131: 388-399.
- [87] Washer GA and Ziehl P. Nondestructive evaluation methods for composite materials: acoustic methods. In: Zoghi M (ed) *The international handbook of FRP composites in civil engineering*. Boca Raton, FL, USA: CRC Press, 2014.
- [88] Qixian L and Bungey JH. Using compression wave ultrasonic transducers to measure the velocity of surface waves and hence determine dynamic modulus of elasticity for concrete. *Construction and Building Materials* 1996; 10: 237-242.
- [89] Chong KP, Carino NJ and Glenn Washer. Health monitoring of civil infrastructures. *Smart Materials and Structures* 2003; 12: 483-493.
- [90] Hevin G, Abraham O, Pedersen HA and Campillo M. Characterisation of surface cracks with Rayleigh waves: a numerical model. *NDT&E International* 1998; 31: 289-297.
- [91] Edwards RS, Dixon S and Jian X. Depth gauging of defects using low frequency wideband Rayleigh waves. *Ultrasonics* 2006; 44: 93-98.
- [92] Sun M, Staszewski WJ, Swamy RN and Li Z. Application of low-profile piezoceramic transducers for health monitoring of concrete structures. *NDT&E International* 2008; 41: 589-595.
- [93] Aggelis DG and Shiotani T. Repair evaluation of concrete cracks using surface and through-transmission wave measurements. *Cement & Concrete Composites* 2007; 29: 700-711.
- [94] Aggelis DG, Shiotani T and Polyzos D. Characterization of surface crack depth and repair evaluation using Rayleigh waves. *Cement & Concrete Composites* 2009; 31: 77-83.

- [95] Métais V, M.Chekroun, L.LeMarrec, A.LeDuff, G.Plantier and O.Abraham. Influence of multiple scattering in heterogeneous concrete on results of the surface wave inverse problem. *NDT&E International* 2016; 79: 53-62.
- [96] Lee FW, Lim KS and Chai HK. Determination and extraction of Rayleigh-waves for concrete cracks characterization based on matched filtering of center of energy. *Journal of Sound and Vibration* 2016; 363: 303-315.
- [97] Godinho L, Costa DDd, Areias P, Júlio E and Jr DS. Numerical study towards the use of a SH wave ultrasonic-based strategy for crack detection in concrete structures. *Engineering Structures* 2013; 49: 782-791.
- [98] Soleimanpour R and Ng CT. Locating delaminations in laminated composite beams using nonlinear guided waves. *Engineering Structures* 2017; 131: 207-219.
- [99] Rauter N, Lammering R and Kühnrich T. On the detection of fatigue damage in composites by use of second harmonic guided waves. *Composite Structures* 2016; 152: 247-258.
- [100] Shen Y and Cesnik CES. Modeling of nonlinear interactions between guided waves and fatigue cracks using local interaction simulation approach. *Ultrasonics* 2017; 74: 106-123.
- [101] He S and Ng CT. Modelling and analysis of nonlinear guided waves interaction at a breathing crack using time-domain spectral finite element method. *Smart Materials and Structures* 2017; 26: 1-15.
- [102] Yelve NP, Mitra M and Mujumdar PM. Detection of delamination in composite laminates using Lamb wave based nonlinear method. *Composite Structures* 2017; 159: 257-266.
- [103] Soleimanpour R, Ng CT and H.Wang C. Higher harmonic generation of guided waves at delaminations in laminated composite beams. *Structural Health Monitoring* 2016: 1-18.
- [104] Zhang J, Xuan F-Z and Yang F. Effect of surface scratches on the characteristics of nonlinear Rayleigh surface waves in glass. *Journal of Non-Crystalline Solids* 2013; 378: 101-105.

- [105] Kawashima K, Omote R, Ito T, Fujita H and Shima T. Nonlinear acoustic response through minute surface cracks: FEM simulation and experimentation. *Ultrasonics* 2002; 40: 611-615.
- [106] Yuan M, Zhang J, Song SJ and Kim HJ. Numerical simulation of Rayleigh wave interaction with surface closed cracks under external pressure. *Wave Motion* 2015; 57: 143-153.
- [107] Shui G, Kim J-Y, Qu J, Wang Y-S and Jacobs LJ. A new technique for measuring the acoustic nonlinearity of materials using Rayleigh waves. *NDT&E International* 2008; 41: 326-329.
- [108] Guo S, Zhang L, Mirshekarloo MS, Chen S, Chen YF, Wong ZZ, Shen Z, Liu H and Yao K. Method and analysis for determining yielding of titanium alloy with nonlinear Rayleigh surface waves. *Materials Science and Engineering: A* 2016; 669: 41-47.
- [109] Doerr C, Kim J-Y, Singh P, Wall JJ and Jacobs LJ. Evaluation of sensitization in stainless steel 304 and 304L using nonlinear Rayleigh waves. *NDT&E International* 2017; 88: 17-23.
- [110] Chopra AK. *Dynamics of structures: theory and applications to earthquake engineering*. 4th ed. Upper Saddle River, New Jersey, USA: Prentice Hall, 2012.
- [111] Williams M. *Structural dynamics*. Boca Raton, FL, USA: CRC Press, 2016.
- [112] Pavlakovic B and Lowe M. DISPERSE version 2.0.16 User's Manual. Imperial College NDT Laboratory, 2003.
- [113] Lowe MJS. Matrix techniques for modeling ultrasonic waves in multilayered media. *IEEE Transactions on Ultrasonics, Ferroelectrics, and Frequency Control* 1995; 42: 525-542.
- [114] Alleyne DN and Cawley P. The Interaction of Lamb Waves with Defects. *IEEE transactions on ultrasonics, ferroelectrics, and frequency control* 1992; 39: 381-397.
- [115] Ramadas C, Balasubramaniam K, Hood A, Joshi M and Krishnamurthy CV. Modelling of attenuation of Lamb waves using Rayleigh damping: Numerical and experimental studies. *Composite Structures* 2011; 93: 2020-2025. .
- [116] Wu F and Chang F-K. Debond detection using embedded piezoelectric elements for reinforced concrete structures – part II: analysis and algorithm. *Structural Health Monitoring* 2006; 5: 17-28.

- [117] Ng CT. On accuracy of analytical modeling of Lamb wave scattering at delaminations in multilayered isotropic plates. *International Journal of Structural Stability and Dynamics* 2015; 15: 1-12.
- [118] Sohn H, Park G, Wait JR, Limback NP and Farrar CR. Wavelet-based active sensing for delamination detection in composite structures. *Smart Materials and Structures* 2004; 13: 153-160.
- [119] Aryan P, Kotousov A, Ng CT and Cazzolato B. A model-based method for damage detection with guided waves. *Structural Control and Health Monitoring* 2017; 24: 1-14.
- [120] Putkis O, Dalton RP and Croxford AJ. The influence of temperature variations on ultrasonic guided waves in anisotropic CFRP plates. *Ultrasonics* 2015; 60: 109-116.
- [121] Aryan P, Kotousov A, Ng CT and Wildy S. Reconstruction of baseline time-trace under changing environmental and operational conditions. *Smart Materials and Structures* 2016; 25: 1-10.
- [122] Kim G, In C-W, Kim J-Y, Kurtis KE and Jacobs LJ. Air-coupled detection of nonlinear Rayleigh surface waves in concrete-Application to microcracking detection. *NDT&E International* 2014; 67: 64-70.
- [123] Torello D, Thiele S, Matlack KH, Kim J-Y, Qu J and Jacobs LJ. Diffraction, attenuation, and source corrections for nonlinear Rayleigh wave ultrasonic measurements. *Ultrasonics* 2015; 56: 417-426.
- [124] Yang Y, Ng CT, Kotousov A, Sohn H and Lim HJ. Second harmonic generation at fatigue cracks by low-frequency Lamb waves: Experimental and numerical studies. *Mechanical Systems and Signal Processing* 2018; 99: 760-773.
- [125] Lemistre M and Balageas D. Structural health monitoring system based on diffracted Lamb wave analysis by multiresolution processing. *Smart Materials and Structures* 2001; 10: 504-511.
- [126] Kessler SS, Spearing M and Soutis C. Damage detection in composite materials using Lamb wave methods. *Smart Materials and Structures* 2002; 11: 269-278.

- [127] Harri K, Guillaume P and Vanlanduit S. On-line damage detection on a wing panel using transmission of multisine ultrasonic waves. *NDT&E International* 2008; 41: 312-317.
- [128] Diamanti K, Soutis C and Hodgkinson JM. Lamb waves for the non-destructive inspection of monolithic and sandwich composite beams. *Composites: Part A* 2005; 36: 189–195.
- [129] Chamis CC. Mechanics of composite materials: past, present and future. *NASA Technical Memorandum 100793* 1984.
- [130] Ng CT and Veidt M. A Lamb-wave-based technique for damage detection in composite laminates. *Smart Materials and Structures* 2009; 18: 1-12.
- [131] Pratt WK. *Digital image processing*. 2nd ed. New York, NY, USA: John Wiley and Sons, 1991.